

Review

# Molecular Mechanisms of Oxygen Evolution Reactions for Artificial Photosynthesis

Yoshio Nosaka 

Department of Materials Science and Technology, Nagaoka University of Technology, Nagaoka 940-2188, Japan; nosaka@nagaokaut.ac.jp

**Abstract:** Addressing the global environmental problem of water splitting to produce hydrogen fuel by solar energy is receiving so much attention. In water splitting, the essential problem to solve is the development of efficient catalysts for oxygen production. In this paper, having the prospect for a practical application of photocatalysts to artificial photosynthesis, molecular mechanisms in the current literature are briefly reviewed. At first, recent progress in the function of the Mn cluster at the natural photosystem II is briefly described. The kinds of devices in which oxygen evolution reaction (OER) catalysts are used were designated: water electrolyzers, photoelectrodes, and photocatalysts. Some methods for analyzing molecular mechanisms in OER catalysis, emphasized by the FTIR method, are shown briefly. After describing common OER mechanisms, the molecular mechanisms are discussed for  $\text{TiO}_2$  and  $\text{BiVO}_4$  photoelectrodes with our novel data, followed by presenting OER co-catalysts of  $\text{IrO}_2$ ,  $\text{RuO}_2$ ,  $\text{NiO}_2$ , and other metal oxides. Recent reports describing OER catalysts of perovskites, layered double hydroxides (LDH), metal–organic frameworks (MOF), single-atom catalysts, as well as metal complexes are reviewed. Finally, by comparing with natural photosystem, the required factors to improve the activity of the catalysts for artificial photosynthesis will be discussed.

**Keywords:** oxygen evolution reaction; catalysis; mechanism; artificial photosynthesis; titanium oxide; bismuth vanadate; perovskite; metal oxides; fourier transform infrared spectroscopy; density functional theory; metal oxide; solar to hydrogen conversion efficiency



**Citation:** Nosaka, Y. Molecular Mechanisms of Oxygen Evolution Reactions for Artificial Photosynthesis. *Oxygen* **2023**, *3*, 407–451. <https://doi.org/10.3390/oxygen3040027>

Academic Editor: John T. Hancock

Received: 30 August 2023

Revised: 21 October 2023

Accepted: 10 November 2023

Published: 16 November 2023



**Copyright:** © 2023 by the author. Licensee MDPI, Basel, Switzerland. This article is an open access article distributed under the terms and conditions of the Creative Commons Attribution (CC BY) license (<https://creativecommons.org/licenses/by/4.0/>).

## 1. Introduction

The photosynthetic system using solar energy has played a major role in the evolution of plants on the earth, which can oxidize water to generate molecular oxygen. Then, 2.4 billion years ago, the global environment was greatly changed for oxygen to occupy 1/5 of the atmosphere [1]. Before this change, living organisms used hydrogen sulfide as an electron source to live their life. In one billion years, living organisms evolved to utilize water as an electron source resulting in the oxygenic atmosphere. The organisms were further evolved by utilizing oxygen, and it was only about 0.2 million years ago that *Homo sapiens* were born. In recent years, the industrial revolution caused by human beings changed the global environment rapidly by using fossil fuels. Then, to replace fossil fuels with other chemical energy, the production of hydrogen with the aid of solar energy becomes indispensable. In addition, hydrogen will be used to industrially synthesize e-fuels by the reaction with  $\text{CO}_2$ .

In the generation of hydrogen by water splitting, molecular oxygen should be evolved at the same time. However, it is not so easy to artificially achieve photosynthetic oxygen generation by developing novel systems in a short period of time, which took one billion years in the natural world. The oxidation of water to produce oxygen, i.e., oxygen evolution reaction (OER), involves transfers of four electrons and four protons, while the reduction of water to produce hydrogen, i.e., hydrogen evolution reaction (HER), is a reaction of two electrons and two protons. Thus, the OER process is very difficult in comparison with the

HER process. Actually, the overpotential of the present OER electrocatalysts is inevitably higher than that for the HER. In each oxidation step of the OER process, chemical species may appear as intermediates, which are unstable and then named reactive oxygen species (ROS). They are OH radicals, hydrogen peroxide, and superoxide radicals, which were actually detected in the photocatalytic reactions at the semiconductor surface [2]. To sustain the global environment, the reduction of CO<sub>2</sub> by solar light is also an important reaction. However, the CO<sub>2</sub> reduction catalysts are useful only when water is oxidized to generate oxygen at the same time [3]. Since oxygen evolution is the important key reaction, there are a lot of research papers describing the strategy to improve the OER efficiency with various kinds of methods, and the reaction mechanism was analyzed to increase productivity.

In the present paper, molecular mechanisms of water oxidation catalysis are briefly reviewed, with anticipating a practical application to artificial photosynthetic systems with photocatalysts [4]. Thus, this review is primarily focused on heterogeneous surface catalysis. At first, the function of the Mn cluster at the center of the photosystem II and the movement of protons to be released from water is briefly described. It is followed by the classification of catalysts for the OER employed, i.e., electrolyzer, photoelectrodes, and photocatalysts, in which the reaction mechanisms should have some difference. In the next section, the methods to investigate the molecular mechanism of OER processes are briefly described, where Fourier transfer infrared (FTIR) spectroscopy was mainly mentioned because it could detect the molecular structure in the OER process. Next is the widespread common mechanisms of OER, followed by the molecular mechanism of OER for each catalyst, which includes TiO<sub>2</sub>, BiVO<sub>4</sub>, and SrTiO<sub>3</sub> as semiconductors having the ability to direct excitation with photons. Especially for TiO<sub>2</sub> and BiVO<sub>4</sub>, based on some unpublished data, some discussions were added to review the reported data. The following part of this report is devoted to the recent progress in the molecular mechanism of OER for various catalysts; IrO<sub>2</sub>, RuO<sub>2</sub>, transition metal oxides, CoO<sub>x</sub>, NiO<sub>x</sub>, FeO<sub>x</sub>, mixed metal oxides, perovskites, layered dihydroxides (LDHs), metal–organic frameworks (MOFs), metal complexes, single-atom catalysts (SAC), and so on. Finally, the characteristic difference between natural photosystem and present OER catalysts are pointed out, and the required factors to improve the activity of the catalysts for artificial photosynthesis will be discussed.

## 2. Oxygen Evolution Mechanism of Photosystem II (PS II)

In the photosynthesis of plants, across the thylakoid membrane, a series of electron transfers and proton transfers takes place simultaneously. That is, on the one side, two water molecules are oxidized to produce one molecular oxygen and four protons, and, on the other side of the membrane, high energy molecule ATP is produced from ADP in conjunction with the formation of an electron carrier, NADPH [5]. Oxygen is produced in light-driven water plastoquinone oxidoreductase enzymes, which are known as photosystem II (PS II). At the reaction center of PS II, photoexcitation energy is gathered with six pigments at the manganese–calcium–oxide-based Mn<sub>4</sub>CaO<sub>5</sub> cluster in the reaction center, and then four electrons and four protons are transferred [6,7].

The radiation-damage-free structure of PS II was successfully analyzed with femtosecond X-ray free-electron lasers (XFEL). On the absorption of the second photon, the sixth O atom, O<sub>6</sub>, is coordinated at the position of 1.5 Å from the fifth O atom, O<sub>5</sub>, of the Mn<sub>4</sub>CaO<sub>5</sub> cluster, forming an O=O bond [8]. The O<sub>6</sub> comes from H<sub>2</sub>O, which was introduced by flipping the amine of the glutamic acid (Glu) residue [9].

Detailed time causes of electron transfer and proton transfer were analyzed by many spectroscopic methods, such as time-dependent fluorescence and transient absorption. The Mn<sub>4</sub>CaO<sub>5</sub> cluster, at which molecular oxygen is generated, releases an electron to reduce the neighboring phenylalanine residue (Phe) [7]. Flash-induced FTIR difference spectroscopy revealed that the electron further moves to an iron quinone complex due to a small energy difference [10]. EPR measurements forecasted that, at the last quasi-stable state in four-step oxidation, the peroxo group, O–O bond is produced in the cluster, and

immediately it turns into an  $O_2$  molecule forming an O vacancy [11]. Density functional theory (DFT) calculation suggested that this O-O bond has the ionic state of  $[O_2]^{3-}$ , and then antiferromagnetic interaction with the Mn ion stabilizes the O-O group to make a unique low-energy reaction path [12].

The application of time-resolved X-ray emission spectroscopy (XES) to each oxidation step revealed that oxidized tyrosine residue (Tyr) causes the fourth electron transfer, generating  $Mn^{IV}$  in the cluster, and all four Mn ions of the cluster became the valency of IV before the generation of the O-O bond [13]. Structural analysis was further developed [14], and the time-resolved structure after the photon absorption suggested the time cause of the position of the ligands and the water path [15]. The time-resolved IR spectra of microsecond resolution and computational chemistry showed the reaction time of electron transfer and proton transfer of four steps after each photon absorption as shown in Figure 1 [16].

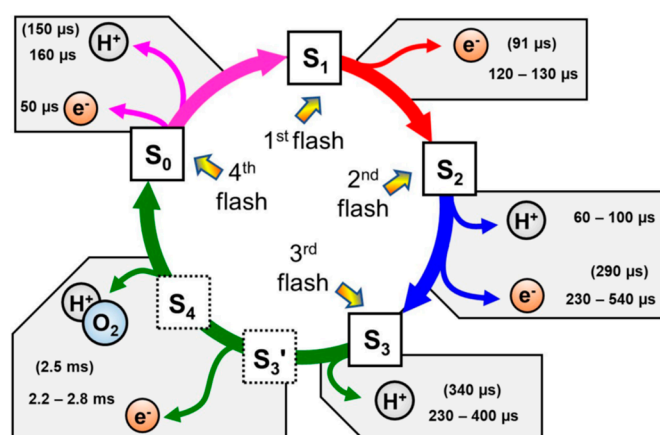


**Figure 1.** S-state cycle in photosystem II (PS II) with time constant values (in parenthesis were newly determined). Reproduced from *Nature* 2023 [16] under the license of CCA4.0.

In the photosynthesis cycle in Figure 1, the reaction process from  $S_{3'}$  to  $S_4$  was clarified recently as shown in Figure 2 [16]. (i) Immediately after the electron release from the  $CaMn_4O_5$  cluster to Tyr, the proton coordinated to Glu moves to asparagine acid (Asp) residue by a tactical proton relay mechanism. (ii) O6 gets close to O5, and (iii) the O-O bond is formed.

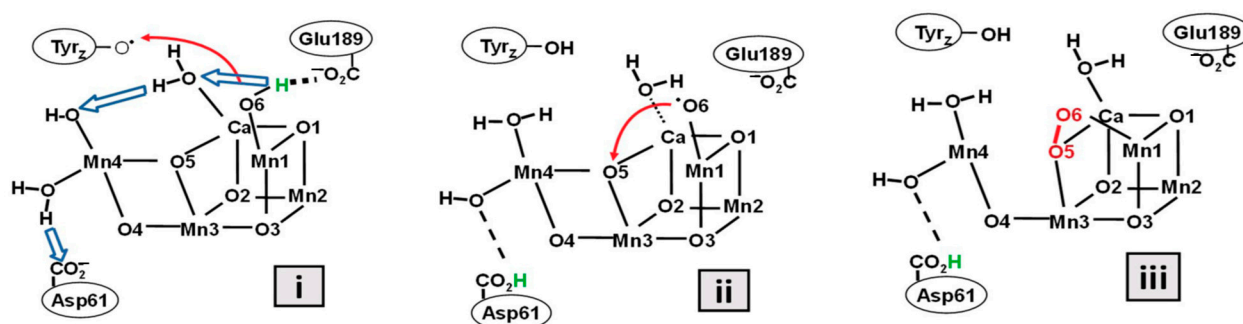


**Figure 2.** Molecular sketches of atomic and electronic rearrangements leading to peroxide formation corresponding to the  $S_{3'}$  to  $S_4$  states in Figure 1. Reproduced from *Nature* 2023 [16] under the license of CCA4.0.

A new prototype of a semiartificial system is reported by anchoring PS II on a polyethyleneimine-coated microporous carbon electrode. Practical applications may have difficulty with the low current density and durability [17]. Thus, the hybrid application may not be easy because PS II has been developed only to work in nature.

### 3. Devices for Oxygen Evolution

It has been reported since the 18th century that the application of electricity to the electrode meets with the dissociation of water to produce hydrogen and oxygen at a ratio of 2:1 [18]. This electrolysis reaction is practically used as a water electrolyzer to produce oxygen in the present day. About 50 years ago, it was found that a TiO<sub>2</sub> semiconductor electrode caused the formation of oxygen and hydrogen by irradiating light [19]. After the report of this photoelectrochemical method, a particulate photocatalytic reaction was tried to photo-split water into hydrogen and oxygen with many semiconducting materials [4]. As the developments in the water splitting methods, this section is divided into three sub-headings: water electrolyzers, photoelectrochemical cells, and particulate photocatalysts.

#### 3.1. Water Electrolyzer

Currently, 95% of total hydrogen is formed by steam reforming of fossil fuels [20]. On the other hand, 5% of hydrogen in the global market is produced by water electrolysis. The electricity capital expenses account for over 60% of H<sub>2</sub> content for renewable electricity if the electrolyzer can keep sustainable operation for 4000 h [21]. If the electricity could be served by solar panels, residual electricity caused by the monthly and daily variations of sunlight could be used to store the hydrogen energy. This system may actually contribute to the global environmental problems. From the viewpoint of the global transportation of energy, green hydrogen, as solar-driven chemical energy, should become indispensable in the near future, and then water electrolysis will become a widespread technology. Since the OER process is significantly difficult compared with the HER process as described above, the industrial scale of OER devices becomes important to produce green hydrogen.

As the water electrolyzer, there is an alkali system in which the anode and cathode are separated by a porous diaphragm [21], an acidic system with a proton exchange membrane (PEM) [22–24], and a solid oxide system with a high-temperature O<sup>2-</sup> conductor [25]. Water electrolysis is the reverse reaction of hydrogen–oxygen fuel cells where chemical energy is changed to electric energy. Therefore, the equipment configuration of the apparatuses with PEM and solid electrolyte resemble the polymer electrolyte fuel cell (PEFC) and solid oxide fuel cell (SOFC), respectively. An alkaline water electrolyzer is conventionally used in industry, but the maximum current density is 400 mAcm<sup>-2</sup>, and a long time is spent to start the operation. Then, the alkaline system is not favorable to use renewable energy with large fluctuation [25]. Since solid electrolytes need high temperatures, most of the research aims to acid water electrolysis [26]. The U.S. Department of Energy announced a goal to reach a lifetime of 80,000 h in 2050 [23].

To prepare a solar water splitting system, electrochemical water splitting systems can be easily integrated with photovoltaic systems. Actually, a solar to hydrogen (STH) conversion efficiency of 30% has been reported by connecting an available three-layer solar cell of InGaP/GaAs/GaInNAsS with an electrolyzer consisting of a Pt black cathode and an Ir black anode [27]. By integrating Pt and Ni on each surface of the GaInP/GaInAs/Ge solar cell, the obtained photoelectrochemical cell showed 18% STH efficiency at 15 suns [28]. By using a commercially available IrRu-coated Ti anode connected to a Pt-coated Si photocathode by a perovskite solar cell, the STH efficiency was reported to be more than 17% [29]. Furthermore, by using a concentrated integrated photoelectrochemical device, a kilowatt-scale solar hydrogen production system is reported to be realized [30]. Though the higher STH efficiencies have been reported, enlargement of the devices and the cost for the practical operation may become problems.

The OER catalysts for water electrolysis have been developed mainly in alkaline and acidic conditions. Since photocatalytic water splitting is expected to take place mainly in a neutral solution, the OER catalysts for the electrolyzer may not be suitable for the photocatalytic system. However, water electrolysis in nearly neutral conditions has also been developed, which contains the OER catalysts used as co-catalysts of photocatalysts [31].

### 3.2. Photoelectrochemical Cell

Photoelectrochemical (PEC) cells based on an interfacial electric field formed at a semiconductor–electrolyte junction aim to achieve solar-driven water electrolysis at low cost and with low complexity [32]. This is the method to produce hydrogen by solar energy without using solar cells, which was discovered 50 years ago [33]. PEC devices have been investigated for many semiconducting materials. The water electrolyzers stated above are operated at a high current of more than  $1 \text{ A cm}^{-2}$ . On the other hand, since the uncondensed solar flux is less than  $10 \text{ m A cm}^{-2}$ , the operation condition of OER catalysts of PEC devices is different from that of electrolyzers. The materials that pose catalytic activity and durability under anodic polarization are limited to  $\text{TiO}_2$ ,  $\text{WO}_3$ ,  $\text{BiVO}_4$ ,  $\alpha\text{-Fe}_2\text{O}_3$ ,  $\beta\text{-NiOOH}$ , and  $\text{CuWO}_4$  [34–37].

A photoelectrochemical reaction with semiconductor electrodes was investigated in connection with the research in the reaction mechanism at the surface of visible-light-responsive photocatalysts;  $\text{GaN}$  [38],  $\text{Ta}_3\text{N}_5$  [39,40],  $\text{LaTiO}_2\text{N}$  [41]. When  $\text{BiVO}_4$  was used as a photoanode, a solar water splitting efficiency of 3.17% was reported [42]. To increase the OER efficiency, the loading of cobalt phosphate (CoPi) catalyst [43], and the application of high valence iron ion,  $\text{Fe}^{4+}$  [44], have been reported. The STH efficiency of the PEC device made of semiconductor photoelectrodes has not exceeded that of the above-mentioned combination device with a water electrolyzer and a photovoltaic cell. For solar-driven electron sources, OER at  $\text{SrTiO}_3$  and  $\text{BiVO}_4$  photoanodes were used not only for the generation of hydrogen but also for the reduction of  $\text{CO}_2$  to generate formic acid [45] and carbon monoxide [46], respectively.

### 3.3. Particulate Photocatalysts

Particulate semiconductor photocatalysts seem to act as a small device of electrolyzer combined solar cell [47]. However, reactions on the electrode surface are essentially different from those on the particulate photocatalyst surface as discussed previously [48]. In the case of an electrochemical reaction, electrons are supplied continuously from the electric source through a lead wire. On the other hand, in the cases of photocatalysts and photoelectrodes, interfacial electron transfer reactions occur only at the absorption of photons. Thus, to proceed four-electron reaction, the reaction step of OER should wait until the absorption of the next photon. Moreover, in an electrochemical reaction, the electron transfer occurs at the electric field gradient formed at the surface of the electrode against the electrolyte in the solution, while in a photocatalytic reaction, the surface-trapped carrier generates the electric field gradient against the surface Fermi level [48]. Since the surface-trapped carrier may recombine with the carrier generated by the next absorption of a photon, the electron transfer reaction in photocatalysis should be rapid to overcome the rapid recombination reaction. Thus, the stability of the reaction intermediate, ROS in the case of OER, is most important to accomplish the process. The concept for effective photocatalysts is contrastive to the case of the PS II described above, where the reaction intermediate was not formed but the photon energy is accumulated in the valency of four Mn ions, and, on the third flash,  $\text{O}_2$  is released immediately after the O-O bond formation.

There is an extensive review of water splitting with semiconductor photocatalysts [49,50]. The application of photocatalysis to the reduction of  $\text{CO}_2$  has been compiled [3]. For practical testing of solar hydrogen generation, porous sheets of  $100 \text{ m}^2$  made of photocatalyst powder were employed where the STH efficiency was 0.76% [51]. To increase the STH efficiency, p-n junction photocatalysts were proposed by combining two semiconductors to avoid recombination [52]. In a recent paper, by using  $\text{Co}_3\text{O}_4$  as an OER co-catalyst on  $\text{InGaN}/\text{GaN}$  nanowire photocatalyst, STH of 9% in pure water, and 7% in seawater have been reported [53]. In a large-scale photocatalytic water-splitting system, an STH efficiency of 6.2% was described [53]. In comparison with the photovoltaic–electrolyzer combination systems, photocatalytic systems have some strong points that contain the scalability to enlarge for industrial manufacturers with abundant materials [49].

#### 4. Methods for Investigating Mechanism

The molecular mechanism of OER at the atomic level is conveniently predicted by means of calculation chemistry. However, it should be supported by appropriate experimental measurements. In the field of photocatalysis, FTIR and electron paramagnetic resonance (EPR) spectroscopies under operation have been used to investigate the reaction mechanism. Operand/in situ measurements have recently been utilized for other spectroscopy such as X-ray absorption spectroscopy (XAS) and X-ray emission spectroscopy (XES), especially for electrocatalysts [54,55]. In this section, such analytical methods for catalyst surface, including operand X-ray diffraction (XRD) measurements, and electrochemical transmission microscopy (EC-TEM) will be described briefly.

##### 4.1. Electrochemical Analysis

Electrochemistry is a conventional technique to investigate the electron transfer reaction at the solid surface. For kinetic analysis, linear sweep voltammetry (LSV), cyclic voltammetry (CV), and electrochemical impedance spectroscopy (EIS) are used. For the analysis of the catalytic activity, the initial rise and slope of the Tafel plot of LSV were used. Initial rise is represented by overpotential at  $10 \text{ mA cm}^{-2}$ , for example. The slope described in the unit of  $\text{mV/dec}$  is useful for microkinetic analysis, which can predict the rate-determining step in the four-step oxidation of OER [56–58]. In the cases of  $\alpha\text{-Fe}_2\text{O}_3$ ,  $\text{BiVO}_4$ , and  $\text{TiO}_2$  electrodes, when the density of holes is small, the OER rate depends on the first order of the holes, indicating that the first step of OER is rate-determining. On the other hand, when the hole density is large, the OER rate depends on the third order, indicating the third oxidation step of rate-determining [59,60], which agrees with the prediction that the second oxidation step is the formation of relatively stable  $\text{H}_2\text{O}_2$ . Furthermore, in CV measurements, the isotope effect on the peak potential by using  $\text{D}_2\text{O}$  [61] could be used to investigate the mechanism of OER. These electrochemical measurements could not be applied to investigate semiconductor particulate photocatalysts, because the current at the particle surface cannot easily be measured.

##### 4.2. Fourier Transform InfraRed (FTIR) Spectroscopy

FTIR (or IR) spectroscopy is a technique to measure the vibrational mode of bonds between atoms and, different from the Raman spectroscopy, is active only for the vibrational motions which can change dipole moment. Since the sensitivity is usually higher than the Raman spectroscopy, FTIR is the technique to obtain the key information for the molecular mechanism of catalysis [62]. Especially for the OER mechanism, FTIR could directly detect the adsorbed intermediate species, which is usually the ROS adsorbed on surface metal ions. To confine the detection area, the attenuated total reflectance (ATR) method could be used. The use of  $\text{D}_2\text{O}$  and  $\text{H}_2^{18}\text{O}$ , which causes the isotope shift of the signal as predicted by the computer simulation, is helpful in assigning the signal. When linearly polarized IR light was used, the direction of the bond against the surface could be detected. Though FTIR spectroscopy is a traditional technique, a novel method with a synchrotron radiation source has been reported [63].

Table 1 lists the reported positions of FTIR signals for the OER intermediates adsorbed on several metal ions.

##### 4.3. Raman Spectroscopy

Raman spectroscopy can be used to detect the vibration mode of the surface species similarly to the FTIR spectroscopy, and different from FTIR, in Raman spectroscopy, the signal of  $\text{H}_2\text{O}$  could not be observed [90]. Therefore, it is useful for applying to operand detection of the intermediates in OER. For example, the change in surface  $\text{CoO}$  to  $\text{CoOOH}$  in the OER reaction at the  $\text{Co}_3\text{O}_4$  surface has been reported [91]. Since the signal intensity is generally weak, surface-enhanced Raman spectroscopy (SERS) with plasmonic metal particles [92,93] and tip-enhanced Raman scattering (TERS) with plasmonic SPM (scanning probe microscope) tips have been utilized [62].

**Table 1.** FTIR peak position of the intermediate species in the OER processes.

Oxidation Step		/cm <sup>-1</sup>	Mode	Sample	[Reference] Year
1	Co(IV)=O	840	νMO	Co <sub>3</sub> O <sub>4</sub>	[64] 2014
	Ni-O·	908		Ni-NC	[65] 2020
	Ni-O·	916		Ni-Vac	[65] 2020
	Ni-O·	1170–1330		NiV-MOF	[66] 2021
	Mn(IV)=O	712–755		Mn complex	[67] 2001
	Mn(V)=O	970–981		Mn complex	[67] 2001
	Mn(VII)=O	1		NiFe-LDH	[68] 2018
	Fe(IV)=O	912		α-Fe <sub>2</sub> O <sub>3</sub>	[69] 2016
	Ti(IV)-O·	898		n-SrTiO <sub>3</sub>	[70] 2016
	Ir-O	795		Atomic Ir	[71] 2015
	Ir(VI)=O	784		CaIrO <sub>2</sub>	[63] 2022
	946				
2	Mn(IV)=O <sub>2</sub>	810	νOO δOOH	Mn complex	[72] 2021
	Li-OOH	1170		Li in DMSO	[73] 2017
	Ti-OOH	837		Ti-SiO <sub>2</sub>	[74] 2002
	Ti-OOH	838		TiO <sub>2</sub>	[75] 2003
	Ti-OOH	1120–1250		TiO <sub>2</sub>	[75] 2003
	Ni-OOH	1060		Ni-Vac	[76] 2022
	Ni(IV)-OOD	1048		NiFe-MOF	[77] 2019
	Ni-OO-	850–1200		NiOOH	[78] 2019
	Cu-OO-	1180		Cu complex	[79] 2021
	Ru-OOH	986		RuO <sub>2</sub>	[80] 2021
	Ga-OOH	978		Ga <sub>2</sub> O <sub>3</sub>	[81] 2021
	Ir (VI)-OO-	870		CaIrO <sub>2</sub>	[63] 2022
	Ir(III)-OOH	830		IrO <sub>2</sub>	[82] 2011
	Ir-OOH	1055		Atomic Ir	[71] 2021
	Ir-OOH	1065		Ir/Co <sub>3</sub> O <sub>4</sub>	[83] 2023
	Au-OOH	1268		Au electrode	[84] 2005
	Co-OO-Co	833		Co <sub>3</sub> O <sub>4</sub>	[85] 2020
	Li-OO-Li	780, 830		Li in DMSO	[73] 2017
	Ti-OO-Ti	812		TiO <sub>2</sub>	[75] 2003
	Fe(VI)(=O) <sub>2</sub>	840, 856		NiFe-LDH	[86] 2018
M-OO-M	1089	Ru/MnO <sub>2</sub>	[80] 2021		
3	Co(III)-OO·(HO)	1013	νOO	Co <sub>3</sub> O <sub>4</sub>	[64] 2014
	Fe-OO·(HO)	1096		α-Fe <sub>2</sub> O <sub>3</sub>	[87] 2018
	Li-OO·	1127–1139		Li in DMSO	[73] 2017
	M-OO	1128		Ru/MnO <sub>2</sub>	[80] 2021
	Pt-OO·	1005–1016		Pt in Alkaline	[88] 2006
	Mn-OO	1080		Mn <sub>3</sub> O <sub>4</sub>	[89] 2019

#### 4.4. Electron Paramagnetic Resonance (EPR) Spectroscopy

EPR spectroscopy is a unique method to directly detect paramagnetic chemical species with unpaired electrons that are caused at the surface of catalysts in both liquid and solid states [94,95]. Since the method is usually used to detect electron spins, it is called electron spin resonance (ESR) sometimes, or it should be called electron magnetic resonance (EMR) [96] by contrasting with nuclear magnetic resonance (NMR). Since metal atoms could have several spin states depending on the valency and coordination states, EPR is a useful technique to detect the situation around the active site. In addition to metal ions, it could also be used for detecting radical species derived from organic compounds and inorganic molecules.

#### 4.5. Electrochemical Transmission Electron Microscope (EC-TEM)

Though the main part of TEM should be in an ultra-high vacuum, when the sample holder is arranged to be very thin and well shielded from the vacuum, operando TEM images could be obtained [97,98]. Furthermore, electron beam refraction patterns could be acquired [98]. Actually, a phase transition under the polarization was reported [98]. When EC-TEM was combined with electron energy loss spectroscopy (EELS) and energy

dispersive spectroscopy (EDS), valence and distribution of positive ions under catalytic reactions could be investigated [99].

#### 4.6. X-ray Photoelectron Spectroscopy (XPS)

XPS is used usually in a vacuum because electrons cannot easily move in the air, therefore it is difficult to measure the surface of the catalyst in a water environment. When the sample surface is separated from vacuum condition with a thin membrane, under normal pressure the XPS could be measured [100].

#### 4.7. X-ray Absorption Spectroscopy (XAS)

XAS can be used to detect the surroundings of the X-ray-emitting metal. In the XAS method, X-ray absorption near-edge structure (XANES) gives the information of valence and electronic configuration, and extended X-ray absorption fine structure (EXAFS) is used to find out the interatomic distance, coordination number, and disorder of the coordination shell [101–103]. For electrocatalysts, operando XAS observation has been reported [102,104,105].

#### 4.8. X-ray Emission Spectroscopy (XES)

XES is a technique that probes the radiative transitions from an occupied upper shell to an unoccupied or partially occupied core orbital. Since the excitation to the upper shell is required to cause the transition from the upper shell, XES provides complementary information of XAS. When the excitation is performed with XFEL or synchrotron radiation, time-resolved spectra can be obtained. Information about electronic structure, crystal field, and metal–ligand covalence could be obtained. When emission wavelength could be detected from soft X-ray to hard X-ray, measurable element spans from ligand elements, such as O, S, and P, to transition metals and actinides [61]. The apparatus used for XES is applicable for the measurements of resonant inelastic X-ray scattering (RIXS) and high energy resolution fluorescence detected XAS (HERFD-XAS) [61].

#### 4.9. Mössbauer Spectroscopy

Mössbauer spectroscopy is a kind of resonance absorption technique in which the gamma ray of radioisotopes is used as the light source. Since the photon energy of gamma rays is very high, the sensitivity is high. The oxidation state, the spin state, and the symmetric property of ligands could be analyzed. However, nuclei that have a gamma ray emitting isotope are limited to Fe, Sn, Ir, and so on [106]. Recently, synchrotron radiation was used as the light source for the Mössbauer spectra of one of the actinide  $^{161}\text{Dy}$  [107]. The time-dependency of the ligand states [107] and the vibrational states of the ligand of  $^{57}\text{Fe}$ , were operando measured in  $\text{CO}_2$  reduction reaction [108].

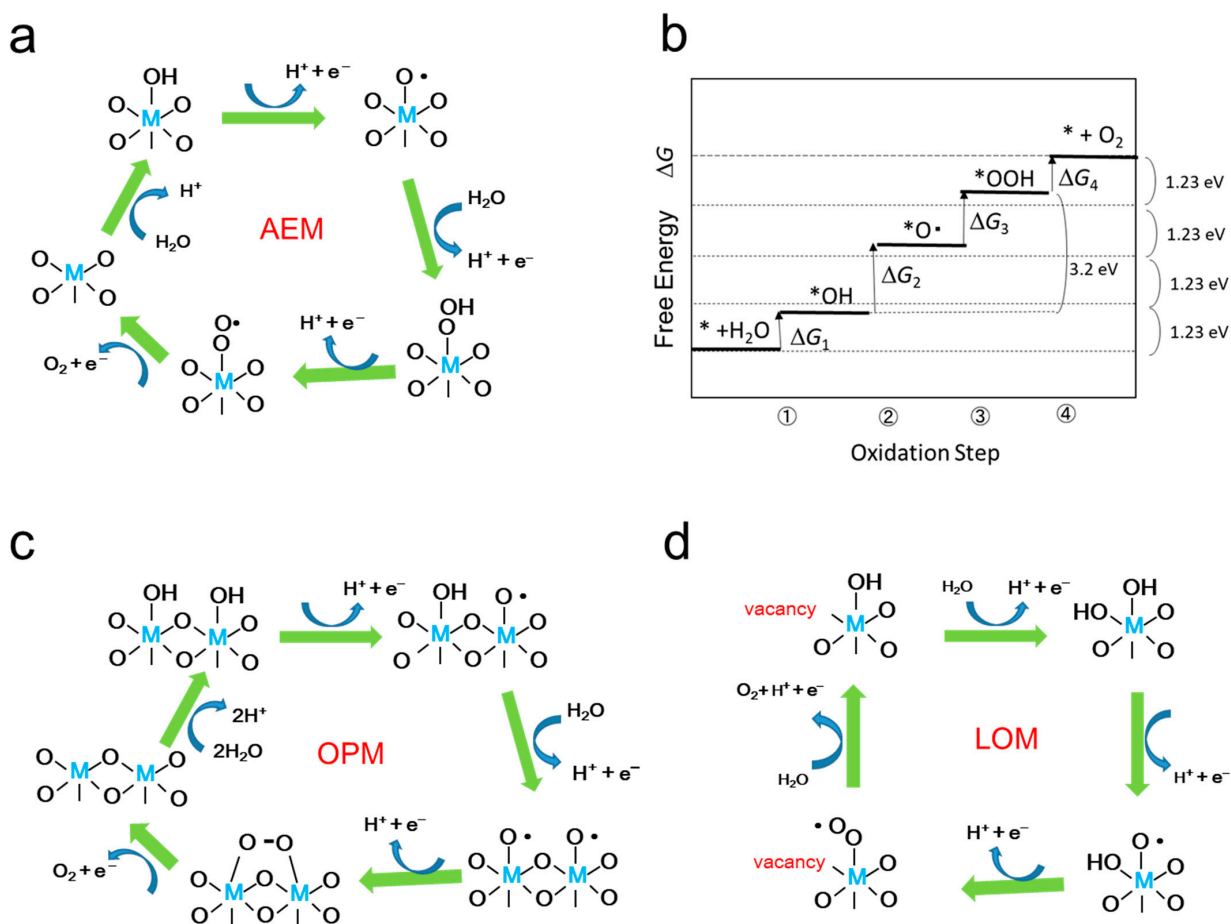
### 5. Common Mechanisms of OER Catalysis

Figure 3a,c,d show the catalytic mechanisms with metal oxides for OER reaction where four protons and four electrons are removed from two  $\text{H}_2\text{O}$  molecules to produce one  $\text{O}_2$  molecule. The mechanisms are classified by whether the lattice oxygen is included (d) or not included (a,c).

In the case that the lattice oxygen is not included, when the reaction proceeds with only one metal ion as shown in Figure 3a, it is called the adsorbate evolution mechanism (AEM). While two adjacent metal ions contribute to the OER as shown in Figure 3c, it is called an oxide pair mechanism (OPM), which may be termed an oxide coupling mechanism (OCM), or interaction of two metal oxide entities (I2M) mechanism. On the other hand, when lattice oxygen participates in the mechanism, it is inclusively called lattice oxygen mechanism (LOM), and Figure 3d is an example of the possible LOM processes [61,109].

As shown in Figure 3b, on the assumption of the AEM process,  $\text{H}_2\text{O}$  is sequentially oxidized to  $^*\text{OH}$ ,  $^*\text{O}$ ,  $^*\text{OOH}$  as the intermediates adsorbed on the surface, where  $^*$  represents the adsorption site on the catalyst. The free energy can be calculated by computational

method, usually DFT calculation is employed. For example, the free energy of each intermediate for OER catalysis of TiO<sub>2</sub>, IrO<sub>2</sub>, and WO<sub>3</sub> is shown in the literature [110]. Figure 3b schematically shows the free energy of each oxidation step in the AEM process. Since the oxidation energy of water is 1.23 eV × 4, the position in the free energy of \*+H<sub>2</sub>O and \*+O<sub>2</sub> is fixed. The overpotential η is calculated from the maximum difference of the free energy ΔG<sub>n,max</sub> = max{ΔG<sub>n</sub> (n = 1, 2, 3, 4)} in the four energy steps as the difference from 1.23 eV, η = ΔG<sub>n,max</sub> - 1.23 eV. As the results of the calculation, it was shown that the free energies of \*OH and \*OOH are linearly correlated, meaning the energy difference between ΔG\*<sub>OH</sub> and ΔG\*<sub>OOH</sub>, that is ΔG<sub>2</sub> + ΔG<sub>3</sub> in Figure 3b, is constant to be 3.2 eV. Therefore, when ΔG\*<sub>O</sub> is located in the middle between ΔG\*<sub>OOH</sub> and ΔG\*<sub>OH</sub> the overpotential η becomes minimum. Therefore, when the expected overpotential η is plotted against ΔG<sub>2</sub> (= ΔG\*<sub>O</sub> - ΔG\*<sub>OH</sub>), η is expected to become a minimum of 0.37 at ΔG<sub>2</sub> = 1.6 eV. This is named scaling relationship, but it is adopted only on the AEM assumption [111].



**Figure 3.** Schematic illustration of simplified OER mechanisms; (a) adsorbate evolution mechanism (AEM), (c) oxide pair mechanism (OPM), and (d) one of the lattice oxygen mechanisms (LOM), (b) schematic free energy change at each oxidation step in AEM OER process. \* represents the adsorption site.

In the reaction model of LOM, one of the O atoms of the oxygen molecule comes from lattice oxygen. Since there are several kinds of lattice oxygens, the reaction mechanism shown in Figure 3d is one of the possible LOM processes. In Figure 4, three other possible LOM processes are shown [112]. In the oxygen vacancy site mechanism (OVSM) shown in Figure 4a, a hole attacks the surface lattice oxygen, followed by a nucleophilic attack with a water molecule (WNA) causing the addition of the OH group at the lattice O atom. In the next hole, attacks cause the release of O<sub>2</sub> and a proton. The next oxidation step causes a surface lattice of OH from OH<sup>-</sup> in water. With the fourth hole, surface OH releases a

proton to return to the original surface O atom. In the single metal site mechanism (SMSM) shown in Figure 4b, when a hole comes into surface lattice oxygen, surface OH becomes surface OO by releasing a proton and making a surface O vacancy, and with the next hole, O<sub>2</sub> is released, and the surface O vacancy was filled by OH. At the next step, surface OH at the metal is recovered, and then at the next step, H of the surface lattice OH is removed to return to the original form. In the double metal site mechanism (DMSM) of Figure 4c, the protons of the adjacent two bridged OH groups are removed by two holes and the M-OO-M bond is formed at the surface. At the next step, O<sub>2</sub> is released, and the vacancy is covered with surface OH on the attack of the fourth hole.

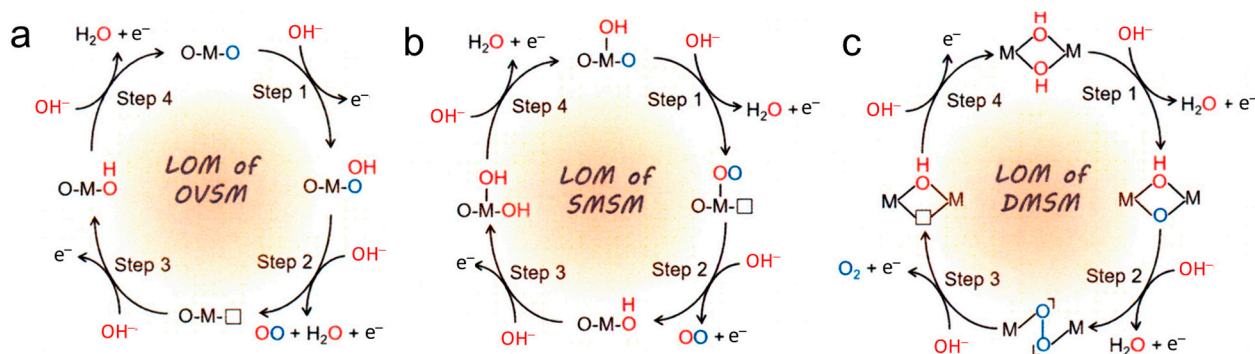


**Figure 4.** Various LOM processes; (a) OVSM = oxygen vacancy site mechanism, (b) SMSM = single metal site mechanism), and (c) DMSM = double metal site mechanism. Reproduced from *Energy Environ. Sci.* **2021** [112] with permission from the Royal Society of Chemistry.

In addition to the four LOM processes described above, other LOM paths can be drawn depending on the kind of metals and the surface crystalline lattice structure. Based on the assumption of the process, the oxidation steps of Gibbs free energy in the OER process can be theoretically calculated. It should be noted that removing the surface lattice oxygen in the LOM process suggests a high probability of the dissolution of metal ions.

## 6. Molecular Mechanism of OER

### 6.1. TiO<sub>2</sub>

The history of TiO<sub>2</sub> for photo-induced water splitting and its molecular mechanism have been described in our previous report [113]. There are abundant reports in which molecular mechanisms of OER at the TiO<sub>2</sub> surface could be found. Research progress in the theoretical calculations for water splitting with TiO<sub>2</sub>-based photocatalysts were also reported [114,115]. Most of the theoretical calculations were performed for rutile (110) and (001) surfaces. Recently, the rutile (100) surface was investigated for OER activity assuming the AEM process [116]. However, it has been shown experimentally that rutile powder consists of (110) and (011) or equivalent surfaces, and reduction occurs at the (110) surface while oxidation occurs at the (011) surface. Though the anatase (101) surface is also used in the theoretical calculation, many experimental observations have indicated that rutile TiO<sub>2</sub> is more active for OER than anatase TiO<sub>2</sub> [2,4]. This experimental conclusion could be explained by the authors as the surface Ti<sub>5C</sub>-Ti<sub>5C</sub> distance of rutile is shorter than that of anatase [117], and the recent theoretical calculation supported this explanation by comparing the anatase (101) surface with the rutile (110) surface [118].

In our previous report, a molecule Ti<sub>5</sub>O<sub>19</sub>H<sub>16</sub> modeling rutile (011) surface was used to investigate the OER process [113]. As the result of the total energy calculation, surface Ti<sub>5C</sub> which can be coordinated by H<sub>2</sub>O could make a hydrogen bonding with the facing bridged O atom. As shown in Figure 5, the first hole attacks the bridge O and then moves to the hydrogen bonding H<sub>2</sub>O molecule to form Ti-O• at the facing Ti<sub>5C</sub> which is the adsorbed OH radical. The second hole can attack Ti-O• or bridged O again to generate OH radical combined with Ti-O•, resulting in the formation of Ti-OOH species. This adsorbed hydroxyperoxo could be stabilized by forming a Ti-OO-Ti structure with another facing

Ti<sub>5</sub>C at the (011) surface. This calculation result suggested that the surface three Ti atoms concerning the OER process are not laid on a line but the third Ti of Ti<sub>5</sub>C should be facing the bridged O [113].

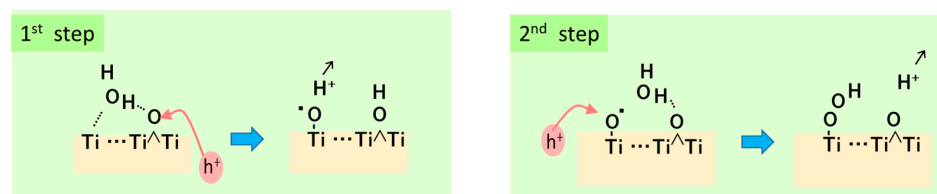


**Figure 5.** Key steps in water oxidation deduced from a DFT calculation for the model molecule of rutile TiO<sub>2</sub>(011) surface. Reproduced from *Catalysts* 2022 [113] under the license of CC BY 4.0 from MDPI publishers.

Two decades ago, Nakamura et al. reported a molecular mechanism of water oxidation at rutile powder as shown in Figure 6 [119,120], and, in our previous review of the ROS formation [2], their reports were referred to in the discussion. In his mechanism, three-coordinated bridging O at a step or kink of the surface is attacked by a hole, simultaneously, WNA takes place to form Ti-O•, and then a pair of Ti-O• generate Ti-OO-Ti structure, and it becomes Ti-OOH [120]. Our prediction described above suggests that the third surface Ti atom may contribute to the following steps. The assignment of FTIR signals was added to this figure. Since the peak at 812 cm<sup>-1</sup> was not clearly shown in their in situ spectra [119], Ti-O• may directly become Ti-OOH by the second hole.

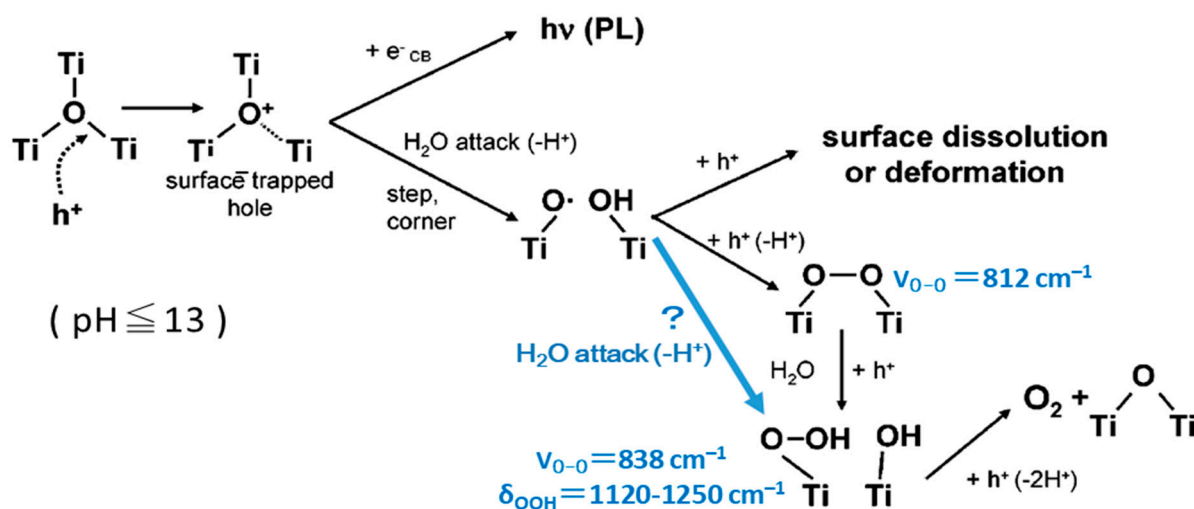


**Figure 6.** Oxygen generation mechanism suggested by Nakamura et al. Blue arrow was added by the present author. Reproduced from *J. Am. Chem. Soc.* 2005 [120] with permission from the American Chemical Society.

The molecular mechanism in Figure 6 was obtained by the observations with the ATR-FTIR for rutile powder and the STM and photoluminescence for rutile single crystals of (100) and (110) facets. The assignment of FTIR spectra was performed for photoinduced O<sub>2</sub> reduction under irradiation based on the isotope effect using D<sub>2</sub>O and H<sub>2</sub><sup>18</sup>O [75]. For the signal of the Ti-OOH group, the isotope effect on the FTIR peaks is shown in Table 2. The calculated signal position and the isotope effect are also listed in Table 2, which was performed for the above-mentioned (011) surface model. The signal assignment seems reasonable, and the isotope effect is well simulated. In the calculation, the signal intensity for bending mode  $\delta(\text{OOH})$  is larger than that of the stretching mode  $\nu(\text{OO})$ , and the signal of the bending mode was clearly shown in the report [75]. However, in the in situ FTIR spectra for water oxidation, the signal at larger than 1100 cm<sup>-1</sup> in the spectrum was not

shown [119]. The spectrum measured in  $\text{H}_2^{18}\text{O}$  did not show the spreading near  $1100\text{ cm}^{-1}$ . Since many chemical species have signals around  $838\text{ cm}^{-1}$ , the observation of Ti-OOH in the experiment may have some problems. In our study, no peaks were observed around  $850\text{ cm}^{-1}$  [117]. They used  $\text{Fe}^{3+}$  ions for electron scavengers in the ATR-FTIR measurements, while we used oxygen as the electron scavenger. Based on the small shift observed for the  $838\text{ cm}^{-1}$  peak, they concluded the involvement of lattice oxygen in the OER process and deduced the molecular mechanism in Figure 6. Since the assignment of the observed peak has ambiguity, the OER process in Figure 6 may have some problems.

**Table 2.** FTIR peak position of hydroxyperoxo coordinated to  $\text{TiO}_2$  and the isotope shifts.

	Mode	Ti-OOH	Ti-O <sup>18</sup> OH	Ti- <sup>18</sup> O <sup>18</sup> OH	Ti-OOD
Experimental <sup>a</sup>	$\delta(\text{OOH})$	1120–1250 $\text{cm}^{-1}$			$\Delta = -220\text{--}320\text{ cm}^{-1}$
	$\nu(\text{OO})$	838 $\text{cm}^{-1}$	$\Delta = -19\text{ cm}^{-1}$	$\Delta = -45\text{ cm}^{-1}$	$\Delta = -67\text{--}97\text{ cm}^{-1}$
DFT calculation <sup>b</sup>	$\delta(\text{OOH})$	1257 $\text{cm}^{-1}$	$\Delta = -2\text{ cm}^{-1}$	$\Delta = -8\text{ cm}^{-1}$	$\Delta = -299\text{ cm}^{-1}$
	$\nu(\text{OO})$	881 $\text{cm}^{-1}$	$\Delta = -23\text{ cm}^{-1}$	$\Delta = -49\text{ cm}^{-1}$	$\Delta = -22\text{ cm}^{-1}$

<sup>a</sup> Experimental data were measured for rutile  $\text{TiO}_2$  powder by Nakamura et al. *J. Am. Chem. Soc.* **2003** [75]. <sup>b</sup> DFT calculation by B3LYP/6-31G(d) method for a rutile (011) surface model molecule  $\text{Ti}_5\text{O}_{19}\text{H}_{16}$  [113].

Having consensus on the assumption that the first oxidation takes place at bridged oxygen Ti-O-Ti, the reaction mechanism of OER was discussed [2]. Recently, Zhuang and Cheng [121] reported that at the rutile (110) surface, pKa of  $\text{Ti}_5\text{C}\text{OH}_2$  is larger than that of  $\text{Ti}_5\text{C}\text{OH}^-$ , and then the coordination structure  $\text{Ti}_5\text{C}\text{O}^{2-}$  exists stably in water and easily becomes Ti-O•. These results in the calculation seem to contradict the fact that the isoelectric point of rutile  $\text{TiO}_2$  is around pH 6. The rutile (110) is not a minor surface in rutile powder as described above. It should be noted that theoretical calculations can bring the result without exception on the basis of the assumed model regardless of the experimental reality. Therefore, it should be careful to refer to the molecular mechanism derived only from the theoretical calculations. Thus, the calculation methods should be used only for the case justified with the experimental results.

## 6.2. $\text{BiVO}_4$

$\text{BiVO}_4$  was discovered first as the semiconductor photocatalyst to have the ability of water oxidation with visible light and the developed process was compiled in the report by Kudo et al. [122]. As the oxygen evolution photocatalysts, Mo-doped  $\text{BiVO}_4$  embedded into an Au layer was employed in a Z-scheme photocatalytic system to exhibit 1.1% STH efficiency [123]. Aiming for utilization in photocatalytic oxidation, there are many reports that describe the effects of surface crystalline systems, morphologies, hetero junctions, and so on [124].

The electrochemical impedance technique was applied to investigate the micro kinetics at  $\text{BiVO}_4$  photoelectrode and found the long-lived holes (0.1–1 s). Two kinds of recombination paths were suggested; one is the fast recombination with photogenerated electrons, and another is the recombination with  $\text{BiVO}_4$  bulk electrons [125]. By measuring the lifetime of the photoluminescence, the recombination was found to occur in nanoseconds, which is probably caused by the multiphonon transition with deep-energy defects [126]. Sub-bandgap is formed by the V-deficiency to accelerate the recombination rate [127].

To understand the reaction mechanism, there are many computational studies in the literature. Walsh et al. concluded that the valence band (VB) of  $\text{O}_{3p}$  is coupled with  $\text{Bi}_{6s}$  to raise the VB maximum, while the conduction band (CB) consists of  $\text{V}_{3d}$  and  $\text{O}_{2p}$  and  $\text{Bi}_{6p}$ . Therefore, the adsorption of ROS is expected to take place at the Bi site [128]. On the other hand, in a later report for the (010) surface, O vacancy provides the V site as an active site. That is, the presence of the O vacancy increased the adsorption energy of  $\text{H}_2\text{O}$ , OH, O•, and the calculated free energy showed a decrease in the barrier for spontaneous charge transfer to electrolyte [129]. The doping of  $\text{Co}^{2+}$  was replaced with  $\text{Bi}^{3+}$ , forming an O vacancy, and  $\text{H}_2\text{O}$  was replaced with the vacancy, which has been calculated to cause a decrease

in the free energy by  $-0.28$  eV [130]. At the (001) surface without vacancy, OH radical is easily formed, on the other hand at the (101) surface, where vacancies are generated by Mo/W doping, strong charge transfer to oxidation intermediates in OER takes place. This difference in the surface character causes charge transfer between (101) and (001) surfaces [131]. For the (010) surface, surface O vacancy is important to the adsorption of water in the catalytic activity [132]. The effect of O vacancy at the subsurface on the charge accumulation in the OER process was investigated. As a result, the O vacancy does not affect the photon acquisition or energy transportation in the crystal [133].

Twin-structured  $\text{BiVO}_4$  was examined in the energy calculation [134]. The structure of the rate-determining step was considered with energy calculations in the OER process for four models (two AEM and two LOM). It was concluded that a larger amount of the twin structure causes a high OER activity [134].

Nikacevic et al. theoretically suggested some routes of OER at the  $\text{BiVO}_4$  surface as shown in Figure 7. At the (001) surface, 97% of vacancies are coordinated with water. As shown in pathway A in this figure, Bi-OO-V is formed as an intermediate, and  $\text{O}_2$  is evolved. On the other hand, only 0.05% of the O vacancy at the (011) surface was coordinated with water, but as shown in pathway B, through the Bi-OOH structure,  $\text{O}_2$  is evolved as OER pathway B with a byproduct of  $\text{H}_2\text{O}_2$  as the HPER pathway [135].

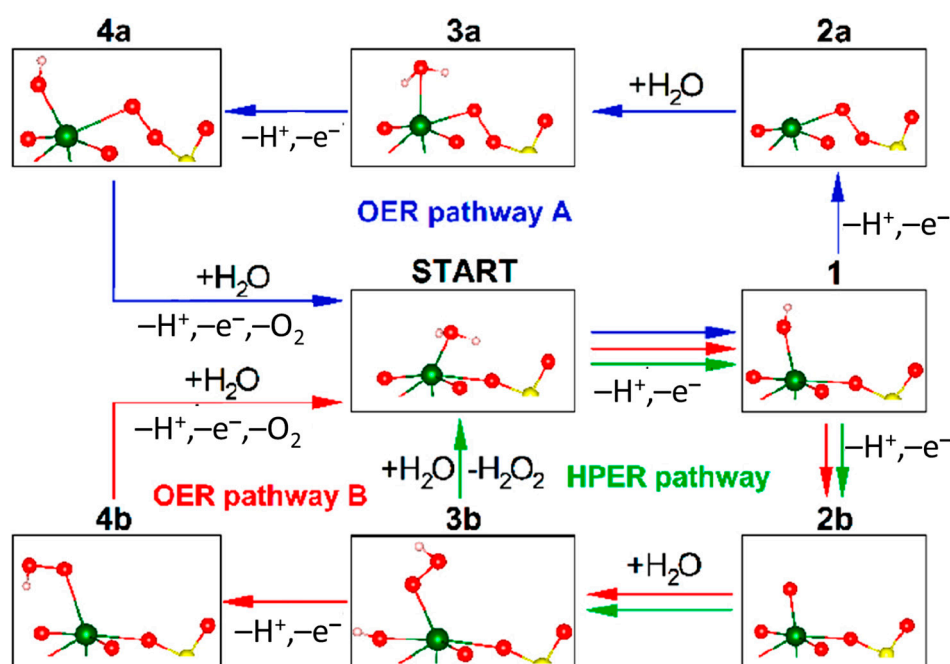


**Figure 7.** Suggested pathways deduced from DFT calculations for oxygen evolution reaction (OER) and hydrogenperoxide evolution reaction (HPER). Reproduced from *ACS Catal.* 2021 [135] with permission from the American Chemical Society.

In the experimental research for the molecular mechanism of the  $\text{BiVO}_4$  OER process, the surface interrogation scanning electrochemical microscopy technique was applied to W/Mo-doped  $\text{BiVO}_4$  electrodes [136]. In this report, the generation of the OH radical was at the ratio of 6% of the absorbed photons in the OER process [136]. However, they detected the OH radical by the oxidation of  $\text{IrCl}_6^{2-}$  for electrochemical monitoring. For non-doped  $\text{BiVO}_4$  electrodes, Nakabayashi et al. detected the OH radical by trapping it with a fluorescent reagent and reported that the yield of the OH radical was 0.06% of the photocurrent while almost 100% was used to generate molecular oxygen [137]. FTIR spectra under light irradiation were measured for the  $\text{BiVO}_4$  photoanode [138]. The in situ FTIR spectra measured in  $\text{H}_2^{18}\text{O}$  and  $\text{D}_2\text{O}$  are compiled in Figure 8. To analyze the isotope shift, DFT calculation with the B3LYP/LanL2DZ method in Gaussian03W was performed

for model molecule  $(\text{OH})_4\text{Bi-OOH}$ , and the isotope shift is shown in Table 3. When the calculated isotope shift was checked with the measured FTIR spectra in the literature [138], the reported assignment of the peak in  $\text{D}_2\text{O}$  was found to be incorrect. The peak positions of  $\delta(\text{OOD})$  and  $\nu(\text{OO})$  should be alternated in  $\text{D}_2\text{O}$ . Then, the large isotope shift in  $\text{H}_2^{18}\text{O}$  shows that both O in Bi-OOH originated from water and that the lattice oxygen of  $\text{BiVO}_4$  was not contained in the OER process. Thus, experimental observations of the presence of Bi-OOH and the 100% yield of the  $\text{O}_2$  show that the OER pathway B in Figure 7 is purely the molecular mechanism of OER at the  $\text{BiVO}_4$  photoanode.

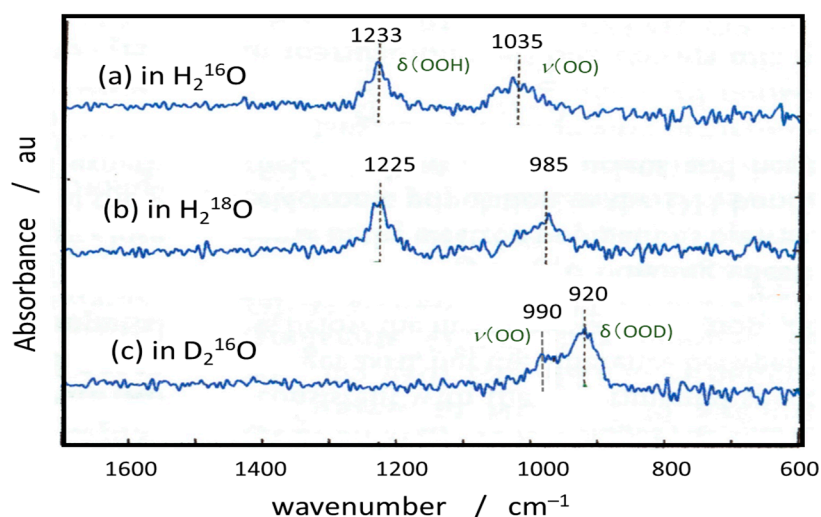


**Figure 8.** ATR-FTIR spectra of  $\text{BiVO}_4$  photoanode under light irradiation in (a) normal water, (b) O-18 labeled water, and (c) heavy water. Compiled from the figures in Ref [138]. Reproduced from *J. Phys. Chem. C* 2021 [138] with permission from the American Chemical Society.

**Table 3.** FTIR peak position of hydroxyperoxo group coordinated to  $\text{BiVO}_4$ .

	Mode	Bi-OOH	Bi-O <sup>18</sup> OH	Bi- <sup>18</sup> O <sup>18</sup> OH	Bi-OOD
BiVO <sub>4</sub> Experiment <sup>a</sup>	$\delta(\text{OOH})$	1233 cm <sup>-1</sup>		$\Delta = -8$ cm <sup>-1</sup>	$\Delta = -313$ cm <sup>-1</sup>
	$\nu(\text{OO})$	1035 cm <sup>-1</sup>		$\Delta = -50$ cm <sup>-1</sup>	$\Delta = -45$ cm <sup>-1</sup>
BiOOH DFT calc. <sup>b</sup>	$\delta(\text{OOH})$	1257 cm <sup>-1</sup>	$\Delta = -2$ cm <sup>-1</sup>	$\Delta = -8$ cm <sup>-1</sup>	$\Delta = -299$ cm <sup>-1</sup>
	$\nu(\text{OO})$	881 cm <sup>-1</sup>	$\Delta = -23$ cm <sup>-1</sup>	$\Delta = -50$ cm <sup>-1</sup>	$\Delta = -22$ cm <sup>-1</sup>

<sup>a</sup> Taken from Ref [138] shown in Figure 8. <sup>b</sup> Calculated for  $(\text{HO})_4\text{BiOOH}$  molecule.

Though OER catalytic activity is observed for photoanode, to increase the separation of charges,  $\text{BiVO}_4$  photoanode is sometimes used with the deposition of some OER catalysts such as Fe-OOH [139], CoPi [140], and  $\text{Co}_3\text{O}_4$  [141].

### 6.3. SrTiO<sub>3</sub>

Strontium titanate ( $\text{SrTiO}_3$ ) is a well-documented photocatalyst in both one-step and two-step (Z-scheme) water-splitting systems as first reported in 1980 [142]. By using an ultrafast sub-band-gap probe with white light and 400 nm beam on  $\text{SrTiO}_3$ , one-electron intermediates were identified to be radicals located in Ti-O• (oxyl) and Ti-O•-Ti (bridge) groups with the initial radical formation time of 1.3 ps as shown in Figure 9 [143]. After photo-triggering the water oxidation reaction from the Nb-doped n- $\text{SrTiO}_3$  surface, the microsecond decay of the intermediates affirms transition-state theory through two distinct time constants. The reaction conditions can be adjusted to allow selection between the two pathways, one characterized by a labile intermediate facing the electrolyte (the oxyl), and the other by a lattice oxygen (the bridge) [144]. Picosecond optical spectra of the Ti-OH population on lightly doped  $\text{SrTiO}_3$  are ordered by the surface hydroxylation. A Langmuir isotherm as a function of pH extracted an effective equilibrium constant relating to the free energy difference of the first oxygen evolution reaction step [145].

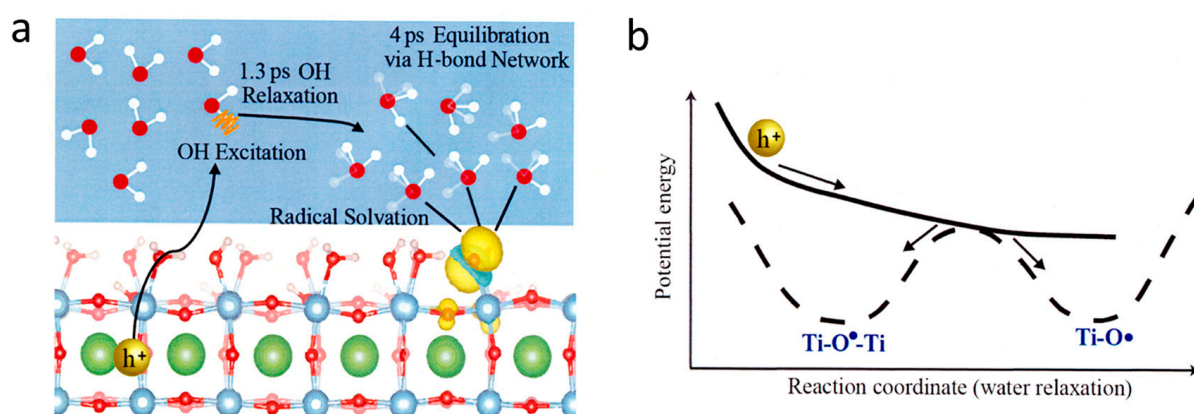


**Figure 9.** Initial step of photocatalytic OER at SrTiO<sub>3</sub>/water interface. (a) OH vibration energy relaxed by H-bond network. (b) Proposed reaction diagram of forming two kinds of surface radicals. Reproduced from *J. Am. Chem. Soc.* **2017** [143] with permission from the American Chemical Society.

Single crystalline SrTiO<sub>3</sub> photoanodes were irradiated with a focused laser to spatially define the degradation. By characterizing the degradation using optical spectroscopy and electron microscopy, the material dissolution constitutes an upper bound of 6% of the charge passed in a pH 13 electrolyte, while for pH 7, it reaches 23%; the pH dependence is anti-correlated with the ultrafast population of trapped charge. Since the dominant lattice dissolution reaction that occurred was thermodynamically concomitant with the OER, the reaction mechanism in Ref [144] was not supported, though the photon flux seems very high in this experiment [146].

#### 6.4. Ga<sub>2</sub>O<sub>3</sub>

On Ga<sub>2</sub>O<sub>3</sub>-based photocatalysts, the overall water-splitting mechanism at a molecular level was suggested, based on the ATR-FTIR investigations combined with the mass spectroscopy (MS) analysis. Different from those observed in other semiconductor photocatalysts, a direct hydroxyl radical formation mechanism was suggested, where two adsorbed OH radicals became adsorbed H<sub>2</sub>O<sub>2</sub> or adsorbed O<sub>2</sub><sup>2-</sup>, which caused the O<sub>2</sub> evolution with two other holes [81].

On different  $\alpha$ -Ga<sub>2</sub>O<sub>3</sub> surfaces, namely (001), (100), (110), and (012), water adsorption and activation were explored by means of DFT calculations. The dissociative water adsorption on all the studied low-index surfaces is thermodynamically favorable, and the most preferentially exposed surface is (012). The computation for the electrochemical model was used to investigate both the HER and the OER on  $\alpha$ -Ga<sub>2</sub>O<sub>3</sub> surfaces. The results indicate that the (100) and (110) surfaces are the most favorable ones for HER and OER, respectively, but they have low stability [147].

#### 6.5. IrO<sub>2</sub> and RuO<sub>2</sub>

Iridium oxide (IrO<sub>x</sub>) was used as the OER co-catalyst of the Y<sub>2</sub>Ti<sub>2</sub>O<sub>5</sub>S<sub>2</sub> photocatalyst for visible light water splitting [148]. Ir-based catalysts are the catalysts of choice to date; nevertheless, their high price and scarcity have greatly hampered the widespread utilization of the PEM water electrolysis technique [149]. On the other hand, ruthenium (Ru), at higher earth abundance and lower price, possesses superior catalytic activity to Ir. However, Ru is prone to dissolution and results in low stability that cannot be applied in practical devices [149]. The surface stability and dissolution of three prominent electro(photo)catalysts for water splitting: RuO<sub>2</sub>, IrO<sub>2</sub>, and TiO<sub>2</sub> in the rutile phase was investigated by using a combination of ab initio steered molecular dynamics, enhanced sampling, and ab initio thermodynamics. A distinct site-specificity in the dissolution of the RuO<sub>2</sub>(110) surface was identified, whereas no such surface site exists for the IrO<sub>2</sub>(110) surface [150]. However, the mechanistic interplay between the OER and material degradation during water electrolysis

is not yet well understood even for the most studied OER electrocatalysts such as IrO<sub>2</sub> and RuO<sub>2</sub> [151].

Anodically grown IrO<sub>x</sub> catalyst films were studied using Raman spectroscopy. In addition to deuteration and <sup>18</sup>O substitution experiments, theoretical models were also constructed using DFT to interpret the experimental data. The material was found to be composed of [IrO<sub>6</sub>]<sub>n</sub> edge-sharing polyhedra (with  $n \geq 3$ ) and characterized over a large potential range (0.0–1.8 V). Ir centers are connected to each other via  $\mu$ -O type oxygen linkages that allow for the Ir centers to electronically couple to each other. Oxidation of Ir<sup>3+</sup> to Ir<sup>4+</sup> at 0.7–1.2 V within a  $\mu$ -O linked polymeric geometry resulted in a blue coloration of the material at high potentials. Theoretical calculations indicated that the optical transition responsible for the color is essentially an Ir-to-Ir charge transfer transition [152].

For a catalyst system of Ir oxide nanocluster, a surface hydroperoxide, Ir-OOH, as an intermediate of OER has been detected by recording the FTIR spectra of the OO vibrational mode at 830 cm<sup>-1</sup>. The detection was achieved upon oxidation of water under pulsed excitation of a visible light sensitizer [Ru(bpy)<sub>3</sub>]<sup>2+</sup> [82]. The OER mechanism of IrO<sub>x</sub> was investigated based on charge accumulation, where the valence change in Ir is more favorable than O–O bond formation. In situ evanescent wave spectroscopy revealed that an intermediate assignable to Ir<sup>5+</sup> with oxygen ligands in opposite spin served as the precursor of OER regardless of pHs (2 to 12), as the generation of this species was not related to valence changes in Ir. The results confirmed that charge accumulation was not rate-limiting for OER on IrO<sub>x</sub>, which is a key mechanistic difference between IrO<sub>x</sub> and less efficient 3d metal electrocatalysts [153]. Time-resolved operando spectroelectrochemistry was employed to investigate the redox-state kinetics of IrO<sub>x</sub> electrocatalyst films for both water and hydrogen peroxide oxidation. Three different redox species involving Ir<sup>3+</sup>, Ir<sup>3x+</sup>, Ir<sup>4+</sup>, and Ir<sup>4y+</sup> were identified spectroscopically. A first-order reaction mechanism was suggested for H<sub>2</sub>O<sub>2</sub> oxidation driven by Ir<sup>4+</sup> states, and a higher-order reaction mechanism involving the cooperative interaction of multiple Ir<sup>4y+</sup> states for water oxidation [154].

On calcined and uncalcined IrO<sub>2</sub>, operando XAS spectroscopy was utilized to study the OER under different protocols. At the elevated OER potentials above 1.5 V, stronger Ir–Ir interactions were observed, which were more dominant in the calcined [155].

With first-principle calculations integrated with implicit solvation at constant potentials, the detailed atomistic reaction mechanism of OER was examined for the IrO<sub>2</sub>(110) surface. The surface phase diagram was determined, and the possible reaction pathways including kinetic barriers, and computed reaction rates were explored based on the microkinetic models [156]. The classical mechanism at the IrO<sub>2</sub>(110) surface was reconsidered. The OER follows a bi-nuclear mechanism with adjacent top surface oxygen atoms as fixed adsorption sites, whereas the Ir atoms underneath play an indirect role and maintain their saturated six-fold oxygen coordination at all stages of the reaction. The oxygen molecule is formed, via an Ir–OOOO–Ir transition state, by association of the outer oxygen atoms of two adjacent Ir–OO surface entities, leaving two intact Ir–O entities at the surface behind [157].

An IrO<sub>2</sub> nanoribbon of monoclinic phase, which is distinct from tetragonal rutile IrO<sub>2</sub>, was provided by a molten alkali mechanochemical method. The intrinsic catalytic activity of IrO<sub>2</sub> nanoribbon was higher than that of rutile IrO<sub>2</sub> due to the low d band center of Ir in this special monoclinic phase structure as confirmed by DFT calculations [158]. Ultrasmall Pd@Ir core–shell nanoparticles (5 nm) with three atomic layers of iron–carbon nanotubes were constructed as an exceptional bifunctional electrocatalyst in acidic water splitting. Due to the core–shell structure, strain generated at heterointerfaces leads to an up-shifted d band center of Ir atoms contributing to a 62-fold better mass activity than commercial IrO<sub>2</sub>. Moreover, electronic hybridization suppresses the electrochemical dissolution of Ir, resulting in the achievement of robust stability [159].

Ir<sub>x</sub>Ru<sub>1-x</sub>O<sub>2</sub> ( $x = 1, 0.6, 0.3,$  and 0) was prepared by the hydrolysis synthesis, and a mechanistic study of the OER was reported. The polarization curves recorded at pHs of 0 to 3 could be well-fitted to a model consisting of a series of concerted electron–proton

transfer reactions (a mononuclear mechanism). It was suggested that the third or fourth step is rate-determining for RuO<sub>2</sub> and IrO<sub>2</sub>, respectively [160].

For single-crystal RuO<sub>2</sub>(110) in acidic electrolytes, the surface structural changes as a function of potential were investigated by in situ surface X-ray scattering measurements with DFT calculations. The redox peaks at 0.7, 1.1, and 1.4 V vs. RHE could be attributed to the surface transitions associated with the successive deprotonation of \*H<sub>2</sub>O on the coordinately unsaturated Ru sites and hydrogen adsorbed to the bridging oxygen sites. At potentials relevant to the OER, an \*OO species on the unsaturated Ru sites was detected, which was stabilized by a neighboring \*OH group on the unsaturated Ru site or bridge site. A new OER pathway, where the deprotonation of the \*OH group is used to stabilize \*OO, was found to be rate-limiting [161]. For the RuO<sub>2</sub>(110) surface, the DFT method considering a possible magnetic effect on the electronic configuration was applied to calculate the thermodynamic stability of possible O versus OH terminations and their effect on the free energies of the OER steps. The magnetic moment of RuO<sub>2</sub> supplies an important contribution to obtaining a low overpotential and to its insensitivity to the exact O versus OH coverage of RuO<sub>2</sub>(110) surface [162].

The OER kinetics on RuO<sub>2</sub> rutile (110), (100), (101), and (111) orientations were experimentally investigated, finding (100) the most active. The potential involvement of lattice oxygen in the OER mechanism was assessed with online electrochemical mass spectrometry. No evidence of oxygen exchange on these oriented facets in acidic or basic electrolytes suggested that lattice oxygen is not exchanged in catalyzing OER on crystalline RuO<sub>2</sub> surfaces [163].

Rh doping for RuO<sub>2</sub> and surface oxygen vacancies to precisely regulate unconventional OER reaction paths via the Ru–O–Rh active sites have been reported. Quasi in situ/operando characterizations demonstrated the recurrence of reversible oxygen species under working potentials for enhanced activity and durability. It was theoretically revealed that Rh–RuO<sub>2</sub> passes through a reaction path of lattice oxygen-mediated mechanism, which is more optimal than the oxygen vacancy site mechanism. The synergistic interaction of defects and Ru–O–Rh active sites causes the \*O formation with the rate-determining step, breaking the barrier limitation (\*OOH) suggested by the traditional AEM process [164].

DFT calculations for RuO<sub>2</sub> demonstrated that the LOM can give rise to higher OER activity than the AEM at the active sites involving structural defects. Although the AEM is preferred for the perfect (110) and (211) surfaces, the formation of metal vacancies due to catalyst dissolution may lead to much lower OER overpotentials for the LOM. By screening several metal impurities in RuO<sub>2</sub>, dopants such as Ni and Co can promote the LOM over the AEM even for perfectly structured surfaces [165]. Transition metal (TM)-doped rutile RuO<sub>2</sub> with different ratios of TM and Ru were discussed through DFT calculation with Hubbard U correction (+U). In low TM doping concentration, the evolved O<sub>2</sub> is generated through the AEM, and the OER activity is limited by the scaling relationship of OER intermediates. In higher TM doping concentrations, the evolved O<sub>2</sub> is generated through the LOM for Cu- or Ni-doped RuO<sub>2</sub>. The distribution of Ru 4d and O 2p orbitals and the adsorption energy of H and O were found to be the major factors that affect the conversion of AEM into LOM [151].

Dispersing RuO<sub>2</sub> over defective TiO<sub>2</sub> enriched with oxygen vacancies (RuO<sub>2</sub>/D-TiO<sub>2</sub>) was reported with an electronic structure modulating strategy. A combination of (spectro-) electrochemistry and theoretical simulations revealed a continuous band structure at the interface between RuO<sub>2</sub> and defective TiO<sub>2</sub>. Thus, a lowered energetic barrier for \*OOH formation was found to be accountable for the largely enhanced acidic OER kinetics [166]. The effect of titanium substitution at different concentrations within nanoscale RuO<sub>2</sub>, Ru<sub>1-x</sub>Ti<sub>x</sub>O<sub>2</sub> (x = 0–50 at%), on the structure, was reported for the OER activity and stability using combined experiments and theory [167]. For the MRuO<sub>x</sub> solid solution (M = Ce<sup>4+</sup>, Sn<sup>4+</sup>, Ru<sup>4+</sup>, and Cr<sup>4+</sup>), the stability was customized by controlling the Ru charge. A scalable single-cell electrolyzer using a SnRuO<sub>x</sub> anode and a polymer electrolyte membrane conveyed the ever-smallest degradation rate during a 1300 h op-

eration at  $1\text{Acm}^{-2}$  [168]. For the sulfate-functionalized RuFeOx catalyst (S-RuFeOx) in a PEM of a water electrolyzer was investigated for OER activity and stability, because RuO<sub>2</sub> shows relatively poor stability. Coupled with the Fe cation doping, S-RuFeOx displayed a remarkable OER performance [169].

### 6.6. Perovskite as Electrocatalysts

Perovskite-type oxide nanocrystals (A<sub>x</sub>B<sub>y</sub>O<sub>z</sub>), which possess distinct thermal stability, ionic conductivity, and electron mobility properties, have attracted increasing interest as efficient OER catalysts [170]. The electronic structure of perovskite-type nanocrystals plays a decisive role in electrocatalytic performance, the orbital filling, metal–oxygen hybridization, and electron correlations of perovskite-type oxide nanocrystals for high-performance OER catalysis were systematically investigated [170]. By using soft X-ray emission and absorption spectroscopies, perovskite OER catalysts were analyzed for the partial density of states on an absolute energy scale. Decreasing the solid-state charge-transfer energy of perovskite can change the mechanisms of the OER from electron-transfer-limited to proton–electron-coupled, and to proton-transfer-limited reactions [171]. The perovskite electrocatalysts with noble metals exhibited the smallest overpotential in various types of catalysts as shown in Figure 10 [172].

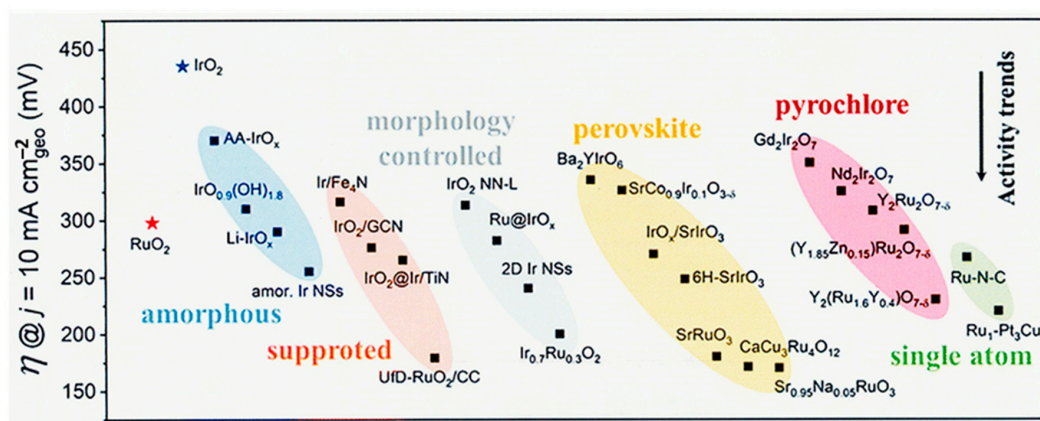


**Figure 10.** Electrocatalytic OER activities (overpotential at  $j = 10\text{mA cm}^{-2}$ ) on noble metal (Ir, Ru, Pt) based catalysts under acidic conditions. Reproduced from *Nanoscale* 2020 [172] with permission from the Royal Society of Chemistry.

On various  $\text{La}_x\text{Sr}_{1-x}\text{CoO}_3^{-\delta}$  as OER catalysts, a general strategy was demonstrated for steering the two mechanisms, AEM and LOM. By delicately controlling the oxygen defect contents, the dominant OER mechanism can be arbitrarily transformed between AEM-LOM-AEM accompanied by a volcano-type activity variation trend. Experimental and computational evidence explicitly revealed that the phenomenon is due to the fact that the increased oxygen defects alter the lattice oxygen activity with a volcano-type trend and preserve the  $\text{Co}^0$  state for preferably the OER [173].

For  $\text{NdNiO}_3$ , the link between structural anisotropy and the OER catalytic activity was established by DFT calculation. The  $\text{NdNiO}_3$  with (100), (110), and (111) orientations display similar oxidative states and metal–oxygen covalence characteristics, but distinct OER activities in experimental results were in the order of (100) > (110) > (111). DFT results confirm that film orientation is a critical determinant of the reaction mechanism. The OER on the (100)-surface favors proceeding via a LOM. In contrast, the reaction on (110)- and (111)-surfaces followed the AEM. The anisotropic oxygen vacancy formation energy and stability are strongly correlated to the reaction mechanism and performance [174]. On  $\text{LaNiO}_3$  epitaxial thin films, electrochemical scanning tunneling microscopy (EC-STM) was used to directly observe structural dynamics during the OER. Based on the comparison of dynamic topographical changes in different compositions, reconstruction of surface

morphology originating from the transition of the Ni species on the surface termination during the OER was proposed [175]. The change in surface topography was induced by  $\text{Ni}(\text{OH})_2/\text{NiOOH}$  redox transformation by quantifying STM images [175].

On  $\text{La}_{1-x}\text{NiO}_3$  perovskite electrocatalysts, direct O–O coupling promoted the OER activity at the interfacial active sites for decorated Ag nanoparticles. The theoretical calculation revealed that oxygen evolution via the dual-site mechanism with direct O–O coupling becomes more favorable than that via the conventional AEM. At  $x = 0.05$ , the electrocatalyst showed 20 times higher mass activity than that of the  $\text{IrO}_2$  electrocatalyst, and the activity increased to 74 times after an accelerated durability test [176].

$\text{Ca}_{2-x}\text{IrO}_4$  nanocrystals exhibited a very high stability of about 62 times that of benchmark  $\text{IrO}_2$ . Lattice resolution images and surface-sensitive spectroscopies demonstrated the Ir-rich surface layer with high relative content of  $\text{Ir}^{5+}$  sites, which is responsible for the high activity and long-term stability. Combining operando IR spectroscopy with the XAS method, key intermediates of  $\text{Ir}^{6+}=\text{O}$  and  $\text{Ir}^{6+}\text{OO}^-$  on Ir-based oxides electrocatalysts were observed, and they were stable even just from 1.3 V vs. RHE. DFT calculations indicated that the catalytic activity of  $\text{Ca}_2\text{IrO}_4$  is enhanced remarkably after leaching the surface Ca ions because  $\text{Ir}=\text{O}$  and  $\text{IrOO}^-$  intermediates can be stabilized on positively charged active sites of the Ir-rich surface layer [63]. Layered perovskite  $\text{Sr}_2\text{IrO}_4$  was chemically exfoliated into protonated colloidal nanosheets with an undamaged perovskite framework. This OER catalyst exhibited about 10 times higher activity than the  $\text{IrO}_2$  catalyst film. As shown in Figure 11, DFT calculation indicated that electrons from the inner Ir atom to the surface were observed in  $\text{IrO}_2$  (e) but not in the case of perovskite nanosheet (d), then the free energy of  $\text{O}^*$  is moderate as shown in (a) compared with the case of  $\text{IrO}_2$  (b). Thus, the structural hydroxyl groups on the surface of protonated nanosheets participate in the catalytic cycle [177].

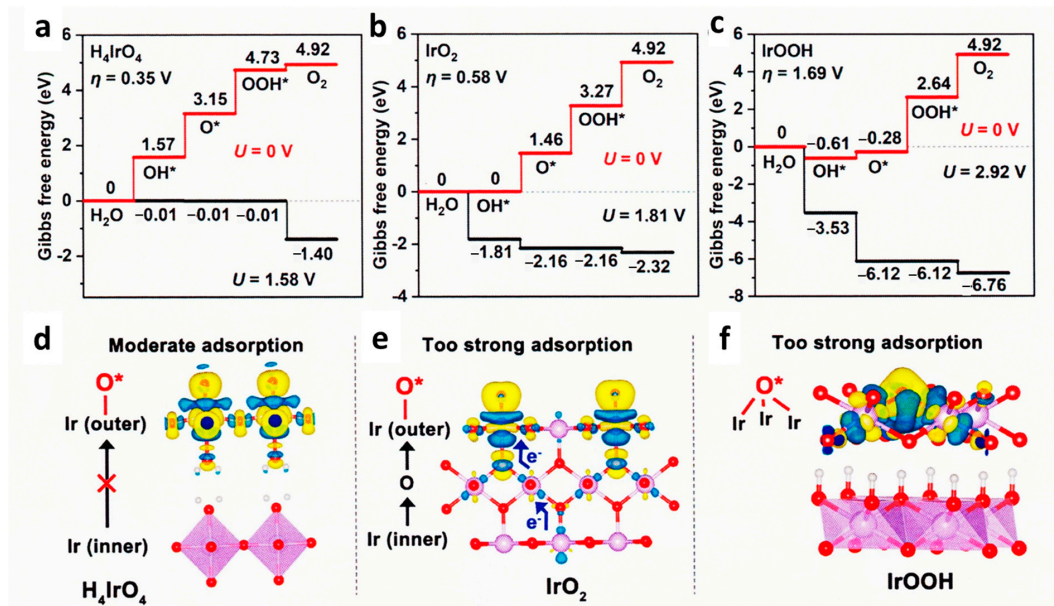


**Figure 11.** DFT calculation of HION,  $\text{IrO}_2$ , and  $\text{IrOOH}$ . (a–c) Gibbs free energy diagrams of  $\text{H}_4\text{IrO}_4$ ,  $\text{IrO}_2$ , and  $\text{IrOOH}$  for OER at Ir sites. (d–f) Charge density difference induced by oxygen adsorption of  $\text{H}_4\text{IrO}_4$ ,  $\text{IrO}_2$ , and  $\text{IrOOH}$  at Ir sites. Reproduced from *ACS Catal.* **2022** [177] with permission from the American Chemical Society.

### 6.7. Transition Metal (TM) Compounds

Multicomponent transition metal oxides and (oxy)hydroxides are the most promising OER catalysts due to their low cost, adjustable structure, high electrocatalytic activity, and outstanding durability. Co-, Ni-, and Fe-based OER catalysts have been considered to be potential candidates to replace noble metals, especially for electrocatalysts, due to their

tunable 3d electron configuration and spin state, versatility in terms of crystal and electronic structures, as well as abundance in nature [23]. The latest advances in the rational design of the related OER electrocatalysts and the modulation of the electronic structure of active sites were comprehensively summarized, besides a brief overview of the mechanisms of OER and the theory and calculation criteria [178].

Wang et al. reviewed the fundamental understanding of the electronic structure of low-cost TM oxide-based catalysts for electrochemical OER, and its relationship with the catalytic activity and the reaction mechanism was discussed [179]. Feng et al. reviewed the relationship between TMs and OER catalyst activity, and then the mechanism of synthesis strategy in different types of TMs-based catalysts was summarized [180]. Guo et al. reviewed the state-of-the-art amorphous transition metal-based OER electrocatalysts, involving oxides, hydroxides, sulfides, phosphides, borides, and their composites, and then the practical application and theoretical modeling of the OER mechanisms in the OER were presented [181]. Though transition metal phosphides often exhibit excellent HER activity, the OER catalytic performance is not outstanding. Huang et al. reviewed the strategies for preparing highly active OER catalysts of transition metal phosphides [182].

The early transition metals (Ti, V, and Cr) can form very stable M=O units, while the late transition metals (Ni and Cu) can only theoretically form unstable M=O structures. On the other hand, for Mn, Fe, and Co, the metal-oxo motif switches between two valence tautomers in the form of  $Mn^{+1} = O^{2-}$  and  $Mn-O\bullet^-$ . The former with an electrophilic oxygen atom can proceed via the acid-base WNA pathway to form the O-O bond, whereas the latter favors the oxygen radical coupling pathway for O-O bond formation [183].

#### 6.7.1. CoOx

CoOOH was selected as the OER co-catalyst of aluminum-doped strontium titanate (SrTiO:Al) photocatalyst to attain almost unity in the internal quantum efficiency of UV-induced water splitting with Rh/Cr HER co-catalyst [184]. The recent progress of Co<sub>3</sub>O<sub>4</sub>-based electrocatalytic materials for the acidic OER was presented with particular reference to the catalytic mechanism and guidelines for the design principles from both experimental and theoretical perspectives [185]. Afterward, emerging strategies were outlined to improve the catalytic performance of Co<sub>3</sub>O<sub>4</sub>-based acidic OER catalysts, including phase engineering, component regulation with doping, composite with carbon-based materials, and multi-phase hybridization [185].

For the application of Co oxides to photocatalysts, operando XPS measurements were performed. The catalyst undergoes chemical-structural transformations as a function of the applied anodic potential, with complete conversion of the Co(OH)<sub>2</sub> and partial conversion of the spinel Co<sub>3</sub>O<sub>4</sub> phases to cobalt oxyhydroxide, CoO(OH), under precatalytic electrochemical conditions. This interpretation revealed that the presence of Co(OH)<sub>2</sub> enhances catalytic activity by promoting transformations to CoO(OH) [186]. To study the mechanism of OER on CoO(OH), operando X-ray absorption and Raman spectroscopy revealed that a Co(IV) species, CoO<sub>2</sub>, is the dominating resting state of the catalyst. Oxygen isotope exchange experiments showed that a cobalt superoxide species is an active intermediate in the OER. This intermediate is formed concurrently with the oxidation of CoO(OH) to CoO<sub>2</sub>. Combining spectroscopic and electrokinetic data, the rate-determining step of the OER was identified as the release of dioxygen from the superoxide intermediate [92].

By using a water-in-salt electrolyte, the water activity was systematically tuned and the mechanism as a function of applied potentials in water electrolysis was probed. The mechanism is sensitive to the applied potential. The Co-OO-Co bond forms via an intramolecular oxygen coupling mechanism at low potentials, whereas it proceeds through a WNA mechanism by forming Co-OOH at high potentials [187].

The morphology-dependent analysis for well-defined crystalline CoO(OH) revealed that the active sites are exclusively located at lateral facets rather than basal facets. Theoretical calculations show that the coordinately unsaturated Co sites of lateral facets upshift the O 2p-band center closer to the Fermi level, thereby enhancing the covalency of Co-O bonds

to yield the reactivity [188]. The sequential oxidation kinetics with  $\text{Co}_3\text{O}_4$  nanoparticles involving multi-active sites for water oxidation in the OER catalytic cycle were resolved by applying quasi-operando transient absorption spectroscopy to a typical photosensitization with Ru-dye and sacrificial electron donor. The  $\text{Co}^{\text{IV}}$  intermediate distribution plays a determining role in OER activity and results in the slow overall OER kinetics [189]. The redox process between  $\text{Co}^{\text{III}}$  and  $\text{Co}^{\text{IV}}$  species does not follow a proton-coupled electron transfer mechanism that is thought to be common prior to the OER, but it involves a proton-decoupled electron transfer, clarified by isotope labeling experiments and in situ electrostatic modulation [190].

An oxygen vacancy (Vo)-rich environment facilitates the reconstruction of  $\text{Co}_3\text{O}_4$  to the  $\text{Co}(\text{OH})_2$  intermediate with proton vacancies ( $\text{Co}^{\text{II}}\text{O}_x(\text{OH})_y$ ), which is favorable for the formation of the active species of  $\text{CoO}(\text{OH})$ . Correlative operando Raman spectra characterizations and electrokinetic analyses indicated that a moderate Vo density can switch the O–O bond formation pathway, from a WNA to an INA pathway, which is more kinetically favorable for water oxidation [191]. As shown in Figure 12b with O vacancy, at step 3, three protons and one electron are removed to form  $\text{Co-O}(\text{OH})$ . At step 4,  $\text{Co}^{\text{III}}$  sites of  $\text{Co-O}(\text{OH})$  are oxidized to  $\text{Co}^{\text{IV}}$  which can be deprotonated (step 8) by hole attack oxo ligand  $\text{Co}^{\text{IV}}=\text{O}$  forms a  $\text{Co-O-O}$  triangle (step 9), and then becomes  $\text{Co}^{\text{II}}\text{-OO}\bullet$  (step 10). At the next oxidation (step 10),  $\text{O}_2$  is released and  $\text{Co}^{\text{II}}$  back to  $\text{Co}^{\text{III}}$  with the coordination of water. The I2M process was excluded based on the experimental results of using the  $\text{H}_2^{18}\text{O}$  isotope [191].

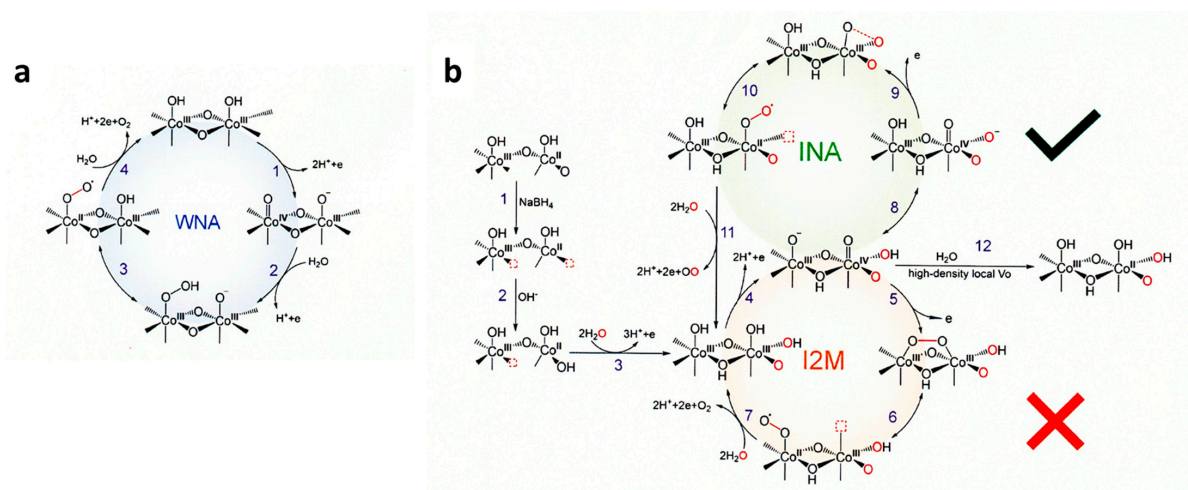


**Figure 12.** Proposed reaction mechanisms of the OER for (a)  $\text{Co}_3\text{O}_4$  and (b)  $\text{Vo-Co}_3\text{O}_4$ . Oxygen vacancy (Vo) prepared by  $\text{NaBH}_4$  reduction was represented by the red dotted boxes. WNA = water nucleophilic attack, INA = intramolecular nucleophilic attack, and I2M = interaction between the two metal-O units. Reproduced from *ACS Catal.* 2023 [191] with permission from the American Chemical Society.

Amorphous  $\text{CoO}(\text{OH})$  layer architecture was loaded onto the surface of  $\text{TiO}_2$ . Tafel analysis, EIS, and CV methods showed that the carrier transfer barrier within the electrode and the transition of  $\text{Co}^{\text{III}}\text{O}(\text{OH})$  to  $\text{Co}^{\text{IV}}\text{O}(\text{OH})$  have the dominating effects on the photoelectrochemical performance. Theoretical calculation revealed that the interface between the  $\text{CoO}(\text{OH})$  and  $\text{TiO}_2$  improves the electronic transfer ability among Co sites [192]. Amorphous  $\text{CoO}(\text{OH})$  layers are electrochemically synthesized on the surface of various cobalt sulfides  $\text{CoS}_x$  and found to decrease the intermolecular energy gap. The decrease in the energy gap accelerates the formation of OER-active high-valent  $\text{Co}^{\text{IV}}$  species [193].

$\text{Co}_3\text{O}_4$  nanocrystals anchored on carbon nitride nanofiber (CNF) were prepared and found that the OER activity under visible light increased by 124 times, where heterogeneous kinetics is improved based on a synergistic effect between its binary components for charge separation and the (222) facet exposure of  $\text{Co}_3\text{O}_4$  nanocrystals. DFT calculations revealed that Vo at (222) facet leads to a reduction of the bandgap of the nanocrystals [194].

The water oxidation with Co cubane cluster,  $\text{Co}_4\text{O}_4(\text{OAc})_4(\text{py})_4$ , as the catalysis was examined by time-resolved rapid scan ATR FTIR spectroscopy, the  $\mu$ -peroxido structure, Co-OO-Co, was established as the intermediate. Where the one-electron oxidized cubane was the sole source of charge that was driven either in alkaline solution by a visible light sensitizer or in hydroxide ( $\text{OH}^-$ ) containing acetonitrile solution [85].

The simulations on the OER mechanism were performed and, in addition, the influence of Fe substitution was examined.  $\text{Co}^{\text{IV}}$  in the pristine  $\text{CoO}(\text{OH})$  promotes the efficient formation of an active O radical intermediate followed by intramolecular O–O coupling. In the case of Fe substitution, the early oxidation of  $\text{Fe}^{\text{III}}$  to  $\text{Fe}^{\text{IV}}$  promotes the electrophilic character in the reaction center, reducing the proton affinity of the surface-bound hydroxyl moieties [195].

### 6.7.2. NiOx

For the nascent ultra-small nickel oxyhydroxide ( $\text{NiOOH}$ ) particles (<3 nm), the thermodynamics of Ni dissolution was calculated by using first-principles theory at a near-neutral pH range, and the mechanism of OER on the  $\gamma$ - $\text{NiOOH}$  surface was clarified. It was concluded that (i) ~4% Ni cations on the surface of  $\gamma$ - $\text{NiOOH}$  dissolve at pH = 7 and 1.73 V vs. RHE; (ii) on the pristine  $\gamma$ - $\text{NiOOH}$  surface, OER proceeds via the “lattice peroxide” mechanism ( $*\text{H}_2\text{O} \rightarrow *\text{OH} \rightarrow *\text{O}-\text{O}_{\text{latt}}\text{H}^* \rightarrow \text{O}-\text{O}_{\text{latt}} \rightarrow \text{O}_2$ ) with an overpotential of 0.70 V; (iii) in the presence of Ni cationic vacancies, OER proceeds via the “hydroperoxide” mechanism ( $*\text{OH} + *\text{H}_2\text{O} \rightarrow *2\text{OH} \rightarrow *\text{OOH} \rightarrow \text{O}_2$ ) with an overpotential of 0.40 V [196].

For  $\text{NiOOH}$ -based materials, light-triggered reversible geometric conversion between octahedron ( $\text{NiO}_6$ ) and square planar ( $\text{NiO}_4$ ) was proposed. The unit cell was undergone to achieve electronic states with alternative metal and oxygen characters throughout the oxygen evolution process. Utilizing this electron transfer pathway can bypass the potential limiting steps, that is, O–O bonding in the AEM and deprotonation in the LOM. As a result, the electrocatalysts that operate through this route showed superior activity compared with previously reported electrocatalysts [197,198].

By incorporating Fe and V into  $\text{Ni}(\text{OH})_2$  lattices, OER activity was improved. X-ray photoelectron/absorption spectroscopies revealed the synergistic interaction between Fe/V dopants and Ni in the host matrix, which subtly modulates local coordination environments and electronic structures of the Fe/V/Ni cations. Further, in situ XAS analyses manifested contraction of metal–oxygen bond lengths in the activated catalyst, with a short V–O bond distance. DFT calculations indicated that the V site of the Fe/V co-doped  $\text{NiOOH}$  gave near-optimal binding energies of OER intermediates and had lower overpotential compared with Ni and Fe sites [199]. A series of Mn-, Co-, Fe-, and Zn-doped nickel oxides were investigated by using operando UV–vis spectroscopy coupled with time-resolved stepped potential spectroelectrochemistry. The  $\text{Ni}^{2+}/\text{Ni}^{3+}$  redox peak potential was found to shift anodically from Mn- < Co- < Fe- < Zn-doped samples, suggesting a decrease in oxygen binding energetics from Mn- to Zn-doped samples. The OER kinetics had a second-order dependence on the density of these oxidized species, suggesting a chemical rate-determining step involving the coupling of two oxo species. The intrinsic turnover frequency per oxidized species exhibits a volcano trend with the binding energy of oxygen on the Ni site, having a maximum activity for the Fe-doped sample as shown in Figure 13. For Ni centers that bind oxygen too strongly (Mn- and Co-doped oxides), OER kinetics is limited by O–O coupling and oxygen desorption, while for Ni centers that bind oxygen too weakly (Zn-doped oxides), OER kinetics is limited by the formation of oxo groups [200].

Oxygen vacancy-enriched porous  $\text{NiO}/\text{In}_2\text{O}_3$  nanofibers ( $\text{Vo-NiO}/\text{In}_2\text{O}_3@\text{NFs}$ ) were fabricated for efficient OER electrocatalysis. Abundant Vo modulated the electronic configuration of the catalyst for altering the adsorption of intermediates to reduce the OER overpotential and promote  $*\text{O}$  formation, upshifting the d band center of metal centers near the Fermi level, and also increasing the electrical conductivity and enhancing the OER reaction kinetics simultaneously. In situ Raman spectra suggested that the Vo can render the  $\text{NiO}/\text{In}_2\text{O}_3$  more easily reconstructible on the surface during the OER course [201].

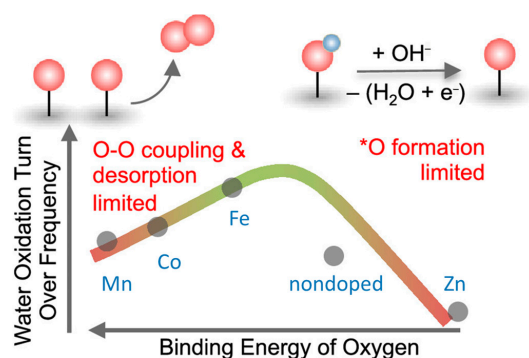


**Figure 13.** Decrease in the binding energy from Zn- to Mn-doped nickel oxides showed a volcano-type OER activity by changing the rate-determining step from  $\bullet\text{O}$  formation to O-O coupling. Reproduced from *J. Am. Chem. Soc.* 2022 [200] with permission from the American Chemical Society.

DFT +U calculations revealed that Ir-doping of a  $\beta$ -NiOOH(001) surface enhanced the electric conductivity while also activating an oxygen site involving three Ni atoms to realize a remarkably low OER overpotential of only  $\eta = 0.46$  V, much lower than the oxygen site involving three Ni atoms in pristine  $\beta$ -NiOOH ( $\eta = 0.66$  V) [202]. Since theoretical calculations predicted that Co, Rh, and Ir dopants would lead to low overpotentials to improve the OER activity of Ni-based hydroxides, an experimental confirmation on the altered OER activities for a series of metals (Mo, W, Fe, Ru, Co, Rh, Ir) doped into  $\gamma$ -NiOOH has been reported [203]. The in situ electrical conductivity for metal-doped  $\gamma$ -NiOOH correlated well with the trend in enhanced OER activities. The DFT calculations, which suggested that the intrinsic connections to the double exchange interaction between adjacent metal ions with various d orbital occupancies, rationalized the experimental results, serving as an indicator for the key metal-oxo radical character [203].

### 6.7.3. FeOx

Recent advancement and progress in initializing Fe-based OER electrocatalysts with different supporting materials, including carbon-based materials, layered double hydroxides, Prussian blue analogous, metal-organic frameworks, were reviewed by Xiong et al. [204]. In the review, the OER mechanism and some typical OER electrochemical parameters of Fe-based electrocatalysts supported on various supporting materials from experimental and theoretical viewpoints were highlighted. Some challenges and expectations for promoting the catalytic performance were described [204].

In photoelectrochemical (PEC) water oxidation on hematite ( $\alpha$ -Fe<sub>2</sub>O<sub>3</sub>), the mechanism of the subsequent rate-limiting O-O bond formation step was investigated by rate law analysis based on EIS measurements and probing the reaction intermediates with operando FTIR spectroscopy. Distinct reaction orders of  $\sim 1$  and  $\sim 2$  were observed in near-neutral and highly alkaline environments, respectively. The unity rate law in near-neutral pH regions suggests a mechanism of WNA to  $-\text{Fe}=\text{O}$  to form the O-O bond. Operando observation of a surface superoxide species by FTIR further confirmed this pathway. In highly alkaline regions, coupling of adjacent surface trapped holes (I2M) becomes the dominant mechanism. While both are operable at intermediate pHs, the mechanism switch from I2M to WNA induced by local pH decrease was observed at a high photocurrent level as shown in Figure 14 [87]. In the recent report, transient photocurrent measurements for hematite photoanodes revealed that the OER rate has a third-order dependence on the surface hole density. A mechanism wherein the reaction proceeds by accumulating oxidizing equivalents through a sequence of one-electron oxidations of surface hydroxy groups was proposed. The key O-O bond formation step occurs by the dissociative chemisorption of a hydroxide ion involving three oxyl sites [205].

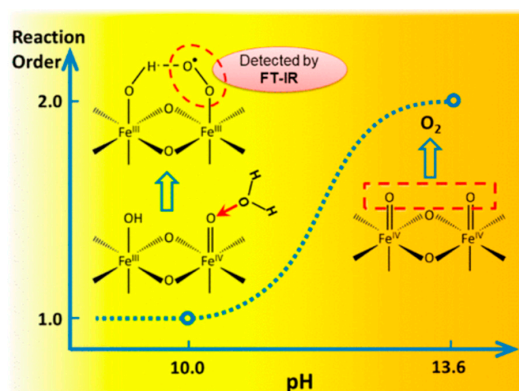


**Figure 14.** In photoelectrochemical water oxidation on  $\alpha\text{-Fe}_2\text{O}_3$ , the OER mechanism switches from WNA to I2M at a strong alkaline solution. Reproduced from *J. Am. Chem. Soc.* **2018** [87] with permission from the American Chemical Society.

Polycrystalline  $\gamma\text{-FeO(OH)}$ , synthesized at room temperature, was used as a stable, although reactive, anode for OER, and electrokinetic studies were performed to unravel the OER pathway [206]. The cell temperature, hydroxyl ion concentration, and the cation of the supporting electrolyte were varied, and the influence of external bias on the OER activity was recorded. Tafel slope and charge-transfer resistance values at high temperatures up to  $65\text{ }^\circ\text{C}$  unambiguously highlight the influence of the thermodynamic barrier and electron transfer kinetics. The faster OER kinetics on polycrystalline  $\gamma\text{-FeO(OH)}$  can also be attributed to an appreciably low activation energy, where the variation of the electrolyte concentration indicated a first-order dependence on the  $\text{OH}^-$  concentration. The deuterium isotope effect implicated the dissociation of hydroxyl ions on the polycrystalline  $\gamma\text{-FeO(OH)}$  as the rate-determining step. The direct effect of cations such as Li, Na, and K of the electrolyte on OER indicated a weak interaction of the cations with the surface-active  $[\text{Fe}^{\text{III}}\text{-OH}]$  species [206].

$\text{Fe}_3\text{O}_4$  with oxygen vacancies ( $\text{Fe}_3\text{O}_4\text{-V}_\text{O}$ ) was synthesized via the Ar ion irradiation method and its OER activity was greatly improved by properly modulating the electron density around Fe atoms, which were evaluated with XANES and EXAFS methods. DFT results indicated the enhancement in desorption of the  $^*\text{OOH}$  groups, which significantly reduced the OER reaction barrier. Actually, the  $\text{Fe}_3\text{O}_4\text{-V}_\text{O}$  catalyst showed a better overpotential than commercial  $\text{RuO}_2$  [207].

Ni-, Co-, and Yb-doped  $\text{FeO(OH)}$  nanorod arrays grown directly on carbon cloth (CC) are synthesized by a simple one-step hydrothermal method. The doped  $\text{Ni}^{2+}$  and  $\text{Co}^{2+}$  can occupy  $\text{Fe}^{2+}$  and  $\text{Fe}^{3+}$  sites in  $\text{FeO(OH)}$ , increasing the concentration of oxygen vacancies and the doped  $\text{Yb}^{3+}$  with a larger ionic radius can occupy the interstitial sites, which leads to more edge dislocations. The oxygen vacancies and edge dislocations greatly enrich the active sites in  $\text{FeO(OH)/CC}$ . In addition, DFT calculations confirmed that doping  $\text{Ni}^{2+}$ ,  $\text{Co}^{2+}$ , and  $\text{Yb}^{3+}$  modulates the electronic structure of the main active Fe sites, bringing its d-band center closer to the Fermi level and reducing the Gibbs free energy change in the rate-determining step of the OER [208].

#### 6.7.4. MnOx

Nature uses a Mn cluster for water oxidation in PS II, and thus, water oxidation using Mn clusters is interesting in artificial water-splitting systems. An ultra-thin manganese oxide ( $\text{MnO}_x$ ) was selected as a co-catalyst to modify the surface of  $\text{BiVO}_4$  photoanode by a spray pyrolysis method [209]. The PEC measurements demonstrated that the surface charge transport efficiency strikingly increased by the  $\text{MnO}_x$  modification. After applying Ar plasma to the  $\text{BiVO}_4/\text{MnO}_x$  sample, the transport efficiency further increased, and it was around 7 times higher compared with that of pristine  $\text{BiVO}_4$  samples. The remarkable

PEC performance could be attributed to the increased charge carrier density, extended carrier lifetime, and additional exposed Mn active sites on the BiVO<sub>4</sub> surface [209].

An  $\alpha$ -Mn<sub>2</sub>O<sub>3</sub>/FTO electrocatalyst was used in nonaqueous (CH<sub>3</sub>CN and DMF) and aqueous 0.1 M KPi (pH 7.0) solutions for kinetic studies of heterogeneous water oxidation. The rate of water oxidation was first order in catalyst concentration and in H<sub>2</sub>O concentration. The square wave and cyclic voltammetry measurements revealed the stepwise proton-coupled electron transfer oxidations of the active Mn<sup>II</sup>-OH<sub>2</sub> site to Mn<sup>III</sup>-OH and then to Mn<sup>IV</sup>=O and finally an electron transfer oxidation of Mn<sup>IV</sup>=O to Mn<sup>V</sup>=O species. The Mn<sup>V</sup>=O species undergoes a rate-limiting O atom transfer to H<sub>2</sub>O to give a Mn<sup>III</sup>-OOH<sub>2</sub> species that, in turn, undergoes further oxidations to release O<sub>2</sub> [61].

An Mn-K cluster was investigated for electrochemical water oxidation. By using XAS, SEM, TEM, XRD, FTIR spectroscopy, and electrochemical methods, it was revealed that conversion into nanosized Mn oxides occurred for the cluster, and the nanosized Mn oxides are the true catalyst for water oxidation [210].

The Mn<sub>3</sub>O<sub>4</sub> nanocatalyst, which exhibits superb catalytic activity for water oxidation under neutral conditions, was analyzed for the complex capacitance. By the change in Mn valence between Mn<sup>II</sup> and Mn<sup>IV</sup>, the charge was accumulated on the catalyst surface prior to the rate-determining O-O bond-forming step. The dissipation ratio was proposed for understanding the energy balance between charge accumulation and charge consumption for chemical O-O bond formation [211]. In Mn<sub>3</sub>O<sub>4</sub> nanoparticles, a profile imaging technique was exploited to understand the correlation between surface atomic structures and the OER. The surface structures of Mn<sub>3</sub>O<sub>4</sub> nanoparticles were changed by the reaction and the surface Mn ions were reconstructed. The commonly considered active sites disappeared from the reconstructed planes, whereas Mn ions were still exposed at the edges of nanoparticles. Thus, the surface reconstructions can deactivate low-index surfaces of Mn oxides in the OER process, which was further validated by DFT calculations [212].

An Mn<sup>VII</sup>=O intermediate during electrocatalytic water oxidation by a c-disordered  $\delta$ -MnOx was identified as an onset-potential-dependent reduction peak at 0.93 V. This intermediate is proven to be highly reactive and much more oxidative than permanganate ion. Thus, a new catalytic mechanism for water oxidation catalyzed by Mn oxides was proposed with the involvement of the Mn<sup>VII</sup>=O intermediate in a resting state and the Mn<sup>IV</sup>-O-Mn<sup>VII</sup>=O as a real active species for O-O bond formation. Figure 15 shows the proposed catalytic cycle, involving Mn<sup>VII</sup>=O, in the MnOx-catalyzed water-oxidation reaction. The overall mechanistic process involves charge accumulation (S<sub>0</sub>/S<sub>3</sub>), charge rearrangement (S<sub>3</sub>/S<sub>4</sub>), active-state formation (S<sub>4</sub>/S<sub>4'</sub>), and oxygen evolution (S<sub>4'</sub>/S<sub>0</sub>) [68].

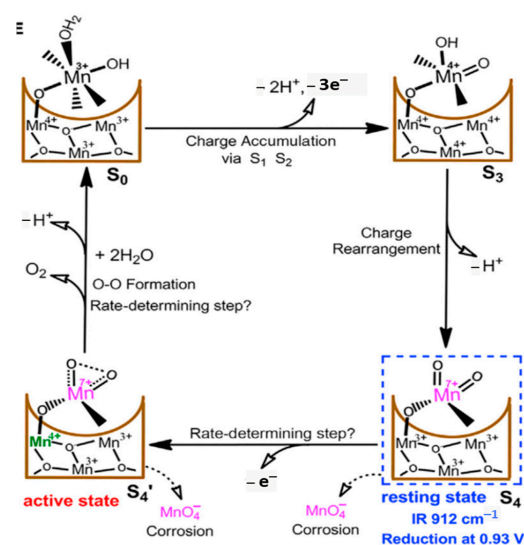


**Figure 15.** Proposed mechanism in MnO<sub>x</sub>-catalyzed OER. Reproduced from *iScience* 2018 [68] under the license of CC BY 4.0 of Elsevier.

### 6.7.5. Mixed Metal Oxides

Two or three transition metals are mixed to form oxides of high electrocatalytic performance for water electrolyzers at a low cost. An NiFe oxide catalyst was employed as the anode catalyst with an NiMo oxide cathode catalyst with a high-performance perovskite-Si tandem solar cell, achieving a record 20% STH efficiency [213]. Nickel ferrite,  $\text{NiFe}_2\text{O}_4$ , cobalt ferrite, and  $\text{CoFe}_2\text{O}_4$ , are efficient and promising anode catalyst materials in the field of electrochemical water splitting.

In Ni-Fe water oxidation electrocatalysts, Ni is likely not an active site for water oxidation, because Ni cannot achieve high-oxide states in aqueous environments at relevant potentials [214]. For the OER of  $\text{NiFeO}_x\text{H}_y$ , the addition of  $\text{Co}^{2+}$  cation increased the current density by 32.7% by the cation transport effect [215]. Using operando XAS, it was revealed that Ni oxidizes from the initial +2 oxidation state to the +3/+4 state [216]. For Ni-Fe oxyhydroxides, in situ monitoring of the Fe active site number and turn-frequency number provided important insights into the activity degradation/regeneration caused by Fe dissolution/adsorption as well as site-dependent activity and stability [217]. In the case of  $\text{NiFe}_2\text{O}_4$ , an Fe-site-assisted LOM pathway as the preferred OER mechanism was predicted. On the other hand, in the case of  $\text{CoFe}_2\text{O}_4$ , an Fe-site-assisted LOM pathway and a Co-site-assisted AEM pathway could both play a role [218].

Amorphous/crystalline  $\text{NiFe}_2\text{O}_4$  induced by vanadium doping showed a superior electrocatalyst and long-term stability [219]. For amorphous Ni-Fe mixed metal oxides, analysis of the XAS revealed local structural transitions. A dual-site OER reaction mechanism was proposed, in which potential and rate-determining steps occur at Ni and Fe sites, respectively [220].

An Fe/Ca-based bimetallic oxide,  $\text{CaFe}_2\text{O}_4$ , exhibited outstanding OER activity in alkaline media. DFT calculations suggested an unconventional mechanism via the direct formation of O–O bonds between two oxygen intermediates, which are adsorbed on a multi-iron site on the catalyst surface [221].

On spinel  $\text{NiCo}_2\text{O}_4$  abundant Co defects were preferentially produced by tuning the M–O bond length. Theoretical calculations and experiments proved that Al doping elongated the Co–O bond and promoted the ionization of Co under plasma treatment [222]. Spinel  $\text{Co}_2\text{MnO}_4$  showed higher OER activity, most probably due to the ideal binding energies of the OER intermediates [223].

For modulated  $\text{NiFeX}$  and  $\text{FeCoX}$  ( $X = \text{W}, \text{Mo}, \text{Nb}, \text{Ta}, \text{Re}, \text{and MoW}$ ) oxyhydroxide catalysts, in situ and ex situ soft and hard XAS were used to characterize the oxidation transition and facilitate the lower OER overpotential [224].  $(\text{Co-Fe-Pb})\text{O}_x$  in acidic solutions through a cobalt-selective self-healing mechanism was investigated. The kinetics of the process were investigated by soft XAS and it was revealed that low concentrations of  $\text{Co}^{2+}$  in the solution stabilize the catalytically active Co(Fe) sites [225].

### 6.8. Layered Double Hydroxide (LDH)

LDH are emerging catalyst materials with inner layer water molecules and higher anion exchange capacity. They have been extensively used as electrocatalytic materials owing to their high specific surface area, environmental friendliness, lower cost, and non-toxicity [226]. A kind of LDH itself may become photocatalysts for water splitting. The electronic properties, such as band structure, bandgap energy ( $E_g$ ), density of states (DOS), and band edge placement for  $\text{M}^{\text{II}}\text{M}^{\text{III}}\text{-LDHs}$  ( $\text{M}^{\text{II}} = \text{Mg}, \text{Co}, \text{Ni}$  and  $\text{Zn}$ ;  $\text{M}^{\text{III}} = \text{Al}$  and  $\text{Ga}$ ) were calculated by using the DFT + U method. The band structures of Mg- and Zn-based LDHs and Co- and Ni-based LDHs are responsive to ultraviolet ( $E_g > 3.1$  eV) and visible light ( $E_g < 3.1$  eV), respectively. The DOS calculations revealed that the photogenerated hole localizes on the surface hydroxyl group of LDHs, facilitating the oxidization of a water molecule without a long transportation route. The band edge placements of NiGa-, CoAl-, ZnAl-, and NiAl-LDHs have a driving force (0.965 eV, 0.836 eV, 0.667 eV, and 0.426 eV, respectively), toward oxygen evolution. In the experimental observations, only

CoAl-LDH was an efficient oxygen evolution photocatalyst, agreeing well with the theoretical prediction [227].

For NiFe-LDH and Ni-LDH, the critical role of superficial oxygen vacancies in enhancing electronic transport was discussed based on the electrochemical analysis by correlating with electrocatalytic activities [228]. The in situ conversion process to yield a monolayer of Ni(OH)<sub>2</sub> on electrodes was presented and the dynamic active site of the monolayer promoted the OER process. Doping with Co caused the oscillation of Ni and Co valence states in NiCo hydroxide. This study defined an in situ conversion process to yield monolayer LDH and a fundamental understanding of the origin of the active sites in monolayer LDHs for the OER [229]. Direct spectroscopic evidence for the different active sites in Fe-free and Fe-containing Ni oxides was reported for ultrathin LDH samples. <sup>18</sup>O-labeling experiments in combination with in situ Raman spectroscopy were employed to probe the role of lattice oxygen as well as an active oxygen species, NiOO<sup>−</sup>, in the catalysts. It was found that lattice oxygen is involved in the OER for Ni and NiCo-LDHs, but not for NiFe and NiCoFe-LDHs. Moreover, NiOO<sup>−</sup> is a precursor to oxygen for Ni and NiCo-LDHs, but not for NiFe and NiCoFe-LDHs [78]. For M-doped Ni-based LDH (M = Ni, Co, and Fe), the OER mechanism was investigated theoretically for the reaction processes of AEM, LOM, and IMOC (= intramolecular oxygen coupling) mechanism. Theory predicted overpotential and Tafel slopes, and the findings were in agreement with the observation. As a result, depending on the applied potential, the reaction mechanism changed [230]. In addition to electrocatalysts, NiFe-LDH may be used as the flexible electrode of Zinc-Air batteries [231].

For the Cu-NiFe-LDH electrocatalyst, a novel magnetic Fe<sup>III</sup> site spin-splitting strategy was suggested [232]. The electronic structure and spin states of the Fe<sup>III</sup> sites are effectively induced by the Jahn–Teller effect of Cu<sup>2+</sup>. The theoretical calculations and operando ATR FTIR revealed that the facilitation for the O–O bond formation accelerated the production of O from OH and improved the OER activity [232]. For as-prepared sulfated Co-NiFe-LDH nanosheets, the kinetic energy barrier of the O–O coupling is significantly reduced. The formation of M-OOH on the active site at low overpotential was directly confirmed in 1 M KOH solution by in situ Raman and charge transfer fitting results. In a weakly alkaline environment of 0.1 M KOH, a sequential proton–electron transfer mechanism replaces the concerted proton–electron transfer mechanism, and the proton transfer step becomes the rate-determining step (RDS) as illustrated in Figure 16 [233].

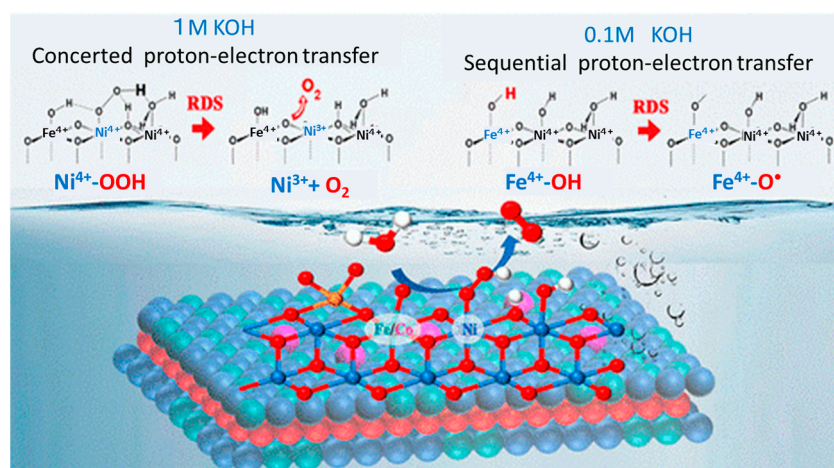


**Figure 16.** For Co-NiFe-LDH nanosheet, weakening alkaline concentration changes rate-determining step (RDS) from the release of O<sub>2</sub> to the oxo radical formation. Reproduced from *ACS Nano* 2023 [233] with permission from the American Chemical Society.

A Pt-induced NiFe-LDH (Pt-NiFe LDH) nanosheet was synthesized and large current density electrodes could be achieved in OER as well as HER [234]. At NiO/NiFe-LDH, the adsorption energy of \*OH and \*OOH can be adjusted independently, so as to bypass

the scaling relationship and achieve high catalytic performance [235]. ZnO nanoparticles are uniformly distributed on the NiFe-LDH nanoflowers, which are prepared uniformly on the three-dimensional porous Ni foam. The active sites changed from Fe cations to Ni cations during OER and the OER dynamics were significantly improved [236]. The hierarchical bimetal nitride/hydroxide (NiMoN/NiFe LDH) array exhibits the industrially required current density. In situ electrochemical spectroscopy reveals that a hetero interface facilitates dynamic structure evolution to optimize the electronic structure. Operando EIS measurement implied the accelerated OER kinetics and intermediate evolution due to fast charge transport. For the OER mechanism, the combination of theoretical and experimental studies revealed that as-activated NiMoN/NiFe-LDH follows an LOM process with accelerated kinetics [237].

NiFe LDH@Ni<sub>3</sub>S<sub>2</sub> heterostructure as an efficient bifunctional electrocatalyst for overall water splitting was prepared. Three-dimensional porous heterostructure arrays caused good electrocatalytic activity with a low Tafel slope [238]. By incorporating a semiconductor CdS/CdSe-MoS<sub>2</sub> and NiFe-LDH for the OER, the as-prepared photoelectrode required a potential lower than the theoretical water splitting potential. Operando XAS measurements revealed that the formation of highly oxidized Ni species under illumination provides large photocurrent gains [239]. Hetero structures of LDH with graphitic carbon nitride (g-C<sub>3</sub>N<sub>4</sub>) stand as promising photo- and electro-catalysts for water oxidation and reduction. Mechanisms involved in electrocatalytic, photocatalytic, and photoelectrocatalytic water splitting processes were reviewed with the necessary insights on the material [240]. By taking CuTi-LDH@g-C<sub>3</sub>N<sub>4</sub> and Bi<sub>2</sub>O<sub>2</sub>CO<sub>3</sub>/NiFe-LDH@g-C<sub>3</sub>N<sub>4</sub> as examples, the importance of heterojunctions and interfacial chemistry in the water-splitting mechanism was explained in detail [240].

### 6.9. Metal–Organic Framework (MOF)

MOF-derived materials have been demonstrated with high surface area, porous structure, increased electron transport, accessible active sites, and tailorable properties. And then they may provide a new route for designing the catalysts with excellent electrochemical water oxidation activity [241]. Singh et al. discussed the MOF-derived electrocatalysts by electronic structure modulation since the recent studies of MOF-derived electrocatalysts mainly focused on morphological development, crystal structure modulation, facet engineering, and enhancement of the electrochemical surface area [241]. As the controlling factors for efficient OER, discussed were e<sub>g</sub> orbital filling, metal–oxygen covalency, mixed valency of metal ions, octahedral vs. tetrahedral occupancy of the metal ions, and vacancy engineering. To improve the OER activity and stability of the MOF catalysts, tuning the electronic properties by interfacial modulation, surface overlayer, Fermi level manipulation, self-supported strategy, and heterostructure formation have been addressed [241].

FeNi–tannic acid coordination crystal was in situ grown on Ni foam ((FeNi)–Tan/NF) to directly catalyze the OER, and it exhibited predominant electrocatalytic OER activity [242]. A series of MOFs; FeM-MOF (M = Fe, Co, Ni, Zn, Mn; H<sub>4</sub>L = 3,3,5,5'-azoxybenzenetetracarboxylic acid) were synthesized under a simple and mild condition. Among them, the FeCo-MOF catalyst exhibits an extremely low overpotential and small Tafel slope in an alkaline electrolyte for OER, which had far exceeded the commercial catalyst IrO<sub>2</sub> [243].

The surface reconstruction phenomenon of MOF-based nanomaterial electrocatalysts for OER was summarized, and the effects of structural and compositional transformation on the catalytic activity were discussed because many MOF-based catalysts inevitably undergo irreversible surface reconstruction during the redox process [244]. The causes and conditions of surface reconstruction and its influence on OER performance were also discussed, demonstrating the structure–activity relationship between surface reconstruction and catalytic performance [244]. A facile impregnation method through an ion-exchange process to fabricate Fe-doped Co-BDC nanosheets (Fe@Co-BDC NSs, BDC = benzenedicarboxylic) was proposed, though most of the related reports focus on the hydrothermal

methods to prepare the mixed-metal MOFs. For an efficient OER electrocatalyst, the morphology change and the electronic structure of Fe@Co-BDC NSs were important to represent significant enhancement in the activity [245].

For MOF-based catalysts, in situ or operando Raman spectroscopic studies are useful to identify the adsorption sites, defect sites, structural or spin transitions, reaction centers, intermediates, and so on. Sunil et al. reviewed the current research for OER mechanisms with Raman spectroscopy in probing the structure, guest adsorption, catalytic activity, and reaction mechanisms of MOFs [246]. MOFs may become alternative OER catalysts because in situ self-reconstruction from MOFs to (oxy)hydroxides could be performed in alkaline electrolytes. Thus, Fe-doped Co-MOF nanosheets were prepared and utilized straightforwardly as OER electrocatalysts. CoFe-layered bimetallic hydroxides (CoFe-LDHs) with abundant active sites, which are generally actual active species, were obtained from in situ conversion of Co-MOF/Fe after etching by the KOH electrolyte. [247].

A new MOF with well-defined Co–Mo dual sites, HZIF-2-CoMo, (HZIF = Hybrid zeolitic imidazolate framework), was reported, which can promote the OER process through an unconventional Mo/Co dual-site relay mechanism. Theoretical calculations suggested that the Mo and Co sites stabilize the \*OH and \*OOH intermediates, respectively, and that the unique Co–O–Mo configuration induces the formation of a Co–O\*–Mo transition intermediate, remarkably reducing the reaction-free energy. As a result, HZIF-2-CoMo showed one of the best OER electrocatalysts reported [248].

Two-dimensional cobalt ion ( $\text{Co}^{2+}$ ) and benzimidazole (bIm)-based zeolite imidazole framework nanosheets were reported as exceptionally efficient electrocatalysts for the OER. Liquid-phase ultrasonication was applied to exfoliate a  $\text{Co}_4(\text{bIm})_{16}$  zeolite imidazole framework (ZIF) into nanoscale sheets. The electrochemical and physicochemical characterization data supported that the OER active site is assigned to nitrogen-coordinated cobalt oxyhydroxide,  $\text{N}_4\text{CoO}(\text{OH})$ , of the exfoliated nanosheet, following a mechanism known for Co-porphyrin and related systems as shown in Figure 17 [249].

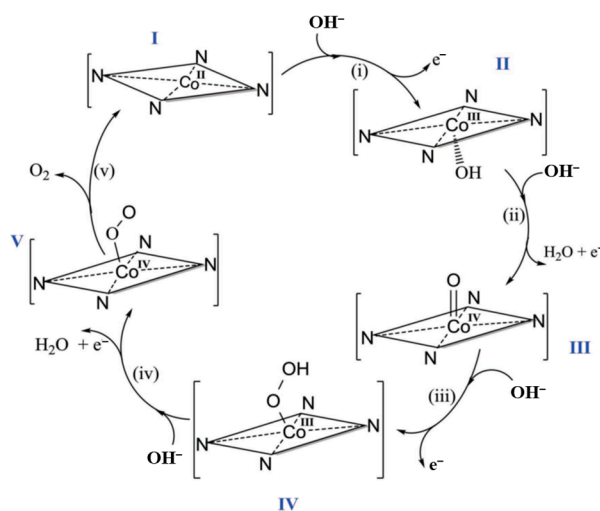


**Figure 17.** Proposed scheme of the nature of the active site of the exfoliated Co-ZIF-9(III) 2D catalyst and the underlying mechanism of the OER. Reproduced from *Adv. Sci.* **2018** [249] under the license of CC BY 4.0 of John Wiley & Sons, Inc.

### 6.10. Metal Complexes

Since the  $\text{CaMn}_4\text{O}_5$  cluster in PS II can catalyze the OER with a very low overpotential, it is expected that multinuclear water oxidation catalysts possess superior OER performances. Inspired by the  $\text{CaMn}_4\text{O}_5$  cluster in PS II, some multinuclear complexes were synthesized that could catalyze water oxidation [250]. Mimicking the  $\text{Mn}_4$  cluster, an artificial  $\text{Mn}_4$  oxide cluster was proposed from the DFT calculation. The cluster may act as an OER catalyst because the ability of electron and proton transfers was theoretically

exhibited [251]. Since the degradation of organic ligands is an inevitable characteristic of molecular catalysts, the ligands that pose the ability for electron transfer come under consideration [250]. By referring to the molecular mechanism of PS II, redox-active ligands were employed for metal complex catalysts and then an achievement of current efficiency of 100%, overpotential of 200–300 mV, and a turnover frequency of  $100\text{s}^{-1}$  has been reported [250].

Mainly with Ru, Mn, and Ir, metal complex catalysts for artificial OER were investigated at the beginning. However, recent investigations shift to non-precious natural abundant metals, such as Fe, Co, Ni, and Cu, and grow with understanding of proton-coupled electron transfer and O–O bond formation [252]. Recently, some mononuclear heterogeneous catalysts showed a high OER activity, which testified that mononuclear active sites with suitable coordination surroundings could also catalyze water oxidation efficiently. Though some mononuclear molecular complexes for OER show high water oxidation activity, it cannot be excluded that the high activity arises from the formation of dimeric species. The development of mono-/multi-nuclear homo and heterogeneous catalysts for water oxidation was focused on in a review paper [253]. This review also provided active sites and possible catalytic mechanisms of OER on the mono-/multi-nuclear catalysts [253]. Karmakar summarized the progress in research on molecular catalysts based on transition metals in the homogeneous phase while emphasizing the current mechanistic understanding of the water oxidation reaction. The factors that influence the character of water oxidation catalysts, such as reaction conditions, attached ligands, and transition metal centers, have been discussed as well [254].

#### 6.10.1. Mn Complexes

An electrocatalytic water oxidation reaction with  $\text{Mn}^{\text{III}}$  tris(pentafluorophenyl) corrole (MTPC) in propylene carbonate (PC) was reported.  $\text{O}_2$  was generated at the  $\text{Mn}^{\text{V/IV}}$  potential with hydroxide, but a more anodic potential was required to evolve  $\text{O}_2$  with only water. With a synthetic  $\text{Mn}^{\text{V}}(\text{O})$  complex of MTPC, a second-order rate constant was determined with hydroxide, whereas its reaction with water occurred much more slowly. Significantly, during the electrolysis of MTPC with water, an  $\text{Mn}^{\text{IV}}$ -peroxo species was identified with various spectroscopic methods, including UV–Vis, EPR, and FTIR spectroscopies. Isotope labeling experiments confirmed that both O atoms of this peroxo species are derived from water, suggesting the involvement of the water nucleophilic attack (WNA) mechanism in water oxidation. DFT calculations suggested that the nucleophilic attack of hydroxide on  $\text{Mn}^{\text{V}}(\text{O})$  and also WNA to one electron-oxidized  $\text{Mn}^{\text{V}}(\text{O})$  are feasibly involved in the catalytic cycles but that direct WNA to  $\text{Mn}^{\text{V}}(\text{O})$  is not likely to be the main O–O bond formation pathway in the electrocatalytic OER by MTPC [72].

#### 6.10.2. Fe Complexes

A pentanuclear Fe complex was reported as an efficient and robust OER catalyst with a turnover frequency of  $1900\text{ s}^{-1}$ , which is about three orders of magnitude larger than that of other Fe-based catalysts. The electrochemical analysis confirmed the redox flexibility of the system, characterized by six different oxidation states between  $\text{Fe}^{\text{II}}_5$  and  $\text{Fe}^{\text{III}}_5$ , where the  $\text{Fe}^{\text{III}}_5$  state is active for oxidizing water. Quantum chemistry calculations indicated that the presence of adjacent active sites facilitates O–O bond formation with a low reaction barrier [255].

The kinetics of water oxidation by  $\text{K}_2\text{FeO}_4$  have been reinvestigated by UV/Vis spectrophotometry at pH 7–9 in 0.2 M phosphate buffer. The rate of reaction was found to be second-order in both  $[\text{FeO}_4^{2-}]$  and  $[\text{H}^+]$ . These results are consistent with a proposed mechanism in which the first step involves the initial equilibrium protonation of  $\text{FeO}_4^{2-}$  to give  $\text{FeO}_3(\text{OH})^-$ , which then undergoes rate-limiting O–O bond formation. Analysis of the  $\text{O}_2$  isotopic composition for the reaction in  $\text{H}_2^{18}\text{O}$  suggests that the predominant pathway for water oxidation is intramolecular O–O coupling. DFT calculations supported the proposed mechanism [256].

### 6.10.3. Cu Complexes

With a family of Cu<sup>II</sup> o-phenylene bis-oxamidate complexes, the reactivity sequence for the OER was found to be a function of the substitution pattern on the periphery of the aromatic ring. In situ EPR, FTIR, and spectroelectrochemistry suggested that ligand-centered oxidations were preferred over Cu-centered oxidations. The resonance Raman spectroelectrochemical study revealed the accumulation of a bis-imine bound Cu<sup>II</sup> superoxide species under catalytic turnover as the reactive intermediate, which provides evidence for the O–O bond formation during the OER process [79]. Bearing the redox-active HL ligand, Cu<sup>II</sup>(HL)(OTf)<sub>2</sub> (HL = N,N-bis(2,2'-bipyrid-6-yl)amine, OTf = triflate) was investigated for an OER catalyst. This Cu catalyst was found to be active as an OER catalyst at pH 11.5, at which the deprotonated complex [Cu<sup>II</sup>(L<sup>-</sup>)(H<sub>2</sub>O)]<sup>+</sup> is the predominant species in the solution. The overall OER mechanism was found to be initiated by two proton-coupled electron-transfer steps. Kinetically, a first-order dependence in the catalyst and a zeroth-order dependence in the phosphate buffer were found. A computational study supported the formation of a Cu–oxyl intermediate, [Cu<sup>II</sup>(L•)(O•)(H<sub>2</sub>O)]<sup>+</sup>. From this intermediate onward, the O–O bond is formed via a single-electron transfer from an approaching hydroxide ion to the ligand. Throughout the mechanism, the Cu<sup>II</sup> center is proposed to be redox-inactive [257].

The mechanism of OER catalyzed by a mononuclear Cu complex in alkaline conditions was studied by DFT calculations and shown in Figure 18. Firstly, a water molecule coordinating with the Cu center of the Cu<sup>II</sup> complex generates the complex of Cu<sup>II</sup>–H<sub>2</sub>O. This complex undergoes two proton-coupled electron transfer processes to produce an intermediate (•L–Cu<sup>II</sup>–O•), which can be described as a Cu<sup>II</sup> center interacting with a ligand radical antiferromagnetically and an oxyl radical ferromagnetically. The oxidation process occurs mainly on the ligand moiety, which can trigger O–O bond formation via the WNA mechanism. The attacking water transfers one of the protons to the HPO<sub>4</sub><sup>2-</sup> coupled with an electron transfer to the ligand radical, which generates a transient •OH interacting with the oxyl radical and H<sub>2</sub>PO<sub>4</sub><sup>-</sup>. Then, the O–O bond is formed through the direct coupling of the oxyl radical and the OH radical. The triplet di-oxygen could be released after two oxidation processes. The O–O bond formation was suggested to be the rate-limiting step. Thus, the Cu complex catalyzes water oxidation with the help of a redox non-innocent ligand and HPO<sub>4</sub><sup>2-</sup> [258].

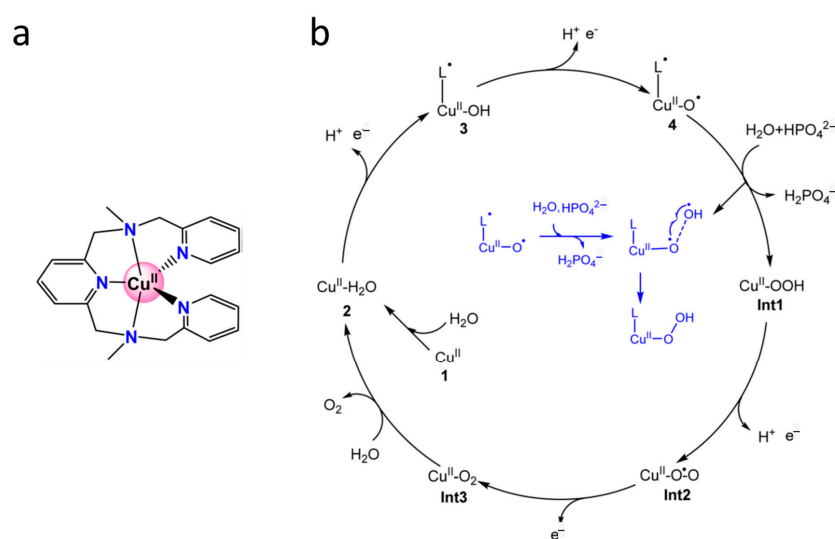


**Figure 18.** (a) Schematic representation of the Cu complex used in the calculation. (b) Proposed catalytic cycle for water oxidation catalyzed by the Cu complex. The O–O bond formation process is shown at the inset. Reproduced from *RSC Adv.* 2023 [258] with permission from the Royal Society of Chemistry.

### 6.11. Single-Atom Catalysts (SACs)

During the past few years, several research efforts have also unveiled the immense potential of SACs for the OER. Excellent OER performance has been demonstrated for both noble metal and non-noble metal SACs with lab-scale electrodes. The long-term stability of promising SACs is less well explored though, and considerable efforts are still required to assess this under technologically relevant conditions [259].

Atomically dispersed Ir atoms incorporated into spinel  $\text{Co}_3\text{O}_4$  lattice as an acidic OER catalyst were reported to exhibit excellent activity and stability for water oxidation. FTIR observation of  $^*\text{OOH}$  indicates that the AEM rather than the LOM dominates the OER process [83]. An electrocatalyst with Ru-atom-array patches supported on  $\alpha\text{-MnO}_2$  (Ru/ $\text{MnO}_2$ ) for the OER was investigated. Ru/ $\text{MnO}_2$  showed a high activity and outstanding stability with small degradation after 200 h operation. Operando vibrational and mass spectroscopy measurements were performed to probe the reaction intermediates and gaseous products for validating the OER pathway, suggesting a mechanism that involves only  $^*\text{O}$  and  $^*\text{OH}$  species as intermediates. This mechanism allows direct O–O radical coupling for  $\text{O}_2$  evolution, i.e., OPM process in Figure 3c was suggested. First-principles calculations confirmed the cooperative catalysis mechanism with a reduced energy barrier. Time-dependent elemental analysis demonstrated the occurrence of the in situ dynamic cation exchange reaction during the OER, which is the key for triggering the reconstruction of Ru atoms into the ordered array with high durability [80].

A macromolecule-assisted SAC providing high-density Co single atoms (10.6 wt% Co) in a pyridinic N-rich graphenic network was reported [260]. The highly porous carbon network with increased conjugation and vicinal Co site decoration significantly enhanced the electrocatalytic OER in 1 M KOH with more than 300 h stability. Operando X-ray absorption near-edge structure demonstrated the formation of electron-deficient Co–O coordination intermediates, accelerating OER kinetics [260].

A representative set of 11 transition metal atoms (Sc, V, Ti, Cr, Mn, Fe, Co, Ni, Cu, Pd, Pt) anchored on nitrogen-doped graphene were considered by means of DFT calculations [261]. Most of them form stable superoxo and peroxo intermediates when they react with molecular oxygen, which has a direct impact on the OER. Thus, in the corresponding microkinetic models, this step of the reaction cannot be neglected. A representative Gibbs energy profile is shown in Figure 19. Depending on the transition metal atom, the inclusion of the superoxo/peroxo complexes in the analysis of the reaction profile can change the kinetics by several orders of magnitude [261]. To clarify the assignment of the intermediates, a DFT technique was applied to a set of 30 SACs made by ten metal atoms (Sc, Ti, V, Cr, Mn, Fe, Co, Ni, Pd, and Pt) anchored on three widely used 2D carbon-based materials; graphene, nitrogen-doped graphene, and carbon nitride. On SACs, it has been generally assumed that OER occurs via the formation of three intermediates,  $^*\text{OH}$ ,  $^*\text{O}$ , and  $^*\text{OOH}$  species, they could be referred to as  $\text{M}(\text{OH})$ ,  $\text{M}(\text{O})$ , and  $\text{M}(\text{OOH})$ . In all cases, however, other intermediates  $\text{M}(\text{OH})_2$ ,  $\text{M}(\text{O})(\text{OH})$ ,  $\text{M}(\text{O})_2$ , and  $\text{M}(\text{O}_2)$  were formed with higher stabilities [262].

Compared with SACs, dual-atom catalysts (DACs) are attracting more attention including higher metal loading, more versatile active sites, and excellent catalytic activity. Several general synthetic strategies and structural characterization methods of DACs were introduced, and the involved catalytic mechanisms were discussed in the review paper [263]. Dual-atom catalysts, particularly those with heteronuclear active sites, have the potential to outperform the well-established single-atom catalysts for OER. A large-scale DFT is employed to explore the feasibility of the  $^*\text{O}$ - $^*\text{O}$  coupling mechanism, which can circumvent the scaling relationship by improving the catalytic performance of N-doped graphene-supported Fe-, Co-, Ni-, and Cu-containing heteronuclear dual-atom catalysts [264].

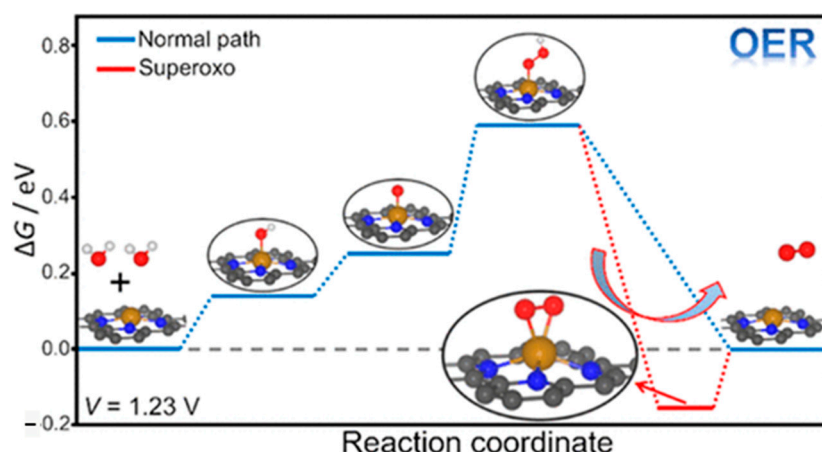


**Figure 19.** Representative Gibbs energy profile of OER over a single-atom catalyst (SAC). Reproduced from *ACS Catal.* **2022** [261] with permission from the American Chemical Society.

### 6.12. Effect of Surface Functionalization

It has been found that the addition of carbonate salts to Pt-loaded TiO<sub>2</sub> suspensions led to highly efficient stoichiometric photocatalytic decomposition of liquid water into H<sub>2</sub> and O<sub>2</sub>. Since a high concentration of carbonate ions is essential for the catalytic photodecomposition of water, it was considered that the carbonate species aids the desorption of O<sub>2</sub> from the TiO<sub>2</sub> surface [265]. To elucidate the effect of carbonates, DFT calculations are performed to study the photoinduced H<sub>2</sub>O and H<sub>2</sub>CO<sub>3</sub> oxidation mechanisms on TiO<sub>2</sub> and BiVO<sub>4</sub> [266]. The computational results verify that the adsorbed H<sub>2</sub>CO<sub>3</sub> molecule is easily photo-oxidized compared with the adsorbed H<sub>2</sub>O molecule, facilitating the formation of the peroxide intermediate and improving O<sub>2</sub> evolution and H<sub>2</sub>O<sub>2</sub> production [266].

The use of surface functionalization with phosphate ion groups (Pi) enhances the interfacial proton transfer. As the results, the Pi functionalization on La<sub>0.5</sub>Sr<sub>0.5</sub>CoO<sub>3-δ</sub> and LaCoO<sub>3</sub> gave rise to a significant enhancement of the OER activity when compared to La<sub>0.5</sub>Sr<sub>0.5</sub>CoO<sub>3-δ</sub> and LaCoO<sub>3</sub>, respectively. It was demonstrated that the surface functionalization by Pi enhanced the activity when the OER kinetics are limited by the proton transfer as shown in Figure 20. By Sr<sup>2+</sup> cation substitution, O 2p band closed to the Fermi level, assisting the deprotonation step from -OOH to -OO•. Thus, depending on the position of the Fermi level, the function of Pi changed from keeping water near the surface to assisting the deprotonation reaction [267].

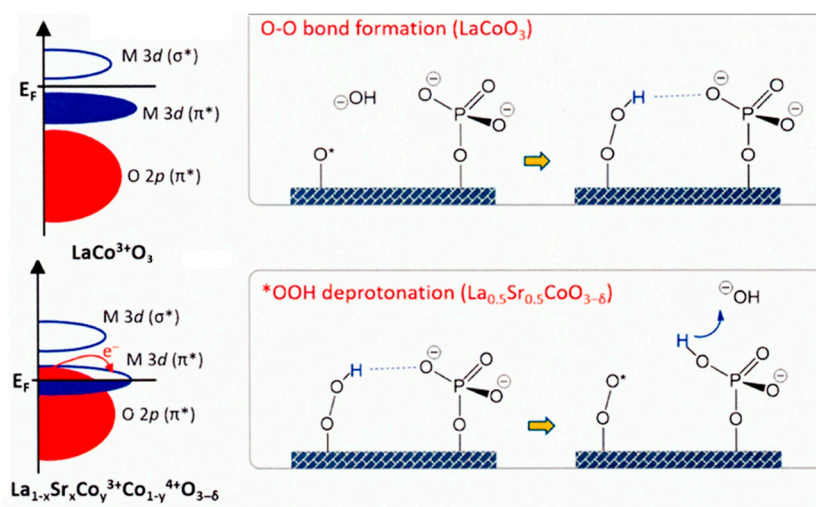


**Figure 20.** Proposed mechanisms to improve the OER activity of perovskite catalysts. Reproduced from *J. Phys. Chem. Lett.* **2017** [267] with permission from the American Chemical Society.

The hydrated cobalt phosphate (CoPi) co-catalyst was investigated for O–O bond and OOH formation, based on the conventional experimental findings. Theoretical calculations of hydrated CoPi cluster models elucidated the roles of phosphate as a source of oxygen and deliverer of protons, both of which result in the spontaneous formation of an O–O bond after the release of two electrons and two protons. The calculations also show that OOH formation proceeds subsequently depending on the spin electronic states of the hydrated CoPi surface, and O<sub>2</sub> formation then spontaneously progresses after the release of two electrons and two protons [268].

A proton acceptor, TA<sup>2-</sup> (terephthalate ion) can mediate proton transfer pathways by preferentially accepting protons, which optimizes the O–H adsorption/activation process and reduces the kinetic barrier for O–O bond formation. A proton-transfer-promotion mechanism for OER electrocatalysts with FeO<sub>6</sub>/NiO<sub>6</sub> units is proposed by in situ Raman spectroscopy, catalytic tests, and theoretical calculations [269].

The strong adsorption of hexadecyl trimethyl ammonium cations on the surface of electrocatalysts provides the increased absolute number of OH<sup>-</sup> ions near the electrocatalyst surface, which effectively promotes the OER performance of electrocatalysts, such as Fe<sub>1-y</sub>Ni<sub>y</sub>S<sub>2</sub>@Fe<sub>1-x</sub>Ni<sub>x</sub>OOH micro platelets and SrBaNi<sub>2</sub>Fe<sub>12</sub>O<sub>22</sub> powders [270].

## 7. Perspectives

In the brimming research articles of the OER developments, the catalysts for electrolyzers (electrocatalysts) are dominant because they are actually working in industries. These catalysts for electrolyzers may not be directly applied for artificial photosynthesis using photoelectrodes or photocatalysts. However, the molecular mechanism is surely applicable under the consideration of difference in the reaction conditions. Since the electrochemical OER catalysts are used with electrolytes, they usually work in alkaline or acid solution. However, photoelectrodes and photocatalysts are usually used in moderate pH values. Then, the most attention should be paid to the pH effects on the reaction mechanism when electrocatalysts are consulted for photocatalysts.

Nature assembled PS II with CaMn<sub>4</sub>O<sub>5</sub> clusters as the ultimate OER catalysts. Compared with the present artificial catalysts, the molecular mechanism of the PS II catalytic reaction is different in the following issues. (i) Immediately after the O–O bond formation O<sub>2</sub> is released from the cluster, while the lifetime of the \*OO<sup>-</sup> or \*OO\* in artificial catalysts is so long to be easily detected. Therefore, the catalysts, of which O–O intermediate species can be detected, may not be really generalized as a good catalyst. (ii) In the CaMn<sub>4</sub>O<sub>5</sub> cluster, the four transition metals share each positive hole to give four Mn<sup>IV</sup> ions. In the case of artificial OER catalysts, one or two metal ions participate the four-electron reaction. Therefore, intermediate species of the OER should receive the next hole at the same metal ions. Namely, the catalysts of AEM process may have a difficulty to improve the activity. Then, catalysts with more than one metal atom appear promising in the future. (iii) The pathways of proton and water molecules are controlled in the PS II process. To keep the pathways, the surroundings of the Mn<sub>4</sub> cluster is rather hydrophobic. The artificial OER catalysts are usually surrounded by water molecules and the whole surface of the catalysts can adsorb water molecules. To improve the OER activity of the artificial catalysts, controlling the proton transfers may become important, and it could be achieved by the surface functionalization of the present catalysts. The discussion in Section 6.12 may provide a clue to the improvement of the OER activity.

**Funding:** This research received no external funding.

**Institutional Review Board Statement:** Not applicable.

**Informed Consent Statement:** Not applicable.

**Data Availability Statement:** Not applicable.

**Acknowledgments:** The author thanks the Library of Kyoto University for access to the literature.

**Conflicts of Interest:** The author declares no conflict of interest.

## References

1. Hocke, K. Oxygen in the Earth System. *Oxygen* **2023**, *3*, 19. [[CrossRef](#)]
2. Nosaka, Y.; Nosaka, A.Y. Generation and detection of reactive oxygen species in photocatalysis. *Chem. Rev.* **2017**, *117*, 11302–11336. [[CrossRef](#)] [[PubMed](#)]
3. Yoshino, S.; Takayama, T.; Yamaguchi, Y.; Iwase, A.; Kudo, A. CO<sub>2</sub> reduction using water as an electron donor over heterogeneous photocatalysts aiming at artificial photosynthesis. *Acc. Chem. Res.* **2022**, *55*, 966–977. [[CrossRef](#)] [[PubMed](#)]
4. Nosaka, Y.; Nosaka, A. *Introduction to Photocatalysis: From Basic Science to Applications*; Royal Society of Chemistry: Cambridge, UK, 2016; 272p. [[CrossRef](#)]
5. Oliver, N.; Avramov, A.P.; Nürnberg, D.J.; Dau, H.; Burnap, R.L. From manganese oxidation to water oxidation: Assembly and evolution of the water-splitting complex in photosystem II. *Photosynth. Res.* **2022**, *152*, 107–133. [[CrossRef](#)] [[PubMed](#)]
6. Najafpour, M.M.; Zaharieva, I.; Zand, Z.; Hosseini, S.M.; Kouzmanova, M.; Hołyńska, M.; Tranca, I.; Larkum, A.W.; Shen, J.-R.; Allakhverdiev, S.I. Water-oxidizing complex in photosystem II: Its structure and relation to manganese-oxide based catalysts. *Coord. Chem. Rev.* **2020**, *409*, 213183. [[CrossRef](#)]
7. Yoneda, Y.; Arsenault, E.A.; Yang, S., Jr.; Orcutt, K.; Iwai, M.; Fleming, G.R. The initial charge separation step in oxygenic photosynthesis. *Nat. Commun.* **2022**, *13*, 2275. [[CrossRef](#)]
8. Suga, M.; Akita, F.; Sugahara, M.; Kubo, M.; Nakajima, Y.; Nakane, T.; Yamashita, K.; Umena, Y.; Nakabayashi, M.; Yamane, T.; et al. Light-induced structural changes and the site of O=O bond formation in PSII caught by XFEL. *Nature* **2017**, *543*, 131–135. [[CrossRef](#)]
9. Suga, M.; Akita, F.; Yamashita, K.; Nakajima, Y.; Ueno, G.; Li, H.; Yamane, T.; Hirata, K.; Umena, Y.; Yonekura, S.; et al. An oxyl/oxo mechanism for oxygen-oxygen coupling in PSII revealed by an X-ray free-electron laser. *Science* **2019**, *366*, 334–338. [[CrossRef](#)]
10. Kato, Y.; Noguchi, T. Redox properties and regulatory mechanism of the iron-quinone electron acceptor in photosystem II as revealed by FTIR spectroelectrochemistry. *Photosynth. Res.* **2022**, *152*, 135–151. [[CrossRef](#)]
11. Corry, T.A.; O'Malley, P.J. Evidence of O–O Bond formation in the final metastable S<sub>3</sub> state of nature's water oxidizing complex implying a novel mechanism of water oxidation. *J. Phys. Chem. Lett.* **2018**, *9*, 6269–6274. [[CrossRef](#)]
12. Rummel, F.; O'Malley, P.J. How nature makes O<sub>2</sub>: An electronic level mechanism for water oxidation in photosynthesis. *J. Phys. Chem. B* **2022**, *126*, 8214–8221. [[CrossRef](#)]
13. Davis, K.M.; Sullivan, B.T.; Palenik, M.C.; Yan, L.; Purohit, V.; Robison, G.; Kosheleva, I.; Henning, R.W.; Seidler, G.T.; Pushkar, Y. Rapid evolution of the photosystem II electronic structure during water splitting. *Phys. Rev. X* **2018**, *8*, 041014. [[CrossRef](#)]
14. Simon, P.S.; Makita, H.; Bogacz, I.; Fuller, F.; Bhowmick, A.; Hussein, R.; Ibrahim, M.; Zhang, M.; Chatterjee, R.; Cheah, M.H.; et al. Capturing the sequence of events during the water oxidation reaction in photosynthesis using XFELs. *FEBS Lett.* **2023**, *597*, 30–37. [[CrossRef](#)] [[PubMed](#)]
15. Bhowmick, A.; Hussein, R.; Bogacz, I.; Simon, R.S.; Ibrahim, M.; Chatterjee, R.; Doyle, M.D.; Cheah, M.H.; Fransson, T.; Chernev, P.; et al. Structural evidence for intermediates during O<sub>2</sub> formation in photosystem II. *Nature* **2023**, *617*, 629. [[CrossRef](#)]
16. Greife, P.; Schönborn, M.; Capone, M.; Assunção, R.; Narzi, D.; Guidoni, L.; Dau, H. The electron–proton bottleneck of photosynthetic oxygen evolution. *Nature* **2023**, *617*, 623. [[CrossRef](#)] [[PubMed](#)]
17. Tian, W.; Zhang, H.; Sibbons, J.; Sun, H.; Wang, H.; Wang, S. Photoelectrochemical water oxidation and longevous photoelectric conversion by a photosystem II electrode. *Adv. Energy Mater.* **2021**, *11*, 2100911. [[CrossRef](#)]
18. de Levie, R. The electrolysis of water. *J. Electroanal. Chem.* **1999**, *476*, 92. [[CrossRef](#)]
19. Fujishima, A.; Honda, K.; Kikuchi, S. Photosensitized electrolytic oxidation at TiO<sub>2</sub> semiconductor electrodes. *J. Chem. Soc. Jan.* **1969**, *72*, 108–113. (In Japanese) [[CrossRef](#)]
20. Longden, T.; Beck, F.J.; Jotzo, F.; Andrews, R.; Prasad, M. 'Clean' hydrogen?—Comparing the emissions and costs of fossil fuel versus renewable electricity based hydrogen. *Appl. Energy* **2022**, *306 Pt B*, 118145. [[CrossRef](#)]
21. ul Haq, T.; Haik, Y. A roadmap towards sustainable anode design for alkaline water electrolysis. *Appl. Catal. B Environ.* **2023**, *334*, 122853. [[CrossRef](#)]
22. An, L.; Wei, C.; Lu, M.; Liu, H.; Chen, Y.; Scherer, G.G.; Fisher, A.C.; Xi, P.; Xu, Z.J.; Yan, C.-H. Recent development of oxygen evolution electrocatalysts in acidic environment. *Adv. Mater.* **2021**, *33*, 2006328. [[CrossRef](#)] [[PubMed](#)]
23. Yu, M.; Budiayanto, E.; Tgysgz, H. Principles of water electrolysis and recent progress in cobalt-, nickel-, and iron-based oxides for the oxygen evolution reaction. *Angew. Chem. Int. Ed.* **2022**, *61*, e202103824. [[CrossRef](#)] [[PubMed](#)]
24. Ma, Q.; Mu, S. Acidic oxygen evolution reaction: Mechanism, catalyst classification, and enhancement strategies. *Interdiscip. Mater.* **2023**, *2*, 53–90. [[CrossRef](#)]
25. Vinodh, R.; Kalanur, S.S.; Natarajan, S.K.; Pollet, B.G. Recent advancements of polymeric membranes in anion exchange membrane water electrolyzer (AEMWE): A critical review. *Polymers* **2023**, *15*, 2144. [[CrossRef](#)]
26. Lin, Y.; Dong, Y.; Wang, X.; Chen, L. Electrocatalysts for the oxygen evolution reaction in acidic media. *Adv. Mater.* **2022**, *35*, 2210565. [[CrossRef](#)]
27. Jia, J.; Seitz, L.C.; Benck, J.D.; Huo, Y.; Chen, Y.; Wei, J.; Ng, D.; Bilir, T.; Harris, J.S.; Jaramillo, T.F. Solar water splitting by photovoltaic-electrolysis with a solar-to-hydrogen efficiency over 30%. *Nat. Commun.* **2016**, *7*, 13237. [[CrossRef](#)]

28. Khan, M.A.; Al-Shankiti, I.; Ziani, A.; Wehbe, N.; Idriss, H. A stable integrated photoelectrochemical reactor for H<sub>2</sub> production from water attains a solar-to-hydrogen efficiency of 18% at 15 suns and 13% at 207 suns. *Angew. Chem. Int. Ed.* **2020**, *59*, 14802–14808. [[CrossRef](#)]
29. Karuturi, S.K.; Shen, H.; Sharma, A.; Beck, F.J.; Varadhan, P.; Duong, T.; Narangari, P.R.; Zhang, D.; Wan, Y.; He, J.-H.; et al. Over 17% efficiency stand-alone solar water splitting enabled by perovskite-silicon tandem absorbers. *Adv. Energy Mater.* **2020**, *10*, 2000772. [[CrossRef](#)]
30. Holmes-Gentle, I.; Temburne, S.; Suter, C.; Haussener, S. Kilowatt-scale solar hydrogen production system using a concentrated integrated photoelectrochemical device. *Nat. Energy* **2023**, *8*, 586–596. [[CrossRef](#)]
31. Anantharaj, S.; Aravindan, V. Developments and perspectives in 3d transition-metal-based electrocatalysts for neutral and near-neutral water electrolysis. *Adv. Energy Mater.* **2020**, *10*, 1902666. [[CrossRef](#)]
32. Mayer, M.T. Photovoltage at semiconductor–electrolyte junctions. *Curr. Opinion Electrochem.* **2017**, *2*, 104–110. [[CrossRef](#)]
33. Fujishima, A.; Honda, K. Electrochemical photolysis of water at a semiconductor electrode. *Nature* **1972**, *238*, 37–38. [[CrossRef](#)]
34. Mesa, C.A.; Francàs, L.; Yang, K.R.; Garrido-Barros, P.; Pastor, E.; Ma, Y.; Kafizas, A.; Rosser, T.E.; Mayer, M.T.; Reisner, E.; et al. Multihole water oxidation catalysis on hematite photoanodes revealed by operando spectroelectrochemistry and DFT. *Nat. Chem.* **2020**, *12*, 82–89. [[CrossRef](#)] [[PubMed](#)]
35. Rajan, A.G.; Martinez, J.M.P.; Carter, E.A. Why do we use the materials and operating conditions we use for heterogeneous (photo)electrochemical water splitting? *ACS Catal.* **2020**, *10*, 11177–11234. [[CrossRef](#)]
36. Tang, R.; Zhou, S.; Zhang, Z.; Zheng, R.; Huang, J. Engineering nanostructure–interface of photoanode materials toward photoelectrochemical water oxidation. *Adv. Mater.* **2021**, *33*, 2005389. [[CrossRef](#)] [[PubMed](#)]
37. Cendula, P.; Bedoya-Lora, F.E.; Prabhakar, R.R. Semiconductor catalysts for oxygen and hydrogen evolution reactions. *ACS Appl. Energy Mater.* **2022**, *5*, 14593–14604. [[CrossRef](#)]
38. Ertem, M.Z.; Khariche, N.; Batista, V.S.; Hybertsen, M.S.; Tully, J.C.; Muckerman, J.T. Photoinduced water oxidation at the aqueous GaN (10 $\bar{1}0$ ) interface: Deprotonation kinetics of the first proton-coupled electron-transfer step. *ACS Catal.* **2015**, *5*, 2317–2323. [[CrossRef](#)]
39. Higashi, T.; Nishiyama, H.; Suzuki, Y.; Sasaki, Y.; Hisatomi, T.; Katayama, M.; Minegishi, T.; Seki, K.; Yamada, T.; Domen, K. Transparent Ta<sub>3</sub>N<sub>5</sub> photoanodes for efficient oxygen evolution toward the development of tandem cells. *Angew. Chem. Int. Ed.* **2019**, *58*, 2300–2304. [[CrossRef](#)]
40. Pihosh, Y.; Minegishi, T.; Nandal, V.; Higashi, T.; Katayama, M.; Yamada, T.; Sasaki, Y.; Seki, K.; Suzuki, Y.; Nakabayashi, M.; et al. Ta<sub>3</sub>N<sub>5</sub>-nanorods enabling highly efficient water oxidation via advantageous light harvesting and charge collection. *Energy Environ. Sci.* **2020**, *13*, 1519–1530. [[CrossRef](#)]
41. Ma, Z.; Piętak, K.; Piętak, J.; DeMoulipe, J.R.; Rokicińska, A.; Kuśtrowski, P.; Dronskowski, R.; Zlotnik, S.; Coridan, R.H.; Slabon, A. Semi-transparent quaternary oxynitride photoanodes on GaN underlayers. *Chem. Commun.* **2020**, *56*, 13193–13196. [[CrossRef](#)]
42. Huang, D.; Wang, K.; Li, L.; Feng, K.; An, N.; Ikeda, S.; Kuang, Y.; Ng, Y.; Jiang, F. 3.17% efficient Cu<sub>2</sub>ZnSnS<sub>4</sub>–BiVO<sub>4</sub> integrated tandem cell for standalone overall solar water splitting. *Energy Environ. Sci.* **2021**, *14*, 1480–1489. [[CrossRef](#)]
43. Pan, Z.; Chen, S.; Katayama, K. Roles of surface states in cocatalyst-loaded hematite photoanodes for water oxidation. *J. Phys. Chem. C* **2023**, *127*, 3904–3909. [[CrossRef](#)]
44. Jeon, T.H.; Han, S.; Kim, B.; Park, C.; Kim, W.; Park, H.; Choi, W. High-valent iron redox-mediated photoelectrochemical water oxidation. *ACS Energy Lett.* **2022**, *7*, 59–66. [[CrossRef](#)]
45. Morikawa, T.; Sato, S.; Sekizawa, K.; Suzuki, T.M.; Arai, T. Solar-driven CO<sub>2</sub> reduction using a semiconductor/molecule hybrid photosystem: From photocatalysts to a monolithic artificial leaf. *Acc. Chem. Res.* **2022**, *55*, 933–943. [[CrossRef](#)] [[PubMed](#)]
46. Andrei, V.; Jagt, R.A.; Rahaman; Lari, M.L.; Lazarov, V.K.; MacManus-Driscoll, J.L.; Hoye, R.L.Z.; Reisner, E. Long-term solar water and CO<sub>2</sub> splitting with photoelectrochemical BiOI–BiVO<sub>4</sub> tandems. *Nat. Mater.* **2022**, *21*, 864–868. [[CrossRef](#)] [[PubMed](#)]
47. Takanabe, K. Photocatalytic water splitting: Quantitative approaches toward photocatalyst by design. *ACS Catal.* **2017**, *7*, 8006–8022. [[CrossRef](#)]
48. Nosaka, Y.; Nosaka, A.Y. Intrinsic nature of photocatalysis by comparing with electrochemistry. *Phys. Chem. Chem. Phys.* **2020**, *22*, 7146–7154. [[CrossRef](#)]
49. Wang, Q.; Domen, K. Particulate photocatalysts for light-driven water splitting: Mechanisms, challenges, and design strategies. *Chem. Rev.* **2020**, *120*, 919–985. [[CrossRef](#)]
50. Tao, X.; Zhao, Y.; Wang, S.; Li, C.; Li, R. Recent advances and perspectives for solar-driven water splitting using particulate photocatalysts. *Chem. Soc. Rev.* **2022**, *51*, 3561–3608. [[CrossRef](#)] [[PubMed](#)]
51. Nishiyama, H.; Yamada, T.; Nakabayashi, M.; Maehara, Y.; Yamaguchi, M.; Kuromiya, Y.; Nagatsuma, Y.; Tokudome, H.; Akiyama, S.; Watanabe, T.; et al. Photocatalytic solar hydrogen production from water on a 100-m<sup>2</sup> scale. *Nature* **2021**, *598*, 304–307. [[CrossRef](#)]
52. Zhang, B.; Liu, K.; Xiang, Y.; Wang, J.; Lin, W.; Guo, M.; Ma, G. Facet-oriented assembly of Mo:BiVO<sub>4</sub> and Rh:SrTiO<sub>3</sub> particles: Integration of p–n conjugated photo-electrochemical system in a particle applied to photocatalytic overall water splitting. *ACS Catal.* **2022**, *12*, 2415–2425. [[CrossRef](#)]
53. Zhou, P.; Navid, I.A.; Ma, Y.; Xiao, Y.; Wang, P.; Ye, Z.; Zhou, B.; Sun, K.; Mi, Z. Solar-to-hydrogen efficiency of more than 9% in photocatalytic water splitting. *Nature* **2023**, *613*, 66–70. [[CrossRef](#)] [[PubMed](#)]

54. Yang, X.; Wang, Y.; Li, C.M.; Wang, D. Mechanisms of water oxidation on heterogeneous catalyst surfaces. *Nano Res.* **2021**, *14*, 3446–3457. [[CrossRef](#)]
55. Zhao, Y.; Saseendran, D.P.A.; Huang, C.; Triana, C.A.; Marks, W.R.; Chen, H.; Zhao, H.; Patzke, G.R. Oxygen evolution/reduction reaction catalysts: From in situ monitoring and reaction mechanisms to rational design. *Chem. Rev.* **2023**, *123*, 6257–6358. [[CrossRef](#)]
56. Shinagawa, T.; Garcia-Esparza, A.T.; Takanebe, K. Insight on Tafel slopes from a microkinetic analysis of aqueous electrocatalysis for energy conversion. *Sci. Rep.* **2015**, *5*, 13801. [[CrossRef](#)] [[PubMed](#)]
57. Zhang, J.; Tao, H.B.; Kuang, M.; Yang, H.B.; Cai, W.; Yan, Q.; Mao, Q.; Liu, B. Advances in thermodynamic-kinetic model for analyzing the oxygen evolution reaction. *ACS Catal.* **2020**, *10*, 8597–8610. [[CrossRef](#)]
58. Corby, S.; Rao, R.R.; Steier, L.; Durrant, J.R. The kinetics of metal oxide photoanodes from charge generation to catalysis. *Nat. Rev. Mater.* **2021**, *6*, 1136–1155. [[CrossRef](#)]
59. Francàs, F.; Corby, S.; Selim, S.; Lee, D.; Mesa, C.A.; Godin, R.; Pastor, E.; Stephens, I.E.L.; Choi, K.-S.; Durrant, J.R. Spectroelectrochemical study of water oxidation on nickel and iron oxyhydroxide electrocatalysts. *Nat. Commun.* **2019**, *10*, 5208. [[CrossRef](#)]
60. Francàs, L.; Selim, S.; Corby, S.; Lee, D.; Mesa, C.A.; Pastor, E.; Choi, K.-S.; Durrant, J.R. Water oxidation kinetics of nanoporous BiVO<sub>4</sub> photoanodes functionalised with nickel/iron oxyhydroxide electrocatalysts. *Chem. Sci.* **2021**, *12*, 7442. [[CrossRef](#)]
61. Zahran, Z.N.; Mohamed, E.A.; Naruta, Y. Kinetic and mechanism of heterogeneous water oxidation by  $\alpha$ -Mn<sub>2</sub>O<sub>3</sub> sintered on FTO electrode. *ACS Catal.* **2016**, *6*, 4470–4476. [[CrossRef](#)]
62. Xu, Z.; Liang, Z.; Guo, W.; Zou, R. In situ/operando vibrational spectroscopy for the investigation of advanced nanostructured electrocatalysts. *Coord. Chem. Rev.* **2021**, *436*, 213824. [[CrossRef](#)]
63. Li, N.; Cai, L.; Gao, G.; Lin, Y.; Wang, C.; Liu, H.; Liu, Y.; Duan, H.; Ji, Q.; Hu, W.; et al. Operando direct observation of stable water-oxidation intermediates on Ca<sub>2-x</sub>IrO<sub>4</sub> nanocrystals for efficient acidic oxygen evolution. *Nano Lett.* **2022**, *22*, 6988–6996. [[CrossRef](#)] [[PubMed](#)]
64. Zhang, M.; de Respinis, M.; Frei, H. Time-resolved observations of water oxidation intermediates on a cobalt oxide nanoparticle catalyst. *Nat. Chem.* **2014**, *6*, 362–367. [[CrossRef](#)] [[PubMed](#)]
65. Su, H.; Zhou, W.; Zhang, H.; Zhou, W.; Zhao, X.; Li, Y.; Liu, M.; Cheng, W.; Liu, Q. Dynamic evolution of solid-liquid electrochemical interfaces over single-atom active sites. *J. Am. Chem. Soc.* **2020**, *142*, 12306–12313. [[CrossRef](#)]
66. Sun, X.; Zhang, X.; Li, Y.; Xu, Y.; Su, H.; Che, W.; He, J.; Zhang, H.; Liu, M.; Zhou, W.; et al. In situ construction of flexible V-Ni redox centers over Ni-based MOF nanosheet arrays for electrochemical water oxidation. *Small Methods* **2021**, *5*, 2100573. [[CrossRef](#)]
67. Chu, H.-A.; Hillier, W.; Law, N.A.; Babcock, G.T. Vibrational spectroscopy of the oxygen-evolving complex and of manganese model compounds. *Biochim. Biophys. Acta* **2001**, *1503*, 69–82. [[CrossRef](#)]
68. Zhang, B.; Daniel, Q.; Fan, L.; Liu, T.; Meng, Q.; Sun, L. Identifying Mn<sup>VII</sup>-oxo species during electrochemical water oxidation by manganese oxide. *iScience* **2018**, *4*, 144–152. [[CrossRef](#)]
69. Zandi, O.; Hamann, T. Determination of photoelectrochemical water oxidation intermediates on haematite electrode surfaces using operando infrared spectroscopy. *Nat. Chem.* **2016**, *8*, 778–783. [[CrossRef](#)]
70. Herlihy, D.; Waegle, M.; Chen, X.; Pemmaraju, C.D.; Prendergast, D.; Cuk, T. Detecting the oxyl radical of photocatalytic water oxidation at an n-SrTiO<sub>3</sub>/aqueous interface through its subsurface vibration. *Nat. Chem.* **2016**, *8*, 549–555. [[CrossRef](#)]
71. Su, H.; Zhou, W.; Zhou, W.; Li, Y.; Zheng, L.; Zhang, H.; Liu, M.; Zhang, X.; Sun, X.; Xu, Y.; et al. In-situ spectroscopic observation of dynamic coupling oxygen on atomically dispersed iridium electrocatalyst for acidic water oxidation. *Nat. Commun.* **2021**, *12*, 6118. [[CrossRef](#)] [[PubMed](#)]
72. Li, X.; Zhang, X.-P.; Guo, M.; Lv, B.; Guo, K.; Jin, X.; Zhang, W.; Lee, Y.-M.; Fukuzum, S.; Nam, W.; et al. Identifying intermediates in electrocatalytic water oxidation with a manganese corrole complex. *J. Am. Chem. Soc.* **2021**, *143*, 14613–14621. [[CrossRef](#)] [[PubMed](#)]
73. Vivek, J.P.; Berry, N.G.; Zou, J.; Nichols, R.J.; Hardwick, L.J. In situ surface-enhanced infrared spectroscopy to identify oxygen reduction products in nonaqueous metal-oxygen batteries. *J. Phys. Chem. C* **2017**, *121*, 19657–19667. [[CrossRef](#)]
74. Lin, W.; Frei, H. Photochemical and FT-IR probing of the active site of hydrogen peroxide in Ti silicalite sieve. *J. Am. Chem. Soc.* **2002**, *124*, 9292–9298. [[CrossRef](#)]
75. Nakamura, R.; Imanishi, A.; Murakoshi, K.; Nakato, Y. In situ FTIR studies of primary intermediates of photocatalytic reactions on nanocrystalline TiO<sub>2</sub> films in contact with aqueous solutions. *J. Am. Chem. Soc.* **2003**, *125*, 7443–7450. [[CrossRef](#)]
76. Zhou, Z.; Kong, Y.; Tan, H.; Huang, Q.; Wang, C.; Pei, Z.; Wang, H.; Liu, Y.; Wang, Y.; Li, S.; et al. Cation-vacancy-enriched nickel phosphide for efficient electrosynthesis of hydrogen peroxides. *Adv. Mater.* **2022**, *34*, 2106541. [[CrossRef](#)]
77. Cheng, W.; Zhao, X.; Su, H.; Tang, F.; Che, W.; Zhang, H.; Liu, Q. Lattice-strained metal-organic-framework arrays for bifunctional oxygen electrocatalysis. *Nat. Energy* **2019**, *4*, 115–122. [[CrossRef](#)]
78. Lee, S.; Banjac, K.; Lingenfelder, M.; Hu, X. Oxygen isotope labeling experiments reveal different reaction sites for the oxygen evolution reaction on nickel and nickel iron oxides. *Angew. Chem. Int. Ed.* **2019**, *58*, 10295–10299. [[CrossRef](#)]
79. Chattopadhyay, S.; Ghatak, A.; Ro, Y.; Guillot, R.; Halime, Z.; Aukauloo, A.; Dey, A. Ligand radical mediated water oxidation by a family of copper o-phenylene bis-oxamidate complexes. *Inorg. Chem.* **2021**, *60*, 9442–9455. [[CrossRef](#)]

80. Lin, C.; Li, J.; Li, X.; Yang, S.; Luo, W.; Zhang, Y.; Kim, S.-H.; Kim, D.-H.; Shinde, S.S.; Li, Y.-F.; et al. In-situ reconstructed Ru atom array on  $\alpha$ -MnO with enhanced performance for acidic water oxidation. *Nat Catal.* **2021**, *4*, 1012–1023. [[CrossRef](#)]
81. Chen, T.; Ding, Q.; Wang, X.; Feng, Z.; Li, C. Mechanistic studies on photocatalytic overall water splitting over Ga<sub>2</sub>O<sub>3</sub>-based photocatalysts by *operando* MS-FTIR spectroscopy. *J. Phys. Chem. Lett.* **2021**, *12*, 6029–6033. [[CrossRef](#)]
82. Sivasankar, N.; Weare, W.W.; Frei, H. Direct observation of a hydroperoxide surface intermediate upon visible light-driven water oxidation at an Ir oxide nanocluster catalyst by rapid-scan FT-IR spectroscopy. *J. Am. Chem. Soc.* **2011**, *133*, 12976–12979. [[CrossRef](#)] [[PubMed](#)]
83. Liu, Y.; Chen, Y.; Mu, X.; Wu, Z.; Jin, X.; Li, J.; Xu, Y.; Yang, L.; Xi, X.; Jang, H.; et al. Spinel-anchored iridium single atoms enable efficient acidic water oxidation via intermediate stabilization effect. *ACS Catal.* **2023**, *13*, 3757–3767. [[CrossRef](#)]
84. Shao, M.H.; Adzic, R.R. Spectroscopic identification of the reaction intermediates in oxygen reduction on gold in alkaline solutions. *J. Phys. Chem. B* **2005**, *109*, 16563–16566. [[CrossRef](#)]
85. Liu, H.; Frei, H. Observation of O–O bond forming step of molecular Co<sub>4</sub>O<sub>4</sub> cubane catalyst for water oxidation by rapid-scan FT-IR spectroscopy. *ACS Catal.* **2020**, *10*, 2138–2147. [[CrossRef](#)]
86. Hunter, B.M.; Thompson, N.B.; Müller, A.M.; Rossman, G.R.; Hill, M.G.; Winkler, J.R.; Gray, H.B. Trapping an iron(VI) water-splitting intermediate in nonaqueous media. *Joule* **2018**, *2*, 747–763. [[CrossRef](#)]
87. Zhang, Y.; Zhang, H.; Liu, A.; Chen, C.; Song, W.; Zhao, J. Rate-limiting O–O bond formation pathways for water oxidation on hematite photoanode. *J. Am. Chem. Soc.* **2018**, *140*, 3264–3269. [[CrossRef](#)]
88. Shao, M.-H.; Liu, P.; Adzic, R.R. Superoxide anion is the intermediate in the oxygen reduction reaction on platinum electrodes. *J. Am. Chem. Soc.* **2006**, *128*, 7408–7409. [[CrossRef](#)]
89. Li, W.; Fu, H.; Cao, Y.; Wang, H.; Hao Yu, H.; Qiao, Z.; Liang, H.; Peng, F. Mn<sub>3</sub>O<sub>4</sub>@C nanoparticles supported on porous carbon as bifunctional oxygen electrodes and their electrocatalytic mechanism. *ChemElectroChem* **2019**, *6*, 359–368. [[CrossRef](#)]
90. Hess, C. New advances in using Raman spectroscopy for the characterization of catalysts and catalytic reactions. *Chem. Soc. Rev.* **2021**, *50*, 3519–3564. [[CrossRef](#)]
91. Huang, J.; Sheng, H.; Ross, R.D.; Han, J.; Wang, X.; Song, B.; Jin, S. Modifying redox properties and local bonding of Co<sub>3</sub>O<sub>4</sub> by CeO<sub>2</sub> enhances oxygen evolution catalysis in acid. *Nat. Commun.* **2021**, *12*, 3036. [[CrossRef](#)]
92. Moysiadou, A.; Lee, S.; Hsu, C.-S.; Chen, H.M.; Hu, X. Mechanism of oxygen evolution catalyzed by cobalt oxyhydroxide: Cobalt superoxide species as a key intermediate and dioxygen release as a rate-determining step. *J. Am. Chem. Soc.* **2020**, *142*, 11901–11914. [[CrossRef](#)] [[PubMed](#)]
93. Hu, C.; Hu, Y.; Fan, C.; Yang, L.; Zhang, Y.; Li, H.; Xie, W. Surface-enhanced Raman spectroscopic evidence of key intermediate species and role of NiFe dual-catalytic center in water oxidation. *Angew. Chem. Int. Ed.* **2021**, *60*, 19774–19778. [[CrossRef](#)] [[PubMed](#)]
94. Brückner, A. In situ electron paramagnetic resonance: A unique tool for analyzing structure–reactivity relationships in heterogeneous catalysis. *Chem. Soc. Rev.* **2010**, *39*, 4673–4684. [[CrossRef](#)] [[PubMed](#)]
95. Brückner, A. In situ EPR spectroscopy in heterogeneous catalysis: Stepchild or ray of hope? *Chem. Ingenieur Technik* **2014**, *86*, 1871–1882. [[CrossRef](#)]
96. Chiesa, M.; Giamello, E. On the role and applications of electron magnetic resonance techniques in surface chemistry and heterogeneous catalysis. *Catal. Lett.* **2021**, *151*, 3417–3436. [[CrossRef](#)]
97. Balaghi, S.E.; Mehrabani, S.; Mousazade, Y.; Bagheri, R.; Sologubenko, A.S.; Song, Z.; Patzke, G.R.; Najafpour, M.M. Mechanistic understanding of water oxidation in the presence of a copper complex by in situ electrochemical liquid transmission electron microscopy. *ACS Appl. Mater. Interfaces* **2021**, *13*, 19927–19937. [[CrossRef](#)]
98. Peña, N.O.; Ihiwakrim, D.; Han, M.; Lassalle-Kaiser, B.; Carenco, S.; Sanchez, C.; Laberty-Robert, C.; Portehault, D.; Ersen, O. Morphological and structural evolution of Co<sub>3</sub>O<sub>4</sub> nanoparticles revealed by in situ electrochemical transmission electron microscopy during electrocatalytic water oxidation. *ACS Nano* **2019**, *13*, 11372–11381. [[CrossRef](#)]
99. Zhao, G.; Yao, Y.; Lu, W.; Liu, G.; Guo, X.; Tricoli, A.; Zhu, Y. Direct observation of oxygen evolution and surface restructuring on Mn<sub>2</sub>O<sub>3</sub> nano catalysts using in situ and ex situ transmission electron microscopy. *Nano Lett.* **2021**, *21*, 7012–7020. [[CrossRef](#)]
100. Mom, R.; Frevel, L.; Velasco-Vélez, J.-J.; Plodinec, M.; Knop-Gericke, A.; Schlögl, R. The oxidation of platinum under wet conditions observed by electrochemical X-ray photoelectron spectroscopy. *J. Am. Chem. Soc.* **2019**, *141*, 6537–6544. [[CrossRef](#)]
101. van Oversteeg, C.H.M.; Doan, H.Q.; de Groot, F.M.F.; Cuk, T. In situ X-ray absorption spectroscopy of transition metal based water oxidation catalysts. *Chem. Soc. Rev.* **2017**, *46*, 102–125. [[CrossRef](#)]
102. Beaumont, S.K. Soft XAS as an in situ technique for the study of heterogeneous catalysts. *Phys. Chem. Chem. Phys.* **2020**, *22*, 18747–18756. [[CrossRef](#)] [[PubMed](#)]
103. Cutsail III, G.E.; DeBeer, S. Challenges and opportunities for applications of advanced X-ray spectroscopy in catalysis research. *ACS Catal.* **2022**, *12*, 5864–5886. [[CrossRef](#)]
104. Park, J.; Cho, J. Advances in understanding mechanisms of perovskites and pyrochlores as electrocatalysts using in-situ X-ray absorption spectroscopy. *Angew. Chem. Int. Ed.* **2020**, *59*, 15314–15324. [[CrossRef](#)]
105. Chang, C.-J.; Zhu, Y.; Wang, J.; Chen, H.-C.; Tung, C.-W.; Chu, Y.-C.; Chen, H.M. In situ X-ray diffraction and X-ray absorption spectroscopy of electrocatalysts for energy conversion reactions. *J. Mater. Chem. A* **2020**, *8*, 19079–19112. [[CrossRef](#)]
106. Zeng, Y.; Li, X.; Wang, J.; Sougrati, M.T.; Huang, Y.; Zhang, T.; Liu, B. In situ/operando Mössbauer spectroscopy for probing heterogeneous catalysis. *Chem Catal.* **2021**, *1*, 1215–1233. [[CrossRef](#)]

107. Scherthan, L.; Schmidt, S.F.M.; Auerbach, H.; Hochdörffer, T.; Wolny, J.A.; Bi, W.; Zhao, J.; Hu, M.Y.; Toellner, T.; Alp, E.E.; et al.  $^{161}\text{Dy}$  time-domain synchrotron Mössbauer spectroscopy for investigating single-molecule magnets incorporating Dy ions. *Angew. Chem. Int. Ed.* **2019**, *58*, 3444–3449. [[CrossRef](#)]
108. Kunze, S.; Grosse, P.; Lopez, M.B.; Sinev, I.; Zegkinoglou, I.; Mistry, H.; Timoshenko, J.; Hu, M.Y.; Zhao, J.; Alp, E.E.; et al. Operando NRIXS and XAFS investigation of segregation phenomena in Fe-Cu and Fe-Ag nanoparticle catalysts during  $\text{CO}_2$  electroreduction. *Angew. Chem. Int. Ed.* **2020**, *59*, 22667–22674. [[CrossRef](#)]
109. Craig, M.J.; Coulter, G.; Dolan, E.; Soriano-López, J.; Mates-Torres, E.; Schmitt, W.; García-Melchor, M. Universal scaling relations for the rational design of molecular water oxidation catalysts with near-zero overpotential. *Nat. Commun.* **2019**, *10*, 4993. [[CrossRef](#)]
110. Siahrostami, S.; Li, G.-L.; Viswanathan, V.; Nørskov, J.K. One- or two-electron water oxidation, hydroxyl radical, or  $\text{H}_2\text{O}_2$  evolution. *J. Phys. Chem. Lett.* **2017**, *8*, 1157–1160. [[CrossRef](#)]
111. Man, I.C.; Su, H.-Y.; Calle-Vallejo, F.; Hansen, H.A.; Martínez, J.I.; Inoglu, N.G.; Kitchin, J.; Jaramillo, T.F.; Nørskov, J.K.; Rossmeisl, J. Universality in oxygen evolution electrocatalysis on oxide surfaces. *ChemCatChem* **2011**, *3*, 1159–1165. [[CrossRef](#)]
112. Zhang, N.; Chai, Y. Lattice oxygen redox chemistry in solid-state electrocatalysts for water oxidation. *Energy Environ. Sci.* **2021**, *14*, 4647–4671. [[CrossRef](#)]
113. Nosaka, Y. Water photo-oxidation over  $\text{TiO}_2$ —History and reaction mechanism. *Catalysts* **2022**, *12*, 1557. [[CrossRef](#)]
114. Wang, D.; Sheng, T.; Chen, J.; Wang, H.-F.; Hu, P. Identifying the key obstacle in photocatalytic oxygen evolution on rutile  $\text{TiO}_2$ . *Nat. Catal.* **2018**, *1*, 291–299. [[CrossRef](#)]
115. Li, B.; Wu, S.; Gao, X. Theoretical calculation of a  $\text{TiO}_2$ -based photocatalyst in the field of water splitting: A review. *Nanotechnol. Rev.* **2020**, *9*, 85. [[CrossRef](#)]
116. Malik, A.S.; Fredin, L.A. Unraveling the water oxidation mechanism on a stoichiometric and reduced rutile  $\text{TiO}_2(100)$  surface using first-principles calculations. *J. Phys. Chem. C* **2023**, *127*, 3444–3451. [[CrossRef](#)]
117. Kakuma, Y.; Nosaka, A.Y.; Nosaka, Y. Difference of  $\text{TiO}_2$  photocatalytic mechanism between rutile and anatase studied by the detection of active oxygen and surface species in water. *Phys. Chem. Chem. Phys.* **2015**, *17*, 18691–18698. [[CrossRef](#)]
118. Li, F.; Chen, J.-F.; Gong, X.-Q.; Hu, P.; Wang, D. Subtle structure matters: The vicinity of surface  $\text{Ti}_{5\text{C}}$  cations alters the photooxidation behaviors of anatase and rutile  $\text{TiO}_2$  under aqueous environments. *ACS Catal.* **2022**, *12*, 8242–8251. [[CrossRef](#)]
119. Nakamura, R.; Nakato, Y. Primary intermediates of oxygen photoevolution reaction on  $\text{TiO}_2$  (rutile) particles, revealed by in situ FTIR absorption and photoluminescence measurements. *J. Am. Chem. Soc.* **2004**, *126*, 1290–1298. [[CrossRef](#)]
120. Nakamura, R.; Okamura, T.; Ohashi, N.; Imanishi, A.; Nakato, Y. Molecular mechanisms of photoinduced oxygen evolution, PL emission, and surface roughening at atomically smooth (110) and (100) n- $\text{TiO}_2$  (rutile) surfaces in aqueous acidic solutions. *J. Am. Chem. Soc.* **2005**, *127*, 12975–12983. [[CrossRef](#)]
121. Zhuang, Y.-B.; Cheng, J. Deciphering the anomalous acidic tendency of terminal water at rutile(110)–water interfaces. *J. Phys. Chem. C* **2023**, *127*, 10532–10540. [[CrossRef](#)]
122. Kudo, A.; Miseki, Y. Heterogeneous photocatalyst materials for water splitting. *Chem. Soc. Rev.* **2009**, *38*, 253–278. [[CrossRef](#)]
123. Wang, Q.; Hisatomi, T.; Jia, Q.; Tokudome, H.; Zhong, M.; Wang, C.; Pan, Z.; Takata, T.; Nakabayashi, M.; Shibata, N.; et al. Scalable water splitting on particulate photocatalyst sheets with a solar-to-hydrogen energy conversion efficiency exceeding 1. *Nat. Mater.* **2016**, *15*, 611–615. [[CrossRef](#)] [[PubMed](#)]
124. Rafter, R.A.; Mehta, A.; Lu, Y.; Valant, M.; Fang, M.; Liu, W. Influence of exposed facets, morphology and hetero-interfaces of  $\text{BiVO}_4$  on photocatalytic water oxidation: A review. *Int. J. Hydrogen Energy* **2021**, *46*, 21866–21888. [[CrossRef](#)]
125. Ma, Y.; Pendlebury, S.R.; Reynal, A.; Formal, F.L.; Durrant, J.R. Dynamics of photogenerated holes in undoped  $\text{BiVO}_4$  photoanodes for solar water oxidation. *Chem. Sci.* **2014**, *5*, 2964–2973. [[CrossRef](#)]
126. Abdellaoui, I.; Islam, M.M.; Remeika, M.; Higuchi, Y.; Kawaguchi, T.; Harada, T.; Budich, C.; Maeda, T.; Wada, T.; Ikeda, S.; et al. Photocarrier recombination dynamics in  $\text{BiVO}_4$  for visible light-driven water oxidation. *J. Phys. Chem. C* **2020**, *124*, 3962–3972. [[CrossRef](#)]
127. Tran-Phu, T.; Fusco, Z.; Bernardo, I.D.; Lipton-Duffin, J.; Toe, C.Y.; Daiyan, R.; Gengenbach, T.; Lin, C.-H.; Bo, R.; Nguyen, H.T.; et al. Understanding the role of vanadium vacancies in  $\text{BiVO}_4$  for efficient photoelectrochemical water oxidation. *Chem. Mater.* **2021**, *33*, 3553–3565. [[CrossRef](#)]
128. Walsh, A.; Yan, Y.; Huda, M.N.; Al-Jassim, M.M.; Wei, S.-H. Band edge electronic structure of  $\text{BiVO}_4$ : Elucidating the role of the Bi s and V d orbitals. *Chem. Mater.* **2009**, *21*, 547–551. [[CrossRef](#)]
129. Hu, J.; Zhao, X.; Chen, W.; Su, H.; Chen, Z. Theoretical insight into the mechanism of photoelectrochemical oxygen evolution reaction on  $\text{BiVO}_4$  anode with oxygen vacancy. *J. Phys. Chem. C* **2017**, *121*, 18702–18709. [[CrossRef](#)]
130. Liu, G.; Li, F.; Zhu, Y.; Lia, J.L.; Sun, L. Cobalt doped  $\text{BiVO}_4$  with rich oxygen vacancies for efficient photoelectrochemical water oxidation. *RSC Adv.* **2020**, *10*, 28523–28526. [[CrossRef](#)]
131. Liu, T.; Liu, R.; Li, Q.; Yang, J. Theoretical insight into the role of defects and facets in the selectivity of products in water oxidation over bismuth vanadate ( $\text{BiVO}_4$ ). *ACS Sustain. Chem. Eng.* **2020**, *8*, 1980–1988. [[CrossRef](#)]
132. Wang, W.; Strohbeen, P.J.; Lee, D.; Zhou, C.; Kawasaki, J.K.; Choi, K.-S.; Liu, M.; Galli, G. The role of surface oxygen vacancies in  $\text{BiVO}_4$ . *Chem. Mater.* **2020**, *32*, 2899–2909. [[CrossRef](#)]
133. Steinitz-Eliyahu, R.; Hernangómez-Pérez, D.; Hegner, F.S.; Nikačević, P.; López, N.; Refaely-Abramson, S. Mixed excitonic nature in water-oxidized  $\text{BiVO}_4$  surfaces with defects. *Phys. Rev. Mater.* **2022**, *6*, 065402. [[CrossRef](#)]

134. Huang, M.; He, W.; Xu, Z.; Zhu, H. Enhanced catalytic mechanism of twin-structured BiVO<sub>4</sub>. *J. Phys. Chem. Lett.* **2021**, *12*, 10610–10615. [[CrossRef](#)] [[PubMed](#)]
135. Nikačević, P.; Hegner, F.S.; Galán-Mascarós, J.R.; López, N. Influence of oxygen vacancies and surface facets on water oxidation selectivity toward oxygen or hydrogen peroxide with BiVO<sub>4</sub>. *ACS Catal.* **2021**, *11*, 13416–13422. [[CrossRef](#)]
136. Park, H.S.; Leonard, K.C.; Bard, A.J. Surface interrogation scanning electrochemical microscopy (SISECM) of photoelectrochemistry at a W/Mo-BiVO<sub>4</sub> semiconductor electrode. *J. Phys. Chem. C* **2013**, *117*, 12093–12102. [[CrossRef](#)]
137. Nakabayashi, Y.; Nishikawa, M.; Saito, N.; Terashima, C.; Fujishima, A. Significance of hydroxyl radical in photoinduced oxygen evolution in water on monoclinic bismuth vanadate. *J. Phys. Chem. C* **2017**, *121*, 25624–25631. [[CrossRef](#)]
138. Nakabayashi, Y.; Suzuki, N.; Terashima, C.; Fujishima, A. In situ infrared analysis for the process of water photo-oxidation on monoclinic bismuth vanadate. *J. Phys. Chem. C* **2021**, *125*, 18579–18587. [[CrossRef](#)]
139. Sun, Q.; Ren, K.; Qi, L. Boosting the performance of BiVO<sub>4</sub> photoanodes by the simultaneous introduction of oxygen vacancies and cocatalyst via photoelectrodeposition. *ACS Appl. Mater. Interfaces* **2022**, *14*, 37833–37842. [[CrossRef](#)]
140. Pan, L.; Wu, J.; Xu, X.; Lv, F.; Chen, Y.; Guo, L. Photoelectrochemical performance of bismuth vanadate photoanode for water splitting under concentrated light irradiation. *Int. J. Hydrogen Energy* **2023**, *48*, 13479–13488. [[CrossRef](#)]
141. Majumder, S.; Su, X.; Kim, K.H. Effective strategy of incorporating Co<sub>3</sub>O<sub>4</sub> as a co-catalyst onto an innovative BiVO<sub>4</sub>/Fe<sub>2</sub>TiO<sub>5</sub> core-shell heterojunction for effective photoelectrochemical water-splitting application. *Surf. Interfaces* **2023**, *39*, 102936. [[CrossRef](#)]
142. Avcioglu, C.; Avcioglu, S.; Bekheet, M.F.; Gurlo, A. Photocatalytic overall water splitting by SrTiO<sub>3</sub>: Progress report and design strategies. *ACS Appl. Energy Mater.* **2023**, *6*, 1134–1154. [[CrossRef](#)]
143. Chen, X.; Choing, S.N.; Aschaffenburg, D.J.; Pemmaraju, C.D.; Prendergast, D.; Cuk, T. The formation time of Ti–O• and Ti–O•–Ti radicals at the n-SrTiO<sub>3</sub>/aqueous interface during photocatalytic water oxidation. *J. Am. Chem. Soc.* **2017**, *139*, 1830–1841. [[CrossRef](#)] [[PubMed](#)]
144. Chen, X.; Aschaffenburg, D.J.; Cuk, T. Selecting between two transition states by which water oxidation intermediates decay on an oxide surface. *Nat. Catal.* **2019**, *2*, 820–827. [[CrossRef](#)]
145. Vinogradov, I.; Singh, S.; Lyle, H.; Paolino, M.; Mandal, A.; Rossmeisl, J.; Cuk, T. Free energy difference to create the M–OH• intermediate of the oxygen evolution reaction by time-resolved optical spectroscopy. *Nat. Mater.* **2022**, *21*, 88–94. [[CrossRef](#)]
146. Lyle, H.; Singh, S.; Magnano, E.; Nappini, S.; Bondino, F.; Yazdi, S.; Cuk, T. Assessing and quantifying thermodynamically concomitant degradation during oxygen evolution from water on SrTiO<sub>3</sub>. *ACS Catal.* **2023**, *13*, 8206–8218. [[CrossRef](#)]
147. Zhou, X.; Hensen, E.J.M.; van Santen, R.A.; Li, C. DFT simulations of water adsorption and activation on low-index α-Ga<sub>2</sub>O<sub>3</sub> surfaces. *Chem. Eur. J.* **2014**, *20*, 6915–6926. [[CrossRef](#)]
148. Wang, Q.; Nakabayashi, M.; Hisatomi, T.; Sun, S.; Akiyama, S.; Wang, Z.; Pan, Z.; Xiao, X.; Watanabe, T.; Yamada, T.; et al. Oxy-sulfide photocatalyst for visible-light-driven overall water splitting. *Nat. Mater.* **2019**, *18*, 827–832. [[CrossRef](#)]
149. Yu, H.; Ge, J. Recent advances in Ru-based electrocatalysts toward acid electrochemical water oxidation. *Curr. Opinion Electrochem.* **2023**, *39*, 101296. [[CrossRef](#)]
150. Raman, A.S.; Vojvodic, A. Providing atomistic insights into the dissolution of rutile oxides in electrocatalytic water splitting. *J. Phys. Chem. C* **2022**, *126*, 922–932. [[CrossRef](#)]
151. Liu, S.; Chang, Y.; He, N.; Zhu, S.; Wang, L.; Liu, X. Competition between lattice oxygen and adsorbate evolving mechanisms in rutile Ru-based oxide for the oxygen evolution reaction. *ACS Appl. Mater. Interf.* **2023**, *15*, 20563–20570. [[CrossRef](#)]
152. Pavlovic, Z.; Ranjan, C.; Gao, Q.; van Gestel, M.; Schlögl, R. Probing the structure of a water-oxidizing anodic iridium oxide catalyst using Raman spectroscopy. *ACS Catal.* **2016**, *6*, 8098–8105. [[CrossRef](#)]
153. Ooka, H.; Yamaguchi, A.; Takashima, T.; Hashimoto, K.; Nakamura, R. Efficiency of oxygen evolution on iridium oxide determined from the pH dependence of charge accumulation. *J. Phys. Chem. C* **2017**, *121*, 17873–17881. [[CrossRef](#)]
154. Bozal-Ginesta, C.; Rao, R.R.; Mesa, C.A.; Liu, X.; Hillman, S.A.J.; Stephens, I.E.L.; Durrant, J.R. Redox-state kinetics in water-oxidation IrO<sub>x</sub> electrocatalysts measured by *operando* spectroelectrochemistry. *ACS Catal.* **2021**, *11*, 15013–15025. [[CrossRef](#)]
155. Czioska, S.; Boubnov, A.; Escalera-López, D.; Geppert, J.; Zagalskaya, A.; Röse, P.; Saraçi, E.; Alexandrov, V.; Krewer, U.; Cherevko, S.; et al. Increased Ir–Ir interaction in iridium oxide during the oxygen evolution reaction at high potentials probed by *operando* spectroscopy. *ACS Catal.* **2021**, *11*, 10043–10057. [[CrossRef](#)]
156. Ping, Y.; Nielsen, R.J.; Goddard III, W.A. The reaction mechanism with free energy barriers at constant potentials for the oxygen evolution reaction at the IrO<sub>2</sub>(110) surface. *J. Am. Chem. Soc.* **2017**, *139*, 149–155. [[CrossRef](#)]
157. Binniger, T.; Doublet, M.-L. The Ir–OOOO–Ir transition state and the mechanism of the oxygen evolution reaction on IrO<sub>2</sub>(110). *Energy Environ. Sci.* **2022**, *15*, 2519–2528. [[CrossRef](#)]
158. Liao, F.; Yin, K.; Ji, Y.; Zhu, W.; Fan, Z.; Li, Y.; Zhong, J.; Shao, M.; Kang, Z.; Shao, Q. Iridium oxide nanoribbons with metastable monoclinic phase for highly efficient electrocatalytic oxygen evolution. *Nat. Commun.* **2023**, *14*, 1248. [[CrossRef](#)]
159. Xie, Y.; Chang, C.; Luo, F.; Yang, Z. Modulation in the d band of Ir by core–shell construction for robust water splitting electrocatalysts in acid. *ACS Appl. Mater. Interfaces* **2023**, *15*, 20081–20088. [[CrossRef](#)]
160. Reksten, A.H.; Thuv, H.; Seland, F.; Sunde, S. The oxygen evolution reaction mechanism at Ir<sub>x</sub>Ru<sub>1–x</sub>O<sub>2</sub> powders produced by hydrolysis synthesis. *J. Electroanal. Chem.* **2018**, *819*, 547–561. [[CrossRef](#)]
161. Rao, R.R.; Kolb, M.J.; Halck, N.B.; Pedersen, A.F.; Mehta, A.; You, H.; Stoerzinger, K.A.; Feng, Z.; Hansen, H.A.; Zhou, H.; et al. Towards identifying the active sites on RuO<sub>2</sub>(110) in catalyzing oxygen evolution. *Energy Environ. Sci.* **2017**, *10*, 2626–2637. [[CrossRef](#)]

162. Liang, Q.; Bieberle-Hütter, A.; Brocks, G. Anti-ferromagnetic RuO<sub>2</sub>: A stable and robust OER catalyst over a large range of surface terminations. *J. Phys. Chem. C* **2022**, *126*, 1337–1345. [[CrossRef](#)]
163. Stoerzinger, K.A.; Diaz-Morales, O.; Kolb, M.; Rao, R.R.; Frydendal, R.; Qiao, L.; Wang, X.R.; Halck, N.B.; Rossmeisl, J.; Hansen, H.A.; et al. Orientation-dependent oxygen evolution on RuO<sub>2</sub> without lattice exchange. *ACS Energy Lett.* **2017**, *2*, 876–881. [[CrossRef](#)]
164. Wang, Y.; Yang, R.; Ding, Y.; Zhang, B.; Li, H.; Bai, B.; Li, M.; Cui, Y.; Xiao, J.; Wu, Z.-S. Unraveling oxygen vacancy site mechanism of Rh-doped RuO<sub>2</sub> catalyst for long-lasting acidic water oxidation. *Nat. Commun.* **2023**, *14*, 1412. [[CrossRef](#)]
165. Zagalskaya, A.; Alexandrov, V. Role of defects in the interplay between adsorbate evolving and lattice oxygen mechanisms of the oxygen evolution reaction in RuO<sub>2</sub> and IrO<sub>2</sub>. *ACS Catal.* **2020**, *10*, 3650–3657. [[CrossRef](#)]
166. Wang, X.; Wan, X.; Qin, X.; Chen, C.; Qian, X.; Guo, Y.; Xu, Q.; Cai, W.-B.; Yang, H.; Jiang, K. Electronic structure modulation of RuO<sub>2</sub> by TiO<sub>2</sub> enriched with oxygen vacancies to boost acidic O<sub>2</sub> evolution. *ACS Catal.* **2022**, *12*, 9437–9445. [[CrossRef](#)]
167. Godínez-Salomón, J.F.; Ospina-Acevedo, F.; Albiter, L.A.; Bailey, K.O.; Naymik, Z.G.; Mendoza-Cruz, R.; Balbuena, P.B.; Rhodes, C.P. Titanium substitution effects on the structure, activity, and stability of nanoscale ruthenium oxide oxygen evolution electrocatalysts: Experimental and computational study. *ACS Appl. Nano Mater.* **2022**, *5*, 11752–11775. [[CrossRef](#)]
168. Shi, Z.; Li, J.; Wang, Y.; Liu, S.; Zhu, J.; Yang, J.; Wang, X.; Ni, J.; Jiang, Z.; Zhang, L.; et al. Customized reaction route for ruthenium oxide towards stabilized water oxidation in high-performance PEM electrolyzers. *Nat. Commun.* **2023**, *14*, 843. [[CrossRef](#)]
169. Xue, Y.; Fang, J.; Wang, X.; Xu, Z.; Zhang, Y.; Lv, Q.; Liu, M.; Zhu, W.; Zhuang, Z. Sulfate-functionalized RuFeO<sub>x</sub> as highly efficient oxygen evolution reaction electrocatalyst in acid. *Adv. Funct. Mater.* **2021**, *31*, 2101405. [[CrossRef](#)]
170. Shang, C.; Xiao, X.; Xu, Q. Coordination chemistry in modulating electronic structures of perovskite-type oxide nanocrystals for oxygen evolution catalysis. *Coord. Chem. Rev.* **2023**, *485*, 215109. [[CrossRef](#)]
171. Hong, W.T.; Stoerzinger, K.A.; Lee, Y.-L.; Giordano, L.; Grimaud, A.; Johnson, A.M.; Hwang, J.; Crumlin, E.J.; Yange, W.; Shao-Horn, Y. Charge-transfer-energy-dependent oxygen evolution reaction mechanisms for perovskite oxides. *Energy Environ. Sci.* **2017**, *10*, 2190–2200. [[CrossRef](#)]
172. Shi, Z.; Wang, X.; Ge, J.; Liu, C.; Xing, W. Fundamental understanding of the acidic oxygen evolution reaction: Mechanism study and state-of-the-art catalysts. *Nanoscale* **2020**, *12*, 13249–13275. [[CrossRef](#)] [[PubMed](#)]
173. Lu, M.; Zheng, Y.; Hu, Y.; Huang, B.; Ji, D.; Sun, M.; Li, J.; Peng, Y.; Si, R.; Xi, P.; et al. Artificially steering electrocatalytic oxygen evolution reaction mechanism by regulating oxygen defect contents in perovskites. *Sci. Adv.* **2022**, *8*, eabq3563. [[CrossRef](#)] [[PubMed](#)]
174. Peng, M.; Huang, J.; Zhu, Y.; Zhou, H.; Hu, Z.; Liao, Y.-K.; Lai, Y.-H.; Chen, C.-T.; Chu, Y.-H.; Zhang, K.H.L.; et al. Structural anisotropy determining the oxygen evolution mechanism of strongly correlated perovskite nickelate electrocatalyst. *ACS Sustain. Chem. Eng.* **2021**, *9*, 4262–4270. [[CrossRef](#)]
175. Sun, Y.; Wu, C.-R.; Ding, T.-Y.; Gu, J.; Yan, J.-W.; Cheng, J.; Zhang, K.H.L. Direct observation of the dynamic reconstructed active phase of perovskite LaNiO<sub>3</sub> for the oxygen evolution reaction. *Chem. Sci.* **2023**, *14*, 5906–5911. [[CrossRef](#)]
176. Lee, S.; Kishore, M.R.A.; Kim, D.; Kang, H.; Chun, J.; Oh, L.S.; Park, J.H.; Kim, H.J.; Yoo, J.S.; Lim, E. Direct O–O coupling promoted the oxygen evolution reaction by dual active sites from Ag/LaNiO<sub>3</sub> interfaces. *ACS Appl. Energy Mater.* **2022**, *5*, 14658–14668. [[CrossRef](#)]
177. Chen, H.; Shi, L.; Sun, K.; Zhang, K.; Liu, Q.; Ge, J.; Liang, X.; Tian, B.; Huang, Y.; Shi, Z.; et al. Protonated iridate nanosheets with a highly active and stable layered perovskite framework for acidic oxygen evolution. *ACS Catal.* **2022**, *12*, 8658–8666. [[CrossRef](#)]
178. Han, J.; Guan, J. Multicomponent transition metal oxides and (oxy)hydroxides for oxygen evolution. *Nano Res.* **2023**, *16*, 1913–1966. [[CrossRef](#)]
179. Wang, H.; Zhang, K.H.L.; Hofmann, J.P.; O’Shea, V.A.; Oropeza, F.E. The electronic structure of transition metal oxides for oxygen evolution reaction. *J. Mater. Chem. A* **2021**, *9*, 19465–19488. [[CrossRef](#)]
180. Feng, Y.; Yang, H.; Wang, X.; Hu, C.; Jing, H.; Cheng, J. Role of transition metals in catalyst designs for oxygen evolution reaction: A comprehensive review. *Int. J. Hydrogen Energy* **2022**, *47*, 17946–17970. [[CrossRef](#)]
181. Guo, T.; Li, L.; Wang, Z. Recent development and future perspectives of amorphous transition metal-based electrocatalysts for oxygen evolution reaction. *Adv. Energy Mater.* **2022**, *12*, 2200827. [[CrossRef](#)]
182. Huang, C.-J.; Xu, H.-M.; Shuai, T.-Y.; Zhan, Q.-N.; Zhang, Z.-J.; Li, G.-R. A review of modulation strategies for improving catalytic performance of transition metal phosphides for oxygen evolution reaction. *App. Catal. B Environ.* **2023**, *325*, 122313. [[CrossRef](#)]
183. Zhang, W.; Cao, R. Switching the O–O bond formation mechanism by controlling water activity. *Chem* **2021**, *7*, 1981–1992. [[CrossRef](#)]
184. Takata, T.; Jiang, J.; Sakata, Y.; Nakabayashi, M.; Shibata, N.; Nandal, V.; Seki, K.; Hisatomi, T.; Domen, K. Photocatalytic water splitting with a quantum efficiency of almost unity. *Nature* **2020**, *581*, 411–414. [[CrossRef](#)] [[PubMed](#)]
185. Wang, C.; Deng, R.; Guo, M.; Zhang, Q. Recent progress of advanced Co<sub>3</sub>O<sub>4</sub>-based materials for electrocatalytic oxygen evolution reaction in acid: From rational screening to efficient design. *Int. J. Hydrogen Energy*, 2023; *in press*. [[CrossRef](#)]
186. Favaro, M.; Yang, J.; Nappini, S.; Magnano, E.; Toma, F.M.; Crumlin, E.J.; Yano, J.; Sharp, I.D. Understanding the oxygen evolution reaction mechanism on CoO<sub>x</sub> using *operando* ambient-pressure X-ray photoelectron spectroscopy. *J. Am. Chem. Soc.* **2017**, *139*, 8960–8970. [[CrossRef](#)] [[PubMed](#)]
187. Lang, C.; Li, J.; Yang, K.R.; Wang, Y.; He, D.; Thorne, J.E.; Croslow, S.; Dong, Q.; Zhao, Y.; Prostko, G.; et al. Observation of a potential-dependent switch of water-oxidation mechanism on Co-oxide-based catalysts. *Chem* **2021**, *7*, 2101–2117. [[CrossRef](#)]

188. Wang, S.; Jiang, Q.; Ju, S.; Hsu, C.-S.; Chen, H.M.; Zhang, D.; Song, F. Identifying the geometric catalytic active sites of crystalline cobalt oxyhydroxides for oxygen evolution reaction. *Nat. Commun.* **2022**, *13*, 6650. [[CrossRef](#)]
189. Kang, W.; Wei, R.; Yin, H.; Li, D.; Chen, Z.; Huang, Q.; Zhang, P.; Jing, H.; Wang, X.; Li, C. Unraveling sequential oxidation kinetics and determining roles of multi-cobalt active sites on  $\text{Co}_3\text{O}_4$  catalyst for water oxidation. *J. Am. Chem. Soc.* **2023**, *145*, 3470–3477. [[CrossRef](#)]
190. Lin, Y.; Yu, L.; Tang, L.; Song, F.; Schlögl, R.; Heumann, S. In situ identification and time-resolved observation of the interfacial state and reactive intermediates on a cobalt oxide nanocatalyst for the oxygen evolution reaction. *ACS Catal.* **2022**, *12*, 5345–5355. [[CrossRef](#)]
191. Zhou, D.; Li, F.; Zhao, Y.; Wang, L.; Zou, H.; Shan, Y.; Fu, J.; Ding, Y.; Duan, L.; Liu, M.; et al. Mechanistic regulation by oxygen vacancies in structural evolution promoting electrocatalytic water oxidation. *ACS Catal.* **2023**, *13*, 4398–4408. [[CrossRef](#)]
192. Ren, X.; Ji, Y.; Zhai, Y.; Yuan, N.; Ding, J.; Li, Y.; Yan, J.; Liu, S.F. Self-assembled  $\text{CoOOH}$  on  $\text{TiO}_2$  for enhanced photoelectrochemical water oxidation. *J. Energy Chem.* **2021**, *60*, 512–521. [[CrossRef](#)]
193. Yao, N.; Wang, G.; Jia, H.; Yin, J.; Cong, H.; Chen, S.; Luo, W. Intermolecular energy gap-induced formation of high-valent cobalt species in  $\text{CoOOH}$  surface layer on cobalt sulfides for efficient water oxidation. *Angew. Chem. Int. Ed.* **2022**, *61*, e202117178. [[CrossRef](#)] [[PubMed](#)]
194. Zeng, Y.; Li, H.; Xia, Y.; Wang, L.; Yin, K.; Wei, Y.; Liu, X.; Luo, S.  $\text{Co}_3\text{O}_4$  nanocrystals with oxygen vacancy-rich and highly reactive (222) facet on carbon nitride scaffolds for efficient photocatalytic oxygen evolution. *ACS Appl. Mater. Interfaces* **2020**, *12*, 44608–44616. [[CrossRef](#)] [[PubMed](#)]
195. Bhattacharyya, K.; Auer, A.A. Oxygen evolution reaction electrocatalysis on cobalt(oxy)hydroxide: Role of Fe impurities. *J. Phys. Chem. C* **2022**, *126*, 18623–18635. [[CrossRef](#)]
196. Li, L.-F.; Li, Y.-F.; Liu, Z.-P. Oxygen evolution activity on  $\text{NiOOH}$  catalysts: Four-coordinated Ni cation as the active site and the hydroperoxide mechanism. *ACS Catal.* **2020**, *10*, 2581–2590. [[CrossRef](#)]
197. Wang, X.; Xi, S.; Huang, P.; Du, Y.; Zhong, H.; Wang, Q.; Borgna, A.; Zhang, Y.-W.; Wang, Z.; Wang, H.; et al. Pivotal role of reversible  $\text{NiO}_6$  geometric conversion in oxygen evolution. *Nature* **2022**, *611*, 702–708. [[CrossRef](#)]
198. Wang, H.; Lu, S. Light inducing the geometric conversion of  $\text{NiO}_6$  to trigger a faster oxygen evolution reaction pathway: The coupled oxygen evolution mechanism. *Energy Environ. Mater.* **2023**, *6*, e12558. [[CrossRef](#)]
199. Jiang, J.; Sun, F.; Zhou, S.; Hu, W.; Zhang, H.; Dong, J.; Jiang, Z.; Zhao, J.; Li, J.; Yan, W.; et al. Atomic-level insight into super-efficient electrocatalytic oxygen evolution on iron and vanadium co-doped nickel (oxy)hydroxide. *Nat. Commun.* **2018**, *9*, 2885. [[CrossRef](#)]
200. Rao, R.R.; Corby, S.; Bucci, A.; García-Tecedor, M.; Mesa, C.A.; Rossmeis, J.; Giménez, S.; Lloret-Fillol, J.; Stephens, I.E.L.; Durrant, J.R. Spectroelectrochemical analysis of the water oxidation mechanism on doped nickel oxides. *J. Am. Chem. Soc.* **2022**, *144*, 7622–7633. [[CrossRef](#)]
201. Li, T.; Zhang, L.; Wang, J.; Zhang, X.; Zhang, L.; Wang, M.; Yan, C.; Tao Qian, T. Facilitating reconstruction of the hetero interface electronic structure by the enriched oxygen vacancy for the oxygen evolution reaction. *Inorg. Chem.* **2023**, *62*, 10504–10512. [[CrossRef](#)]
202. Liu, J.; Xiao, J.; Wang, Z.; Yuan, H.; Lu, Z.; Luo, B.; Tian, E.; Waterhouse, G.I.N. Structural and electronic engineering of Ir-doped Ni-(oxy)hydroxide nanosheets for enhanced oxygen evolution activity. *ACS Catal.* **2021**, *11*, 5386–5395. [[CrossRef](#)]
203. Tian, B.; Shin, H.; Liu, S.; Fei, M.; Mu, Z.; Liu, C.; Pan, Y.; Sun, Y.; Goddard III, W.A.; Ding, M. Double-exchange-induced in situ conductivity in nickel-based oxyhydroxides: An effective descriptor for electrocatalytic oxygen evolution. *Angew. Chem. Int. Ed.* **2021**, *60*, 16448–16456. [[CrossRef](#)]
204. Xiong, Y.; He, P. A review on electrocatalysis for alkaline oxygen evolution reaction (OER) by Fe-based catalysts. *J. Mater. Sci.* **2023**, *58*, 2041–2067. [[CrossRef](#)]
205. Righi, G.; Plescher, J.; Schmidt, F.-P.; Campen, R.K.; Fabris, S.; Knop-Gericke, A.; Schlögl, R.; Jones, T.E.; Teschner, D.; Piccinin, S. On the origin of multihole oxygen evolution in hematite photoanodes. *Nat. Catal.* **2022**, *5*, 888–899. [[CrossRef](#)]
206. Adak, M.K.; Mallick, L.; Samanta, K.; Chakraborty, B. Slow O–H dissociation in the first-order oxygen evolution reaction kinetics on polycrystalline  $\gamma\text{-FeO(OH)}$ . *J. Phys. Chem. C* **2023**, *127*, 154–168. [[CrossRef](#)]
207. Gao, L.; Tang, C.; Liu, J.; He, L.; Wang, H.; Ke, Z.; Li, W.; Jiang, C.; He, D.; Cheng, L.; et al. Oxygen vacancy-induced electron density tuning of  $\text{Fe}_3\text{O}_4$  for enhanced oxygen evolution catalysis. *Energy Environ. Mater.* **2021**, *4*, 392–398. [[CrossRef](#)]
208. Ouyang, Q.; Cheng, S.; Yang, C.; Lei, Z. Ni, Co, and Yb cation Co-doping and defect engineering of  $\text{FeOOH}$  nanorods as an electrocatalyst for the oxygen evolution reaction. *Inorg. Chem.* **2023**, *62*, 1719–1727. [[CrossRef](#)]
209. Li, C.; Chen, M.; Xie, Y.; Wang, H.; Jia, L. Boosting photoelectrochemical water splitting of bismuth vanadate photoanode via novel co-catalysts of amorphous manganese oxide with variable valence states. *J. Colloid. Interf. Sci.* **2023**, *636*, 103–112. [[CrossRef](#)]
210. Mousazade, Y.; Mohammadi, M.R.; Chernev, P.; Bikas, R.; Song, Z.; Lis, T.; Dau, H.; Najafpour, M.M. Water oxidation by a manganese–potassium cluster: Mn oxide as a kinetically dominant “true” catalyst for water oxidation. *Catal. Sci. Technol.* **2018**, *8*, 4390–4398. [[CrossRef](#)]
211. Seo, H.; Park, S.; Cho, K.H.; Choi, S.; Ko, C.; Randriamahazaka, H.; Nam, K.T. Complex impedance analysis on charge accumulation step of  $\text{Mn}_3\text{O}_4$  nanoparticles during water oxidation. *ACS Omega* **2021**, *6*, 18404–18413. [[CrossRef](#)]
212. Yoon, S.; Seo, H.; Jin, K.; Kim, H.G.; Lee, S.-Y.; Jo, J.; Cho, K.H.; Ryu, J.; Yoon, A.; Kim, Y.-W.; et al. Atomic reconstruction and oxygen evolution reaction of  $\text{Mn}_3\text{O}_4$  nanoparticles. *J. Phys. Chem. Lett.* **2022**, *13*, 8336–8343. [[CrossRef](#)]

213. Wang, Y.; Sharma, A.; Duong, T.; Arandiyani, H.; Zhao, T.; Zhang, D.; Su, Z.; Garbrecht, M.; Beck, F.J.; Karuturi, S.; et al. Direct solar hydrogen generation at 20% efficiency using low-cost materials. *Adv. Energy Mat.* **2021**, *11*, 2101053. [[CrossRef](#)]
214. Zhang, J.; Winkler, J.R.; Gray, H.B.; Hunter, B.M. Mechanism of nickel–iron water oxidation electrocatalysts. *Energy Fuels* **2021**, *35*, 19164–19169. [[CrossRef](#)]
215. Yang, Y.; Du, X.; Wang, S.; Zhao, K.; Wang, L.; Qi, Z.; Yang, W.; Hao, J.; Shi, W. Cation transport effect on nickel iron oxyhydroxide electrodes in the oxygen evolution reaction. *Ind. Eng. Chem. Res.* **2022**, *61*, 16702–16710. [[CrossRef](#)]
216. Acharya, P.; Manso, R.H.; Hoffman, A.S.; Bakovic, S.I.P.; Kékedy-Nagy, L.; Bare, S.R.; Chen, J.; Greenlee, L.F. Fe coordination environment, Fe-incorporated Ni(OH) phase, and metallic core are key structural components to active and stable nanoparticle catalysts for the oxygen evolution reaction. *ACS Catal.* **2022**, *12*, 1992–2008. [[CrossRef](#)]
217. Qian, H.; Wei, J.; Yu, C.; Tang, F.; Jiang, W.; Xia, D.; Gan, L. In situ quantification of the active sites, turnover frequency, and stability of Ni–Fe (oxy)hydroxides for the oxygen evolution reaction. *ACS Catal.* **2022**, *12*, 14280–14289. [[CrossRef](#)]
218. Avci, O.N.; Sementa, L.; Fortunelli, A. Mechanisms of the oxygen evolution reaction on NiFe<sub>2</sub>O<sub>4</sub> and CoFe<sub>2</sub>O<sub>4</sub> inverse-spinel oxides. *ACS Catal.* **2022**, *12*, 9058–9073. [[CrossRef](#)]
219. Deng, H.; Jiang, H.; Wang, K.; Wang, Z.; Wang, B.; Zhou, Z.; Li, J. Coupling the vanadium-induced amorphous/crystalline NiFe<sub>2</sub>O<sub>4</sub> with phosphide heterojunction toward active oxygen evolution reaction catalysts. *Nanotechnol. Rev.* **2022**, *11*, 3165–3173. [[CrossRef](#)]
220. Schoen, M.A.W.; Calderon, O.; Randell, N.M.; Jimenez-Villegas, S.; Daly, K.M.; Chernikov, R.; Trudel, S. Local structural changes in polyamorphous (Ni,Fe)O electrocatalysts suggest a dual-site oxygen evolution reaction mechanism. *J. Mater. Chem. A* **2021**, *9*, 13252–13262. [[CrossRef](#)]
221. Sugawara, Y.; Kamata, K.; Ishikawa, A.; Tateyama, Y.; Yamaguchi, T. Efficient oxygen evolution electrocatalysis on CaFe<sub>2</sub>O<sub>4</sub> and its reaction mechanism. *ACS Appl. Energy Mater.* **2021**, *4*, 3057–3066. [[CrossRef](#)]
222. Zheng, J.; Peng, X.; Xu, Z.; Gong, J.; Wang, Z. Cationic defect engineering in spinel NiCo<sub>2</sub>O<sub>4</sub> for enhanced electrocatalytic oxygen evolution. *ACS Catal.* **2022**, *12*, 10245–10254. [[CrossRef](#)]
223. Li, A.; Kong, S.; Guo, C.; Ooka, H.; Adachi, K.; Hashizume, D.; Jiang, Q.; Han, H.; Xiao, J.; Nakamura, R. Enhancing the stability of cobalt spinel oxide towards sustainable oxygen evolution in acid. *Nat. Catal.* **2022**, *5*, 109–118. [[CrossRef](#)]
224. Zhang, B.; Wang, L.; Cao, Z.; Kozlov, S.M.; de Arquer, F.P.G.; Dinh, C.T.; Li, J.; Wang, Z.; Zheng, X.; Zhang, L.; et al. High-valence metals improve oxygen evolution reaction performance by modulating 3d metal oxidation cycle energetics. *Nat. Catal.* **2020**, *3*, 985–992. [[CrossRef](#)]
225. Simondson, D.; Chatti, M.; Bonke, S.A.; Tesch, M.F.; Golnak, R.; Xiao, J.; Hoogeveen, D.A.; Cherepanov, P.V.; Gardiner, J.L.; Tricoli, A.; et al. Stable acidic water oxidation with a cobalt–iron–lead oxide catalyst operating via a cobalt-selective self-healing mechanism. *Angew. Chem. Int. Ed.* **2021**, *60*, 15821–15826. [[CrossRef](#)] [[PubMed](#)]
226. Karim, A.V.; Hassani, A.; Eghbali, P.; Nidheesh, P.V. Nanostructured modified layered double hydroxides (LDHs)-based catalysts: A review on synthesis, characterization, and applications in water remediation by advanced oxidation processes. *Curr. Opinion Solid State and Mater. Sci.* **2022**, *26*, 100965. [[CrossRef](#)]
227. Xu, S.-M.; Pan, T.; Dou, Y.-B.; Yan, H.; Zhang, S.-T.; Ning, F.-Y.; Shi, W.-Y.; Wei, M. Theoretical and experimental study on M<sup>II</sup>M<sup>III</sup>-layered double hydroxides as efficient photocatalysts toward oxygen evolution from water. *J. Phys. Chem. C* **2015**, *119*, 18823–18834. [[CrossRef](#)]
228. Zhang, H.; Wu, L.; Feng, R.; Wang, S.; Hsu, C.-S.; Ashfaq, Y.N.; Zhang, A.C.; Wu, H.; Chen, H.-M.; Zhang, W.; et al. Oxygen vacancies unfold the catalytic potential of NiFe-layered double hydroxides by promoting their electronic transport for oxygen evolution reaction. *ACS Catal.* **2023**, *13*, 6000–6012. [[CrossRef](#)]
229. Kang, J.; Qiu, X.; Hu, Q.; Zhong, J.; Gao, X.; Huang, R.; Wan, C.; Liu, L.-M.; Duan, X.; Guo, L. Valence oscillation and dynamic active sites in monolayer NiCo hydroxides for water oxidation. *Nat. Catal.* **2021**, *4*, 1050–1058. [[CrossRef](#)]
230. Wang, Z.; Goddard III, W.A.; Xiao, H. Potential-dependent transition of reaction mechanisms for oxygen evolution on layered double hydroxides. *Nat. Commun.* **2023**, *14*, 4228. [[CrossRef](#)]
231. Xu, J.; Li, Z.; Chen, D.; Yang, S.; Zheng, K.; Ruan, J.; Wu, Y.; Zhang, H.; Chen, J.; Xie, F.; et al. Active electrocatalyst in the oxygen evolution reaction and flexible zinc–air batteries. *ACS Appl. Mater. Interfaces* **2021**, *13*, 48774–48783. [[CrossRef](#)]
232. Sun, Z.; Lin, L.; He, J.; Ding, D.; Wang, T.; Li, J.; Li, M.; Liu, Y.; Li, Y.; Yuan, M.; et al. Regulating the spin state of Fe<sup>III</sup> enhances the magnetic effect of the molecular catalysis mechanism. *J. Am. Chem. Soc.* **2022**, *144*, 8204–8213. [[CrossRef](#)]
233. Qiao, C.; Usman, Z.; Wei, J.; Gan, L.; Hou, J.; Hao, Y.; Zhu, Y.; Zhang, J.; Cao, C. Efficient O–O coupling at catalytic interface to assist kinetics optimization on concerted and sequential proton–electron transfer for water oxidation. *ACS Nano* **2023**, *17*, 12278–12289. [[CrossRef](#)] [[PubMed](#)]
234. He, X.; Han, X.; Zhou, X.; Chen, J.; Wang, J.; Chen, Y.; Yu, L.; Zhang, N.; Li, J.; Wang, S.; et al. Electronic modulation with Pt-incorporated NiFe layered doublehydroxide for ultrastable overall water splitting at 1000 mA cm<sup>-2</sup>. *App. Catal. B Environ.* **2023**, *331*, 122683. [[CrossRef](#)]
235. Gao, Z.-W.; Liu, J.-Y.; Chen, X.-M.; Zheng, X.-L.; Mao, J.; Liu, H.; Ma, T.; Li, L.; Wang, W.-C.; Du, X.-W. Engineering NiO/NiFe LDH intersection to bypass scaling relationship for oxygen evolution reaction via dynamic tridimensional adsorption of intermediates. *Adv. Mater.* **2019**, *31*, 1804769. [[CrossRef](#)]

236. Luo, Y.; Wu, Y.; Wu, D.; Huang, C.; Xiao, D.; Chen, H.; Zheng, S.; Chu, P.K. NiFe-layered double hydroxide synchronously activated by heterojunctions and vacancies for the oxygen evolution reaction. *ACS Appl. Mater. Interfaces* **2020**, *12*, 42850–42858. [[CrossRef](#)]
237. Zhai, P.; Wang, C.; Zhao, Y.; Zhang, Y.; Gao, J.; Sun, L.; Hou, J. Regulating electronic states of nitride/hydroxide to accelerate kinetics for oxygen evolution at large current density. *Nat. Commun.* **2023**, *14*, 1873. [[CrossRef](#)]
238. Liang, X.; Li, Y.; Fan, H.; Deng, S.; Zhao, X.; Chen, M.; Pan, G.; Xiong, Q.; Xia, X. Bifunctional NiFe layered double hydroxide@Ni<sub>3</sub>S<sub>2</sub> hetero structure as efficient electrocatalyst for overall water splitting. *Nanotechnology* **2019**, *30*, 484001. [[Cross-Ref](#)] [[PubMed](#)]
239. Wu, Z.; Liu, X.; Li, H.; Sun, Z.; Cao, M.; Li, Z.; Fang, C.; Zhou, J.; Cao, C.; Dong, J.; et al. A semiconductor-electrocatalyst nano interface constructed for successive photoelectrochemical water oxidation. *Nat. Commun.* **2023**, *14*, 2574. [[CrossRef](#)] [[PubMed](#)]
240. Guru, S.; Rao, G.R. Review—Strategic design of layered double hydroxides and graphitic carbon nitride heterostructures for photoelectrocatalytic water splitting applications. *J. Electrochem. Soc.* **2022**, *169*, 046515. [[CrossRef](#)]
241. Singh, B.; Singh, A.; Yadav, A.; Indra, A. Modulating electronic structure of metal-organic framework derived catalysts for electrochemical water oxidation. *Coord. Chem. Rev.* **2021**, *447*, 214144. [[CrossRef](#)]
242. Li, C.; Wang, G.; Li, K.; Liu, Y.; Yuan, B.; Lin, Y. FeNi-based coordination crystal directly serving as efficient oxygen evolution reaction catalyst and its density functional theory insight on the active site change mechanism. *ACS Appl. Mater. Interfaces* **2019**, *11*, 20778–20787. [[CrossRef](#)]
243. Gu, M.; Wang, S.-C.; Chen, C.; Xiong, D.; Yi, F.-Y. Iron-based metal-organic framework system as an efficient bifunctional electrocatalyst for oxygen evolution and hydrogen evolution reactions. *Inorg. Chem.* **2020**, *59*, 6078–6086. [[CrossRef](#)]
244. Liu, Y.; Wang, S.; Li, Z.; Chu, H.; Zhou, W. Insight into the surface-reconstruction of metal-organic framework-based nanomaterials for the electrocatalytic oxygen evolution reaction. *Coord. Chem. Rev.* **2023**, *484*, 215117. [[CrossRef](#)]
245. Zhang, W.; Li, F.; Fu, Z.; Dai, S.; Pan, F.; Li, J.; Zhou, L. Co-MOF nanosheets etched by FeCl<sub>2</sub> solution for enhanced electrocatalytic oxygen evolution. *Energy Fuels* **2022**, *36*, 4524–4531. [[CrossRef](#)]
246. Sunil, J.; Narayana, C.; Kumari, G.; Jayaramulu, K. Raman spectroscopy. An ideal tool for studying the physical properties and applications of metal-organic frameworks (MOFs). *Chem. Soc. Rev.* **2023**, *52*, 3397–3437. [[CrossRef](#)]
247. Yu, R.; Wang, C.; Liu, D.; Wang, X.; Yin, J.; Du, Y. Self-reconstruction of Fe-doped Co-metal-organic frameworks boosted electrocatalytic performance for oxygen evolution reaction. *Inorg. Chem.* **2023**, *62*, 609–617. [[CrossRef](#)] [[PubMed](#)]
248. Huang, W.H.; Li, Q.H.; Yu, D.Y.; Tang, Y.H.; Lin, D.Y.; Wang, F.; Zhang, J. Hybrid zeolitic imidazolate frameworks for promoting electrocatalytic oxygen evolution via dual-site relay mechanism. *Inorg. Chem.* **2021**, *60*, 3074–3081. [[CrossRef](#)]
249. Jayaramulu, K.; Masa, J.; Morales, D.M.; Tomanec, O.; Ranc, V.; Petr, M.; Wilde, P.; Chen, Y.-T.; Zboril, R.; Schuhmann, W.; et al. Ultrathin 2D cobalt zeolite-imidazole framework nanosheets for electrocatalytic oxygen evolution. *Adv. Sci.* **2018**, *5*, 1801029. [[CrossRef](#)]
250. Benkó, T.; Lukács, D.; Li, M.; Pap, J.S. Redox-active ligands in artificial photosynthesis: A review. *Environ. Chem. Lett.* **2022**, *20*, 3657–3695. [[CrossRef](#)]
251. Li, M.; Liao, R.-Z. Water oxidation catalyzed by a bioinspired tetranuclear manganese complex: Mechanistic study and prediction. *ChemSusChem* **2022**, *15*, e202200187. [[CrossRef](#)]
252. Chen, Q.-F.; Guo, Y.-H.; Yu, Y.-H.; Zhang, M.-T. Bioinspired molecular clusters for water oxidation. *Coord. Chem. Rev.* **2021**, *448*, 214164. [[CrossRef](#)]
253. Zhang, Q.; Guan, J. Mono-/multinuclear water oxidation catalysts. *ChemSusChem* **2019**, *12*, 3209–3235. [[CrossRef](#)] [[PubMed](#)]
254. Karmakar, P. Transition metal based coordination complexes as catalysts for water oxidation. *Resonance* **2022**, *27*, 1185–1209. [[CrossRef](#)]
255. Masaya, M.; Kondo, M.; Kuga, R.; Kurashige, Y.; Yanai, T.; Hayami, S.; Praneeth, V.K.K.; Yoshida, M.; Yoneda, K.; Kawata, S.; et al. A pentanuclear iron catalyst designed for water oxidation. *Nature* **2016**, *530*, 465–468. [[CrossRef](#)]
256. Chen, G.; Lam, W.W.Y.; Lo, P.K.; Man, W.-L.; Chen, L.; Lau, K.-C.; Lau, T.-C. Mechanism of water oxidation by ferrate(VI) at pH 7–9. *Chem. Eur. J.* **2018**, *24*, 18735–18742. [[CrossRef](#)]
257. den Boer, D.; Konovalov, A.I.; Siegler, M.A.; Hettterscheid, D.G.H. Unusual water oxidation mechanism via a redox-active copper polypyridyl complex. *Inorg. Chem.* **2023**, *62*, 5303–5314. [[CrossRef](#)]
258. Li, Y.-Y.; Wang, X.-Y.; Li, H.-J.; Chen, J.-Y.; Kou, Y.-H.; Li, X.; Wang, Y. Theoretical study on the mechanism of water oxidation catalyzed by a mononuclear copper complex: Important roles of a redox non-innocent ligand and HPO<sub>4</sub><sup>2-</sup> anion. *RSC Adv.* **2023**, *13*, 8352–8359. [[CrossRef](#)]
259. Iqbal, S.; Safdar, B.; Hussain, I.; Zhang, K.; Chatzichristodoulou, C. Trends and prospects of bulk and single-atom catalysts for the oxygen evolution reaction. *Adv. Energy Mater.* **2023**, *13*, 2203913. [[CrossRef](#)]
260. Kumar, P.; Kannimuthu, K.; Zeraati, A.S.; Roy, S.; Wang, X.; Wang, X.; Samanta, S.; Miller, K.A.; Molina, M.; Trivedi, D.; et al. High-density cobalt single-atom catalysts for enhanced oxygen evolution reaction. *J. Am. Chem. Soc.* **2023**, *145*, 8052–8063. [[CrossRef](#)]
261. Cipriano, L.A.; Liberto, G.D.; Pacchioni, G. Superoxo and peroxo complexes on single-atom catalysts: Impact on the oxygen evolution reaction. *ACS Catal.* **2022**, *12*, 11682–11691. [[CrossRef](#)]
262. Barlocco, I.; Cipriano, L.A.; Liberto, G.D.; Pacchioni, G. Does the oxygen evolution reaction follow the classical OH\*, O\*, OOH\* path on single atom catalysts? *J. Catal.* **2023**, *417*, 351–359. [[CrossRef](#)]

263. He, Y.; Zhou, X.; Jia, Y.; Li, H.; Wang, Y.; Liu, Y.; Tan, Q. Advances in transition-metal-based dual-atom oxygen electrocatalysts. *Small* **2023**, *19*, 2206477. [[CrossRef](#)]
264. Fang, C.; Zhou, J.; Zhang, L.; Wan, W.; Ding, Y.; Sun, X. Synergy of dual-atom catalysts deviated from the scaling relationship for oxygen evolution reaction. *Nat. Commun.* **2023**, *14*, 4449. [[CrossRef](#)]
265. Sayama, K.; Arakawa, H. Effect of carbonate salt addition on the photocatalytic decomposition of liquid water over Pt–TiO<sub>2</sub> catalyst. *J. Chem. Soc. Faraday Trans.* **1997**, *93*, 1647–1654. [[CrossRef](#)]
266. Kusama, H.; Kodera, M.; Yamashita, K.; Sayama, K. Insights into the carbonate effect on water oxidation over metal oxide photocatalysts/photoanodes. *Phys. Chem. Chem. Phys.* **2022**, *24*, 5894–5902. [[CrossRef](#)] [[PubMed](#)]
267. Yang, C.; Laberty-Robert, C.; Batuk, D.; Cibir, G.; Chadwick, A.V.; Pimenta, V.; Yin, W.; Zhang, L.; Tarascon, J.-M.; Grimaud, A. Phosphate ion functionalization of perovskite surfaces for enhanced oxygen evolution reaction. *J. Phys. Chem. Lett.* **2017**, *8*, 3466–3472. [[CrossRef](#)] [[PubMed](#)]
268. Tsuneda, T.; Ten-no, S. Water-oxidation mechanism of cobalt phosphate co-catalyst in artificial photosynthesis: A theoretical study. *Phys. Chem. Chem. Phys.* **2022**, *24*, 4674–4682. [[CrossRef](#)]
269. Liu, M.; Li, N.; Wang, X.; Zhao, J.; Zhong, D.-C.; Li, W.; Bu, X.-H. Photosystem II inspired NiFe-based electrocatalysts for efficient water oxidation via second coordination sphere effect. *Angew. Chem. Int. Ed.* **2023**, *62*, e202300507. [[CrossRef](#)] [[PubMed](#)]
270. Gao, Y.; Wu, C.; Sen, S.; Tan, Y. Hexadecyltrimethylammonium hydroxide promotes electrocatalytic activity for the oxygen evolution reaction. *Commun. Chem.* **2020**, *3*, 154. [[CrossRef](#)]

**Disclaimer/Publisher’s Note:** The statements, opinions and data contained in all publications are solely those of the individual author(s) and contributor(s) and not of MDPI and/or the editor(s). MDPI and/or the editor(s) disclaim responsibility for any injury to people or property resulting from any ideas, methods, instructions or products referred to in the content.